Engineering and Evaluating Chimeric Antigen Receptor T Cell Potency Ex Vivo and In Vitro

By

Nicole Jenine Piscopo

A dissertation submitted in partial fulfillment of

the requirements for the degree of

Doctor of Philosophy

(Biomedical Engineering)

at the

UNIVERSITY OF WISCONSIN-MADISON

2020

Date of final oral examination: 08/04/2020

The dissertation is approved by the following members of the Final Oral Committee:

Krishanu Saha, Associate Professor, Biomedical Engineering

David Beebe, Professor, Biomedical Engineering

Christian Capitini, Associate Professor, Pediatrics

Anna Huttenlocher, Professor, Medical Microbiology and Immunology

Megan McClean, Assistant Professor, Biomedical Engineering

TABLE OF CONTENTS

ABSTRACT

Engineering and Evaluating Chimeric Antigen Receptor T Cell Potency

Ex Vivo and In Vitro

Nicole Jenine Piscopo

Under the supervision of Professor Krishanu Saha

at the University of Wisconsin-Madison

Chimeric antigen receptor (CAR) T cells are genetically engineered T cells that have been used to target cancer-associated antigens [1]. The profound success of CAR T cells in treating hematological malignancies (e.g. leukemia by targeting CD19) has led to the FDA approval of three CAR T cell products [2]. CAR T cells are primarily engineered via viral methods which insert the CAR transgene into random locations in the genome resulting in varied expression and signal activation of the CAR [3]. As a result, CAR T cell performance can vary greatly from cell to cell even within the same batch, due in part to the heterogeneity of CAR activity within the gene-modified T cell population [4]. Therefore, to better ensure that manufactured CAR T cells will result in cancer remission, improvements to the manufacturing process must be made to certify that the live cellular products will act accordingly once they are delivered to the patient [5].

This thesis aims to engineer precise control over the location of integration and copy number afforded by CRISPR-Cas9 gene editing tools to create more homogenous expression of the CAR in the manufactured CAR T cell population, resulting in less variance in potency of individual CAR T cells. First, I describe the manufacture and measurement of expression and function within virally generated and CRISPR-Cas9 generated CAR T cell products. Next, I detail the *in vitro* functional analysis of CAR T cells within microwell co-cultures with target cancer cells to allow for measure of *in vitro* activity of the CAR+ cells and acquire relevant parameters

for mathematical models. Finally, I share the results of *in vivo* testing and computational modeling of CAR T cell therapies within murine xenograft models. This work demonstrates the value of precise gene editing in CAR T cell manufacture, and its influence on quality assurance and quality control (QA/QC) methods of CAR T cell products.

ACKNOWLEDGEMENTS

I am very lucky to have the community that I have around me, and the following are simply some of the people I am grateful to have had in my corner:

Jen, Elissa, Mike, Ginny, Rachel, Ray, and Mrs. Tummey, many people tell me that they don't talk to anybody from high school anymore, and then I realize how grateful I am to still be so close with you all. Thank you for always talking me up and encouraging me to continue in my pursuit of elite nerdiness.

Kevin McLaughlin, thank you for creating the BRIDGE program and inviting me and providing me with the great community that I was able to have all throughout my time at UConn. You truly helped to set me up for success.

Dr. Stephany Santos, going into college, I knew I wanted to get involved in research, even though I didn't really know what that meant. I looked up to you from day 1 and you told me how to reach out to get my first position in a lab and I was so fortunate to have you to guide me through that, and beyond.

Dr. Caroline Jakuba, I am so lucky to have been your undergrad. I know that so much of what I have achieved I did so because of the skills you instilled in me in my first months as a researcher. Thank you for continuing to help me long after we both left UConn.

Rita, (and Rita's mom), thank you for adopting me while I lived in Connecticut and for always encouraging me in my scientific endeavors. I can't wait to see you soon!

Dr. Yusuf Khan, I can still remember sitting in your office in September of my senior year when you told me I was capable of doing a PhD. The thought had never crossed my mind until you said that. So I guess this is all your fault! Just kidding. But I am so grateful for this experience that I know I would not have had without your encouragement.

Ana, Jared, and Ben, thank you for all being such wonderful examples of graduate students to look up to. And thank you for always answering my texts long after you have left UW.

Dr. Peter Zandstra and Dr. Daniel Aguilar-Hidalgo, thank you for welcoming me into your lab and helping me to develop my project further. Thank you Daniel, for being such a great mentor during my time at UBC!

Jess, Jake, Ellen, Adam, Taylor, Emily, thank you all for making Wisconsin feel like home, and inviting me into your homes and taking me all across this beautiful state. And thank you for tolerating every time I mentioned that the best Badger running backs are from New Jersey.

Nisha, thank you for being from New Jersey and for always being willing to discuss all things New Jersey while we both reside in the Midwest. And also thank you for always being willing to substitute wine and cheese for any meal of the day, and also for always giving me advice.

November Project, thank you for always giving me something to look forward to when the science got tough. You always helped me to start my day off on the right foot.

Lab mates, especially Katie and Kaivalya, working from home has made me realize how much you all brighten my day. Thank you for helping to make my time in graduate school a more positive experience.

Brittany, out of the 30,000 undergrads at this school, I truly lucked out by getting to work with you, and for 3 years! Thank you for being such a joy to mentor.

Kris, thank you for (and how dare you) giving me the freedom to choose my own project and path during graduate school. It hasn't made for the easiest ride, but then again, a smooth sea never made for a skilled sailor. Thank you for the endless opportunities you presented me with.

Mom and Don, thank you for teaching me to be independent and to work for the things I want in life. Don, you were the first person to start looking at colleges for me and you always taught me to go through life doing things for the right reason. Mom, I could not have had a stronger woman to look up to all of my life. I think knowing that you worked in a garage full of men and never let that stop you from providing for our family lead me to never question my place in a male dominated field, and I know I would not be here without you and your support.

LIST OF ABBREVIATIONS

aAPC	artificial antigen presenting cells
AAV	adeno-associated virus
alloHSCT	allogenic hematopoietic stem cell transplant
BMT	bone marrow transplant
bp	base pair
CAR	chimeric antigen receptor
CRISPR	clustered regularly interspaced short palindromic repeats
Cas9	CRISPR-associated protein 9
CQA	critical quality attributes
DNA	deoxyribonucleic acid
DSB	double strand break
dsDNA	double stranded DNA
FACS	fluorescence-activated cell sorting
FRET	fluorescence resonance energy transfer
GFP	green fluorescent protein
GMP	good manufacturing practice
GVHD	graft versus host disease
HCA	high-content analysis
HDR	homology directed repair
HSCT	hematopoietic stem cell transplant
ICANS	immune effector cell associated neurotoxicity syndrome
IL	interleukin
indel	insertion/deletion mutation
iPSC	induced pluripotent stem cell
IVT	*in vitro* transcription
NHEJ	non-homologous end joining
NGS	next-generation sequencing
NK	natural killer

NLS	nuclear localization signal
nt	nucleotide
NV	non-viral
ODE	ordinary differential equations
PAM	protospacer adjacent motif
PAT	process analytical techniques
PBMC	peripheral blood mononuclear cells
PCR	polymerase chain reaction
PDMS	polydimethylsiloxane
PLSR	partial least square regression
QA	quality assurance
QC	quality control
qPCR	quantitative PCR
REMS	risk evaluation and mitigation strategy
RNA	ribonucleic acid
RNP	ribonucleoprotein
RT-PCR	reverse transcription PCR
RV	retroviral
scFv	single chain variable fragment
sgRNA	short guide ribonucleic acid
TALEN	tale-like effector nuclease
TCR	T cell receptor
ZFN	zinc-finger nuclease

CHAPTER 1: Introduction

Portions of the work in this chapter were adapted from:

Bioengineering Solutions for Manufacturing Challenges in CAR T Cells

N.J. Piscopo*, K.P. Mueller*, A. Das*, P. Hematti, W.L. Murphy, S.P. Palecek, C.M. Capitini, K. Saha

Biotechnol J. 2018 February; 13 (2).

* *these authors contributed equally*

CAR Immune Cell Therapy

The four main pillars of cancer treatment are surgery, radiation, chemotherapy, and hematopoietic stem cell transplantation (HSCT). In the last two decades, immunotherapy has rapidly developed into a promising 5th pillar, initially consisting mainly of monoclonal antibody and cytokine therapies [6], [7]. In the last five years, chimeric antigen receptor (CAR) T cell therapy has emerged at the forefront of the cancer immunotherapy field [8], [9]. In the CAR T approach, genetically modified lymphocytes are engineered to express a synthetic receptor comprised of an extracellularly expressed single chain variable fragment (scFv) of a monoclonal antibody, which is connected via a transmembrane linker to the intracellular signaling domains of common T cell co-receptors such as CD3 and CD28 [10]–[12] (**Figure 1.1A**). The scFv portion of the CAR is used to target specific surface antigens (e.g., CD19, a B cell lineage surface marker used to target acute lymphoblastic and chronic lymphocytic leukemias) [13]–[16]. This allows the CAR to bypass conventional interactions between the T cell receptor (TCR) and major histocompatibility complex (MHC), thus activating the cell upon recognition of the target antigen [17].

The typical CAR T cell manufacturing process (**Figure 1.1B**) begins with harvesting the patient's peripheral blood mononuclear cells (PBMCs) through leukapheresis. These apheresed cells are virally transduced with the CAR transgene [18], activated, and expanded outside of the body (*ex vivo*), undergoing quality control (QC) testing before administration [19]. The entire manufacturing process can last between 10 to 22 days, beginning with T cell harvest and ending with intravenous delivery of the engineered CAR T cells back to the patient [20],[21].

Amongst published trials targeting hematological malignancies, the therapy has resulted in complete or partial remissions across CAR designs and targets in approximately 70~94% of patients [22], [23]. The adoption of CAR T cell therapy into clinical practice shows similarities to

the early stages of adoption of bone marrow transplantation (BMT). BMT was initially viewed with skepticism and offered at few academic centers [24]. The therapy gained traction as its efficacy became apparent, and it is now available at a much larger number of centers across the globe, having been performed over one million times worldwide [25], [26]. Similarly, the full CAR T cell manufacture and therapy workflow including gene delivery, culture, and clinical care is limited to a handful of academic centers often in partnerships with industry (University of Pennsylvania with Novartis, Seattle Children's Hospital and Memorial Sloan Kettering Cancer Center with Juno Therapeutics a Bristol-Myers Squibb company, Baylor College of Medicine with Cell Medica, MD Anderson Cancer Center with Ziopharm Oncology and Precigen Inc., and the National Cancer Institute with Kite Pharma of Gilead Sciences) with advanced manufacturing and clinical capabilities [19]. However, the geographical reach of CAR T cell therapy has increased with the advent of multicenter clinical trials supported by several pharmaceutical companies (e.g. fully recruited clinical trial NCT02435849 with 26 study locations).

A variety of biological challenges have limited the broad clinical applicability of CAR T cell therapy. First, CAR T cell therapy to date has only shown efficacy for certain hematological malignancies, and there are still problems present despite the successes. The therapeutic process could be complicated by severe adverse events including cytokine release syndrome (CRS), immune effector cell (IEC)-associated neurotoxicity syndrome (ICANS), and in the case of targeting CD19, B-cell aplasia [16]. These pose significant concerns, although standard treatment options such as chemotherapy and stem cell transplantation have equally severe side effects, including acute toxicity and the risk of graft-versus-host disease (GVHD), respectively [27], [28]. Additionally, recent attempts to treat solid tumors with CAR T cells have yielded lackluster results, due in part to heterogeneous CAR T cell populations that have performed inconsistently and in

some cases failed to persist within the body [29], [30]. It has proved challenging to find proper target antigens for solid tumors, and strategies to improve T cell penetration into the tumor microenvironment are needed [29]. Furthermore, T cell exhaustion and differentiation are concerns for the lack of persistence *in vivo* [29]. While problems arising primarily from T cell biology are currently being addressed [10], there is still a need to address manufacturing paradigms and processes to ensure that CAR T cell therapy can be translated widely.

Cell Harvesting and Transportation

CAR T cell therapies can use either autologous or allogeneic T cells, although allogeneic therapies may run a greater risk of immunogenic reactions due to graft-versus-host disease (GVHD) [31]. Most current CAR T cell clinical trials use T cells collected from patients. CAR T cell therapy begins with the leukapheresis procedure to isolate PBMCs [18]. Leukapheresis typically occurs over several hours, during which the patient's blood is treated with anticoagulants and centrifuged to remove excess red blood cells and platelets. The patient's PBMCs are then either shipped to a manufacturing facility as a fresh product or cryopreserved for shipment in the future. Leukapheresis may be complicated for patients that have already been treated for their malignancies, as the resulting lymphopenia from chemotherapy can make it difficult to collect a sufficient number of T cells [32]. Leukapheresis is also more challenging for infants and small children due to their lower total blood volume [33]. Additionally, prolonged treatment with anticoagulants during leukapheresis can pose problems due to the length of time that patients are connected to an external device [34].

Once PBMCs have been isolated, some centers cryopreserve the cells and ship them to centralized manufacturing facilities for activation, viral transduction, and expansion [18]. The cells

are cryopreserved in blood bags and shipped frozen, then thawed and activated after arrival at the manufacturing facility. Transport of the T cells is an important consideration, as it is critical to ensure that desired cytotoxic populations are well preserved. Previous studies have indicated broad changes in PBMC transcriptomes after freezing and thawing [35], while others have shown that re-stimulation can rescue freeze/thaw-induced changes observed in regulatory T cells [36]. Aberrations in cell functionality due to cryopreservation proved prohibitive for Provenge®, the first FDA-approved autologous cell therapy product [37]. Provenge® was only viable for four hours post-thaw and could not be used after being frozen for 18+ hours [38]. As a result of strict delivery conditions and timelines, Provenge® was deemed financially unviable [39], although it remains an instructive case study for CAR T cell therapy. Thus, although some current clinical trials have successfully used freezing and thawing to transport T cells, there may be room for improvement.

To start, better quality control (QC) mechanisms will be required to confirm cell viability and immune profile changes [40] in the form of *in vitro* tumor cell killing assays and cell profiling techniques. Additionally, progress has been made to minimize the impact of cryopreservation reagents such as dimethyl sulfoxide (DMSO) to generate clinically safe products. Microfluidic devices to remove DMSO by diffusion have been described which allow over 95% of cells to be retained post-wash, thus improving yields by ~25% [41]. Furthermore, cell recovery outcomes may be improved through the use of hypothermic preservation solutions (e.g. HypoThermosol®), which allow cells to be transported without the need for freezing [42]. Such approaches have not yet been implemented in CAR T cell manufacturing but may one day improve production efficiency and safety.

Activation and Expansion of T cells

In order to trigger T cell killing mechanisms, CAR T cells must be stimulated via antigen recognition [43]. The most commonly used activation process is independent of antigen presentation and involves culturing T cells with beads coated with CD3/CD28 antibody fragments, along with IL-2 supplementation [19]. While T cells are naturally activated in response to short-term antigen presentation, sustained signaling can cause exhaustion, leading to a loss of proliferative capacity and cytotoxicity [44]. Therefore, it would be beneficial to ensure activation but limit exhaustion through custom biomaterials. This has been achieved through artificial antigen presenting cell (aAPC) technology [45], which can include beads coated with a CD28-specific antibody, a specific antigen epitope, and soluble human leukocyte antigen immunoglobulin (HLA-Ig) [46]. More recently, cells expressing HLA-Ig that are engineered with an antigen epitope have been used as aAPCs [47].

As current methods for activation are time consuming [19] and can lead to exhaustion, there is significant room for improvement in this stage of CAR T cell manufacturing. Tissue engineering approaches may improve the activation process via customizable ligand-presenting scaffolds in the place of aAPCs. These could potentially feature controlled spatial or temporal patterns of ligand presentation. For example, spatially patterned ligands have been used to study and control cell adhesion [48], and degradable materials may be useful to slowly release ligands, thus modulating the activation response [49]. It has also been shown that micropatterned T cell costimulatory ligands can enhance secretion of IL-2 by CD4+ T cells via a CD3/CD28 co-stimulation array. These same technologies could be utilized to potentially ameliorate activation-associated problems such as exhaustion [50]–[52].

Another vital process in the CAR T cell manufacturing pipeline is expansion. Expansion is required to increase the population of T cells available for transduction or infusion to the patient and can occur either before or after gene transduction, depending on the manufacturer [53], [54]. Currently, this process can be accomplished via several platforms. Wave-mixed bioreactors (e.g., GE, Sartorius bioreactors) feature a bioprocessing bag (e.g., Cellbag®, Flexsafe®) on a rocking base for efficient gas exchange and media perfusion, and are widely used across academic and industrial labs to support clinical trials [55]. Fully automated closed systems such as CliniMACS® are also being developed to allow for good manufacturing practice (GMP)-compliant production without the need for clean room facilities [56]. The cell expansion process takes approximately ten days, upon which cells are harvested and cryopreserved for distribution [19].

Current expansion platforms use CD3 and CD28 antibody-functionalized beads to expand general T cell populations (e.g., Dynabeads™ [57]). These beads are prone to aggregation, particularly when used in agitated systems such as GE WAVE [58], [59]. Additionally, ligand presentation needs to be optimized, to ensure that sufficient quantities of cells are activated. Beads have the advantage of a high surface area to volume ratio, which allows for a greater density of ligand presentation. However, the process of removing the beads can cause a loss of product if T cells fail to dissociate or are damaged by shear forces due to binding [60], [61]. To address this issue, bead-free T cell expansion systems utilizing tetrameric CD3/CD28 antibody complexes have been developed by Juno Therapeutics and others, including Expamer™ technology [19]. Ligand-functionalized surfaces could potentially be utilized to circumvent some of these difficulties, enabling the use of other bioreactor architectures. These surfaces could be within hollow fiber membrane bioreactors [62], packed bed bioreactors [63], and potentially, stainless steel stirred tank bioreactors, as antibody functionalization of stainless steel surfaces has been demonstrated [64].

Once expanded, T cells could then be detached using controlled chemistries that release the bound cell from the surface [65], [66]. Such an approach could reduce aggregation and shear stress on the cells.

Cellular metabolic profiles provide an additional phenotypic measurement that can be used to affect cell fate decisions to preferentially expand cells in a mixed culture [67], [68]. In cardiac differentiation of induced pluripotent stem cells (iPSCs), cardiomyocytes metabolize lactate better than non-cardiomyocyte populations generated during differentiation: bioengineers dosed mixed cultures with lactate to increase cardiomyocyte purity in culture [69]. Similar metabolic engineering approaches may prove advantageous for preferentially expanding T cell subsets. Activation of mammalian Target of Rapamycin (mTOR), a regulator of cellular metabolism [70], can influence T cell differentiation fates by altering responses to metabolite changes [71]. Positive and negative mTOR signaling modulators could be used to control *ex vivo* expansion. Levels of amino acids, including tryptophan, arginine, and glutamine, have been indicated in T cell proliferation; hence, amino acid titration is another tool that could be utilized to improve T cell proliferation [72]–[75]. Fatty acid titration could also be employed, as fatty acids have been implicated in CD8+ T cell proliferation, survival and activation [76]. Metabolites can be assayed using many techniques, including fluorescence-based methods to monitor intracellular metabolism in real time [77], and microfluidics [78].

CAR Gene Transfer and Editing

CAR T cell manufacturing for clinical trials currently uses viral vectors (mostly lentiviruses and retroviruses) to transfer the CAR transgene [19], [23], all of which have high transduction efficiencies (approximately 68% for retroviruses, depending on the multiplicity of

infection) [79]. Despite the success of viruses in transfecting T cells, which are notoriously hard to transfect, viral approaches have several major drawbacks, both in terms of patient safety and manufacturing practicality (**Table 1**). Since viral vectors insert transgenes randomly into the genome, there is a risk of gene silencing or insertional oncogenesis [80]. Additionally, the lack of control over the copy number of transgenes inserted into the genome, and the endogenous regulatory elements that will act on this transgene, leads to heterogeneity that can also influence the expression levels of the CAR protein on the cell surface, as can be seen in **Figure 1.2**, further complicating QA/QC efforts [81], [82]. Integration-site analysis shows that when lentiviral transduction is used to manufacture CAR T cells, across 184 pre-infusion and post-infusion samples from 40 patients, over 145,600 unique integration sites were found [83]. Location of integration also influenced Novartis' CART19 proliferation post infusion which could influence patient outcomes. There are additional manufacturing issues associated with viral vectors, which are expensive to produce and require costly QC [84]. Furthermore, the demand for viruses is increasing, making it more difficult to supply the ever growing demand as engineered cellular therapies become more widespread [85]. While the scale of viral manufacturing has been adequate for phase I/II clinical trials, this will be a significant barrier to entry for centers that wish to implement CAR T cell therapy for larger patient populations [85].

Recent advances in non-viral transfection techniques have shown promise in ameliorating some of the issues associated with viral vectors. One approach utilizes transposons, including the Sleeping Beauty [86] and Piggybac transposon systems [87]. Both transposons have been used to successfully generate CAR T cells [45], [88]–[90]. However, they utilize random transgene insertion, which carries risks for clinical safety and efficacy. Additionally, transposons by nature allow the transferred gene to repeatedly change genomic location [91], which further complicates

QC efforts. To address these concerns, many researchers are turning to genome editing methods that allow for site-directed mutagenesis to improve CAR T cell manufacture.

Site-specific editing tools appeared in the early 2000s with the development of zinc finger nucleases (ZFNs) [92] and transcription activator-like effector nucleases (TALENs) [93]. ZFNs and TALENs are chimeric, customizable restriction enzymes that are engineered to target specific loci in the genome, including validated safe-harbor loci [94]. The cost to manufacture ZFNs and TALENs is significant, as individual proteins must be designed for each editing locus [95], [96]. ZFN technology has yet to advance to clinical trials for CAR T cell therapy, although it has been used for other clinical targets, including Hemophilia B and HIV [97], [98]. TALENs have been used preclinically to successfully treat two infant patients ahead of planned phase I clinical trials [99]. In these cases, TALENs were used to knock out the endogenous TCR in allogeneic T cells, although the CAR itself was delivered virally. This technology is actively being developed by Cellectis for their UCART19 product, is now in Phase I clinical trials [99].

In recent years, the development of clustered regularly interspaced short palindromic repeats (CRISPR) Cas9 gene editing, has revolutionized genome editing in laboratory settings [100] and allowed for precise cuts to be made in the genome that can facilitate the incorporation of foreign genomic materials while keeping costs down [101]. CRISPR/Cas9 technology involves the use of a Cas9 nuclease coupled to a short guide RNA (sgRNA), which can be designed to target nearly any locus in the genome and lead to the creation of a double stranded break [102], [103]. The nuclease can be delivered in the form of a ribonucleoprotein (RNP), or as a plasmid that is then expressed by the target T cell [100]. When Cas9 is instructed to make cuts in the genome and no repair template is provided, cells preferentially undergo error prone repair through non-homologous end joining (NHEJ) leading to high rates of mutations, depending on the loci and

gRNA used [100]. This imprecise repair pathway can be circumvented by introducing a repair template, through co-opting the cell's intrinsic homology directed repair (HDR) pathway [102].

CRISPR is an efficient and flexible genome-editing technology, and CRISPR-Cas9 HDR has been used to create CAR T cells in few instances, with great success. First, Cas9 mRNA has been delivered via electroporation to T cells, followed by delivering the CAR via a non-integrating AAV6 vector with homology arms to the highly conserved T cell Receptor Alpha Chain (*TRAC)* locus. In a preclinical study, these CRISPR produced CAR T cells exhibited a high degree of homogeneity, resulted in increased CAR T cell efficiency through decreased rates of exhaustion, and lead to superior survival outcomes in a hematological murine model [82]. Additionally, Cas9 and sgRNA have also been delivered in a fully non-viral manner as a RNP through nucleofection with the affinity-enhanced T cell receptor gene delivered as a double-stranded HDR template [104],[105]. These findings suggest that strategic and precise CAR integration may be important for developing reliable and effective therapies. While CRISPR generated CAR T cells have yet to make it to the clinic, CRISPR has been used to enhance viral generated CAR T cells through the knockout of *TRAC, TRBC,* and *PDCD1* in phase I clinical trials which have proven that the edits were well tolerated and durable [106]. The success in this early work with CRISPR CAR T cells points towards the potential for a new paradigm of more effective and precise CAR T cell manufacture.

Quality Control and Assurance

The complete CAR T cell therapeutic process requires extensive equipment and technical expertise to manufacture cellular products of high quality in a relatively short period of time [19]. Facilities must be capable of handling clinical-grade vectors, conducting gene transfection, and

performing their own QC before reinfusing cells to the patient. Additionally, facilities require the infrastructure to care for CAR T cell recipients both prior to infusion, while these patients still have active disease, and post-infusion, upon which they may experience severe side effects. Hospitals that wish to offer CAR T therapy must acquire Risk Evaluation and Mitigation Strategy (REMS) certification. Few places can currently offer all of these components; as such, the current CAR T cell manufacturing approach is moving towards a centralized format, in which academic clinical centers ship patient's cells to a facility for genome editing and expansion under ISO5 GMP conditions [54]. This centralized model has led to the development of rapidly expanding CAR T cell companies including Juno Therapeutics, Kite Pharma, Novartis, Cellectis, Bluebird Bio, Bellicum, Century Therapeutics, AstraZeneca, CRISPR Therapeutics, and others [107].

Quality control and assurance for CAR T cell products can be assisted through the use of process analytical techniques (PAT) and model predictive control (MPC). MPC is a tool in which workflows are managed through mathematical predictions of outcomes based on the current measured state of the process, enabling significant gains in efficiency and automation [108] (**Figure 1.3**). However, these techniques are rarely used for mammalian cell culture-based processes [109], primarily due to a lack of monitoring tools [110]. Studies on the metabolic requirements of T cell subsets could yield useful monitoring targets as advanced process control techniques for mammalian cell culture rely on metabolic flux analysis [111], [112],[113]. PAT for T cell culture could include immune biosensors [114] and spectroscopic techniques [115]. Soft sensors could be used to integrate measurements of secreted cytokines and metabolite concentrations with software modeling to estimate other components [116]. In CAR T cell expansion, multiphoton redox-based imaging could be used to measure intracellular respiration [77] in combination with biosensors to detect secreted cytokines [117], potentially identifying T

cell phenotype distributions in situ. As with biopharmaceuticals [118], it is expected that regulatory agencies will request quality-by-design-based improvements in cell manufacturing, PAT, and automation to be integrated into current CAR T cell production paradigms.

In Vitro Cytotoxicity Assays to Assist in Prediction of Cell Therapy Potency

A commonly used bioassay for quality control and assurance to measure cell induced cytotoxicity are *in vitro* cytotoxicity assays. The current gold standard for *in vitro* cytotoxicity assays is the Chromium Release Assay, a technique that was developed in 1968 [119]. During a chromium release assay, the target cells are incubated with radioactive Chromium^{51}, transferred to a new plate, and co-cultured with cytotoxic cells. The primary readout of this assay is the amount of released Chromium, which serves as a proxy for the amount of target cell death [120]. Yet, there is no information recorded about any change in the cytotoxic cells, and no data other than relative amounts of death between different conditions is recorded about the target cells. Furthermore, the assay can only provide information at a single timepoint as the sample cannot be measured multiple times. From a manufacturing perspective, radioactive Chromium is not a preferred material to have in most lab settings due to health and safety issues, as well as the high cost associated with radioactive disposal [119], [121].

As a result of the limitations associated with Chromium release assay, other methods have been employed to serve as cytotoxicity assays. Bioluminescence assays involve the use of luciferase cell lines that stop illuminating in the absence of ATP [122]. While these assays remove the issue of radioactivity and allow for measurements at multiple timepoints, they still only provide information on the state of the target cell. The same could be said for calcien or fluorescence resonance energy transfer (FRET) assays, as well as impedance-based methods that measure cell

adherence [123]–[125]. Flow cytometry-based cytotoxicity assays, another common approach (especially for use with immune cells) have an advantage over the assays mentioned above. With flow cytometry, multiple dyes can be used to provide information on the presence of not only live versus dead cells, but also different cell populations at the time of analysis, such as effector T cells, or helper T cells [126], [127]. Like many of the other approaches, flow cytometry is a destructive process and cannot be used to track the progression of cell death over time.

More recently, cytotoxicity assays that allow for longitudinal tracking through non-impedance, image-based analysis assays have gained in popularity. The IncuCyte® is one such assay which has recently been used in numerous papers to measure cytotoxicity [128], [129]. The attraction with the IncuCyte is that it can be placed directly into an incubator and applied to common culture vessels [130]. There is still value to be gained from cocultures that are smaller than a 96-well plate, but larger than a single cell per well platform. An image based assay that does not require constant image acquisition and can still allow for the measurement of functional capabilities of immune cells has the potential to provide another piece of information about how these cells might behave after infusion into patients.

Population Dynamics of Cancer and Immune Cells

Mathematical modeling allows scientists to simulate investigational scenarios and gain input about how altering various experimental conditions may influence the expected outcome. Mathematical modeling surrounding the biology of T cells in the context of chronic infections has been explored for decades, and in recent years has begun to move into the realm of how T cells interact with tumors [131]. Tumors themselves have been modeled using multiple methods, both spatial and nonspatial [132]–[134]. Many of the early models of T cell and tumor interactions represented the

immune cells and cancer cells in a series of ordinary differential equations (ODEs) that followed a predator and prey basis, respectively [135]. Since then, models have begun to include other features of the natural immune system, such as cytokines [136]. The Pennisi model of T cells and monoclonal antibody delivery takes into account that the injection compartment is different from the site of the tumor and accounts for trafficking of the T cells to the site of the melanoma [137]. Another model has taken into account how tumor cells can evolve and gain resistance to immune cells [138]. Furthermore, these models that simulate immune cell mediated cytotoxicity towards cancer have been adapted to both human and mouse estimated parameters, allowing for the ability to apply similar ODEs to both systems [139].

Despite the progress in modeling of the immune systems interactions with cancer, there are limited studies regarding the interactions between CAR T cells and cancer. CAR T cells can be expected to follow the same proliferation as antigen driven T cell proliferation, but the level of response is dependent on the expression level of the CAR, the affinity of the specific scFv clone and the co-stimulatory domains present [140]. Furthermore, the total peak in proliferation is dependent on disease burden [140]. Even then, most of those papers are modeled in the context of anti-CD19 CAR T cells against hematological malignancies, which does not account for the tumor microenvironment. There is ample room for improvement to model issues plaguing the CAR T fight in solid tumors.

Evaluating CRISPR Cas9 Engineered CAR T Cell Potency with *in vitro* Co-culture Assays

As cellular therapies move to the market, it will be necessary to identify a specific set of critical quality attributes (CQAs) that will define the cellular product to improve the success of these therapies in trials. Understanding the sources of heterogeneity and their effect on cell functionality

will be vital for ensuring the best possible patient outcomes by reducing the amount of variation in the therapeutic product. The overall, long-term goal of this research is to shift patient outcomes from the current mix of non-responders, partial responders, and complete responders, to a higher proportion of complete responders.

While the current clinical workflow uses viruses, an efficient method for CAR transfection into T cells, viral vectors have drawbacks [141]. Focusing on the gene delivery step in the manufacturing process by comparing the functional outcomes of both viral and CRISPR-Cas9 gene delivery will allow for a better understanding of how heterogenous the current clinical method is and how impactful the greater control over gene expression afforded by Cas9 may be. Heterogeneity is a vital factor in predicting CAR T cell potency as studies have shown that increased CAR expression on the surface of T cells can cause cells to move off-target, while lower CAR expression can result in less stimulated T cells in response to antigen [81]. The overall goal is to decrease heterogeneity both within a single batch, as well as between batches to engineer more predictable therapies.

The *in vitro* co-culture work will provide information regarding CAR T cell functionality to inform QA/QC during CAR T cell manufacture. Current QA/QC efforts are limited in the clinical manufacturing process and collecting more information on the state of the CAR T cells prior to infusion into the patient will allow for more informed analysis as to why certain patients are complete responders, partial responders, or non-responders. This microwell co-culture system also has the potential to serve as an *in vitro* testing platform for different iterations of new CAR T cell technologies, such as those that involve a more systems biology approach [142], [143].

Finally, the measurements taken from the *in vitro* co-culture studies will inform immune cell mathematical models which will be used to predict *in vivo* results prior to CAR T cell infusion.

The *in vivo* mouse work is required not only to validate the models, but to determine which *in vitro* measurements can best predict the *in vivo* proliferation capacity of the CAR T cells. While it has already been established that proliferation *in vivo* is a strong predictor of remission, identifying other parameters prior to CAR T cell infusion may lead to more reproducible potency and hopefully, more remission in patients [144], [145], [146].

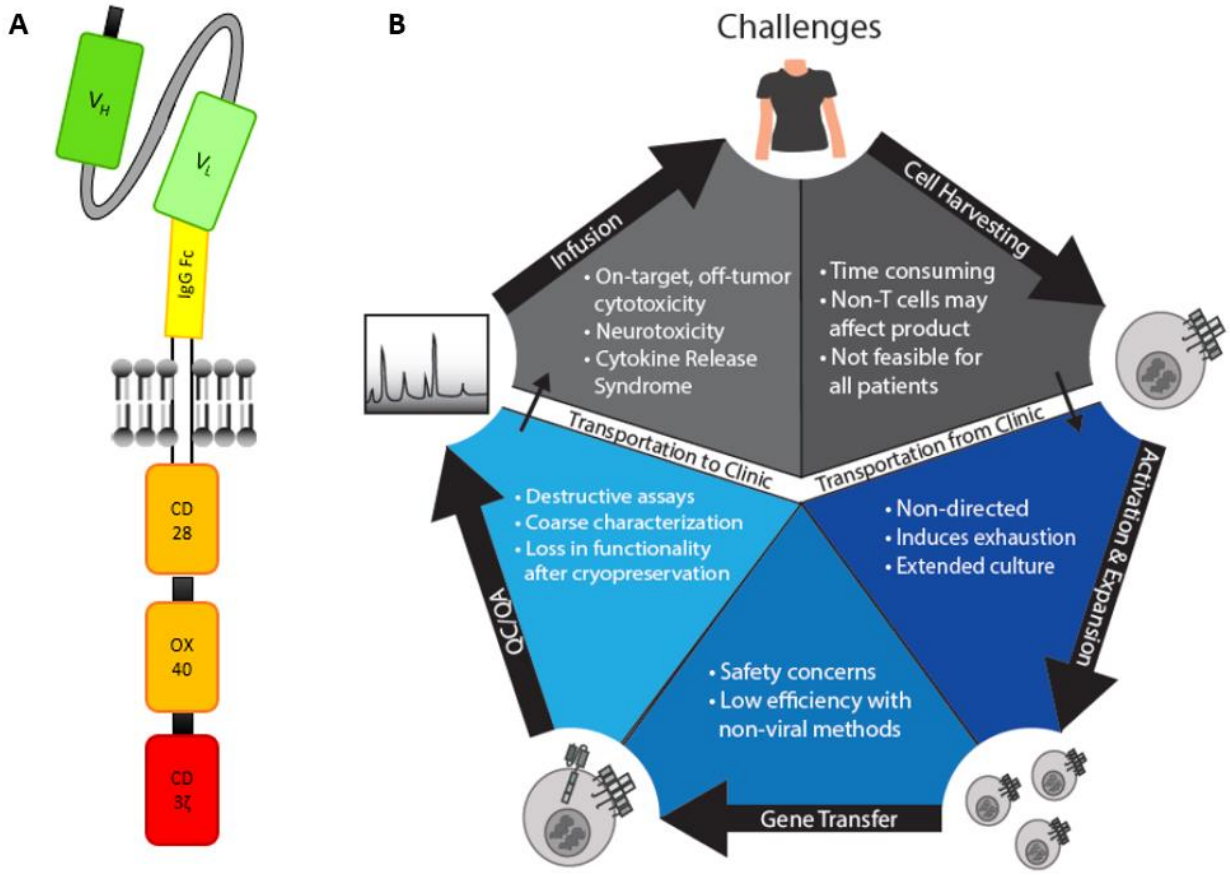

Figure 1.1

A) Schematic of a chimeric antigen receptor. The variable heavy (V_H) and variable light (V_L) chains together make up the single chain variable fragment (scFv) on the external surface of the cell. The scFv is connected through a hinge and a transmembrane region to a series of common T cell signal transmission domains, in this case CD28, CD3Z, and OX40. **B) Diagram of the clinical CAR T cell manufacturing workflow.** The process begins with cell harvesting in the clinic. The cells are then shipped to a manufacturing facility where they are activated and expanded, undergo gene transfer, QA/QC, and are shipped back to the clinic to be infused to the patient.

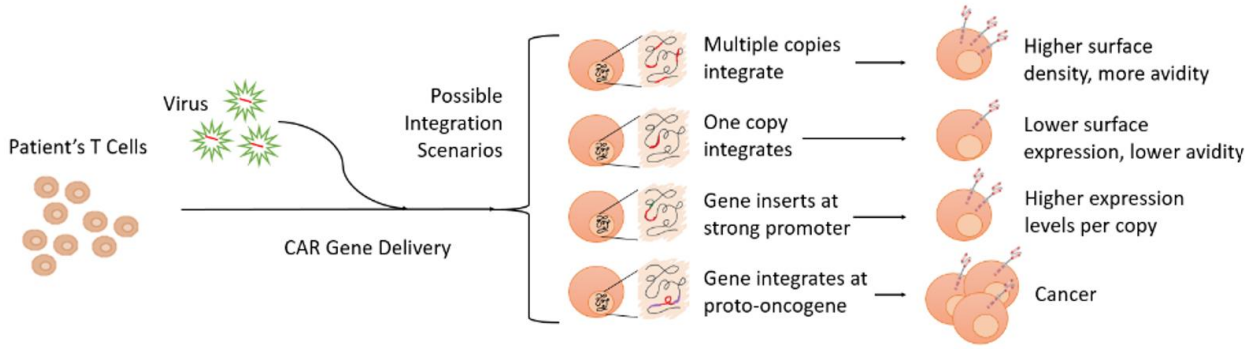

Figure 1.2

Schematic of the different genotypic outcomes that could occur in CAR T cells when manufactured using viruses, and their corresponding potential phenotypic outcomes. Through the use of viruses, a CAR T cell could have multiple copies of the CAR gene integrated leading to higher surface density and thus higher avidity in comparison to a CAR T cell with fewer copies inserted. Location of the CAR insertion, such as near a strong promoter for example, could also lead to altered surface expression. Perhaps the worst possible outcome is if the CAR transgene were to be inserted at a proto-oncogene, thus leading to a cancer of T cells.

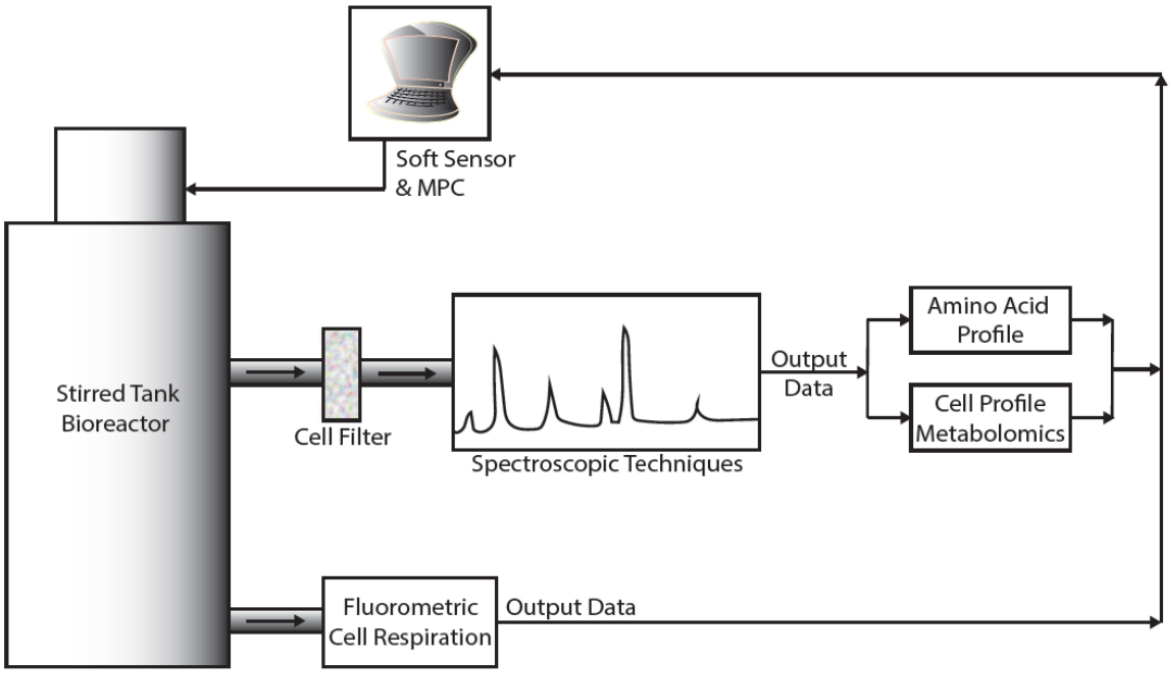

Figure 1.3

Process Analytical Techniques (PAT) and Model Predictive Control (MPC) implementation for CAR T cell populations during manufacturing. Culture medium from the bioreactor is sampled using in-line spectroscopy to determine amino acid composition and metabolite concentrations. Cells from the bioreactor are analyzed using fluorescent techniques to determine their respiratory characteristics. These outputs are combined using modeling to estimate the cellular composition within the bioreactor and modulate medium composition in situ to optimize cell yields.

Table 1

Comparison of Gene Delivery Approaches for CAR T Cell Manufacture. Plus signs indicate positive characteristics associated with each approach while minus signs indicate negative characteristics. More of a given sign implies a higher magnitude of positive or negative characteristic.

	Viruses			Transposons		Targeted Nucleases		
	Lenti	**Retro**	**Adeno**	**Sleeping Beauty**	**Piggybac**	**ZFN**	**TALEN**	**CRISPR-Cas9**
Site-Directed Integration						+++	+++	++
Transfection Efficiency	+++	+	+	++	++	+	+	+
Prevalence in Clinical Trials	+++	+	+	+			+	+
Used for Gene Knockout	+		+			+++	+	+
Insertional Oncogenesis Risk	- - -	- -	- -	- -	- -	-	-	-
Manufacture Costs	- - -	- -	- -	- -	-	-	-	
Random Transgene Integration	- - -	- -	- -	- -	- -	-	-	-

CHAPTER 2: Generation and Characterization of CRISPR-Cas9 Engineered CAR T Cell Products

Portions of the work in this chapter were adapted from:

Rapid non-viral generation of chimeric antigen receptor T cells using CRISPR-Cas9 editing.

Katherine P. Mueller*, Nicole J. Piscopo*, Matthew H. Forsberg, Louise A. Saraspe, Amritava Das, Brittany Russell, Adeela Ali, Cicera R. Lazzarotto, Shengdar Q. Tsai, Christian M. Capitini, Krishanu Saha.

Article submitted.

* *these authors contributed equally*

Abstract

Critical problems in CAR T cell manufacturing with viral vectors arise from imprecise genomic integration, the use of animal components, and supply chain challenges. Here, nonviral CRISPR CAR T cells were manufactured within 9 days using SpyCas9 protein and nucleic acids without any viral vectors. In comparison to retroviral CAR T cells, nonviral CRISPR CAR T cells exhibit *TRAC*-targeted genomic integration of the CAR transgene, less exhaustion and differentiation, a higher dynamic range of activation, decreased detrimental signaling prior to antigen exposure, and potent cytotoxicity against GD2+ neuroblastoma *in vitro* and *in vivo*.

Introduction

Chimeric Antigen Receptor (CAR) T cell therapy is rapidly transforming the treatment of many cancers, with products already approved for some hematologic malignancies. CAR T cells are traditionally manufactured using lentiviruses or γ-retroviruses [2], [54] which confer high-efficiency editing; however, viral transduction methods do not integrate their nucleic acid payloads into a single location within the host genome, risking insertional mutagenesis [2], [148]. In addition, poorly-specified integration of a CAR transgene can lead to heterogeneous and unpredictable CAR expression, which may result in transgene silencing and increased tonic signaling [82]. Good manufacturing practice (GMP)-grade viral vectors and associated quality testing are also prohibitively expensive and constitute a major supply chain bottleneck for the field [149]. Non-viral methods of CAR transduction include transposon-mediated integration [88] and transient mRNA delivery [150]. Like lenti- and retroviruses, transposons also integrate the CAR broadly throughout the genome, while mRNA-mediated delivery is limited to transient expression

over a period of days. Therefore, standard nonviral delivery methods present vexing challenges for CAR T cell manufacturing.

Recently, strategies employing CRISPR/Cas9 editing and viral vectors inserted a CAR transgene into a defined genomic locus, thereby avoiding the risks of insertional mutagenesis and transgene silencing. An anti-CD19 CAR [82] was inserted into exon 1 of the T cell receptor alpha chain (*TRAC*), disrupting expression of the T cell receptor (TCR) while also driving CAR expression from the endogenous *TRAC* promoter. These CAR T cells, engineered through electroporation of Cas9 mRNA followed by delivery a homology-directed repair (HDR) template within an adeno-associated viral (AAV) vector, were potent, retained a memory phenotype, and showed less exhaustion relative to conventional γ-retroviral products. These phenotypes correlate with improved outcomes for patients with hematological malignancies [128], [151]–[157]. Strategies that lead to memory CAR T cell generation with lower exhaustion and terminal differentiation phenotypes have been hypothesized to be beneficial in treating solid tumors, which have typically been refractory to treatment due in part to poor T cell persistence within patients [158]. The use of AAVs to deliver the HDR template needed for CRISPR-mediated transgene insertion [82], [159] is also limited by supply chain challenges associated with viral vector production [149]. Alternate strategies for precise CAR transgene insertion that avoid viral vectors could yield new opportunities to flexibly manufacture CAR T cell immunotherapies.

Efficient nonviral CRISPR/Cas9-mediated TCR replacement in primary human T cells has been demonstrated [104], [160], [161], but it is not clear whether a large synthetic CAR transgene could be integrated using these strategies to reproducibly manufacture functional CAR T cells against solid tumors with clinically-relevant yields. Here, we build upon recent T cell gene editing methods [105], [104] to integrate a 3 kb third-generation anti-disialoganglioside GD2 CAR

transgene at the human *TRAC* locus to report the first completely nonviral CAR T cell product featuring the precise genomic integration of a CAR that has been validated *in vivo*. Our SpyCas9-edited, nonviral (NV)-CAR T cells demonstrate a less differentiated, memory-like phenotype and decreased expression of exhaustion markers relative to conventional retroviral (RV)-CAR T cells, consistent with prior studies with CRISPR-mediated CAR T products manufactured with viral components [82]. In addition, these NV-CAR T cells importantly show less detrimental signaling prior to antigen exposure and comparable potency to retroviral CAR T cells against GD2+ solid tumors *in vivo*.

Results

To avoid use of AAV donor templates, we first cloned a third generation GD2-targeting CAR sequence [162] into a plasmid containing homology arms flanking the desired cut site at the start of the first exon of the *TRAC* locus (**Fig. 2.1a**). The same third generation GD2-targeting CAR sequence was used to generate RV-CAR T cells as a comparison throughout this study. We next generated double-stranded DNA (dsDNA) HDR templates via PCR amplification off the plasmid and performed a two-step purification process to purify and concentrate the templates. Primary human T cells were electroporated with the HDR templates and Cas9 ribonucleoproteins (RNPs) targeting the human *TRAC* locus. Cells were subsequently expanded in xeno-free media and assayed on days 7 and 9 post-isolation (**Fig. 2.1b**). The viability of NV-CAR and RV-CAR T cells was comparably high (>80%) by the end of manufacturing (**Fig. A-1a**). Cell proliferation and growth over 9 days was robust for both groups (**Fig. A-1a**). We assessed gene editing at multiple points post-isolation and achieved higher levels of CAR integration when cells were edited at 48 hours after CD3/CD28/CD2 stimulation (**Fig. A-1b**). As a control, we include an “NV-mCherry”

(NV-mCh) condition in which cells harbor the same disruption of the *TRAC* locus, but with an insertion of a signaling-inert mCherry fluorescent protein in place of the CAR (**Fig. 2.1b**). Using these templates, we achieved consistently high genome editing rates across 31 technical replicates over 4 donors, with CAR integration averaging >15% as measured by flow cytometry (**Fig. 2.1c, d**). The mean fluorescence intensity (MFI) of CAR expression was significantly elevated and showed greater range (~1.6 fold; **Fig. 2.1d**) in the RV-CAR samples in comparison to the NV-CAR samples indicating decreased CAR expression heterogeneity within the NV-CAR product and consistent with prior findings with CRISPR CAR T cells[82]. Within the NV-CAR samples, the TCR was knocked out in 90% of cells (**Fig. 2.1c, e**). We also assayed the immunophenotype by cell surface staining and found significantly elevated CD62L expression in both NV-CAR (CAR+TCR- fraction) and NV-mCh (mCh+TCR- fraction) cells relative to RV-CAR cells (CAR+TCR+ fraction). The mean fluorescence intensity (MFI) of CD62L increased by ~3 fold in the NV-CAR T cells relative to the RV-CAR T cells, indicating a naïve and/or stem cell memory or central memory phenotype in these populations after manufacturing (**Fig. 2.1f**).

Next-generation sequencing of genomic DNA from the manufactured cell products confirmed high rates of indel formation at the *TRAC* locus, averaging 93.06% of reads for NV-CAR samples, and mirroring surface protein levels (**Fig. A-1c, d**). Proper genomic integration of the CAR was confirmed via “in-out” PCR amplification [163] with primers specific to the *TRAC* locus and the transgene (**Fig. 1g, Fig. A-1e**). Highly sensitive genome-wide, off-target analysis for our editing strategy was assayed by CHANGE-seq [164]. The top identified modified locus was the intended on-target site (**Fig. 2.1h, i**) with a rapid drop-off for off-target modifications elsewhere in the genome (**Table A-1**). The CHANGE-seq specificity ratio of our *TRAC* editing strategy is

above average (0.056; 57th percentile) when compared to all editing strategies previously profiled by CHANGE-seq [164].

To further define the phenotypic differences between NV-CAR and RV-CAR T cells, we performed single-cell RNA-sequencing (scRNA-seq) on 29,122 cells from two different donors at the end of the manufacturing process (**Fig. 2.1j**). To distinguish edited transgene-positive and transgene-negative cells within each sample, we aligned reads to a custom reference genome containing an added sequence mapping to the CAR or mCherry transgenes. We detected transgene expression in 6,376 across all samples assayed at the end of manufacturing (22% of assayed cells); and, all subsequent transcriptional analyses were carried out on transgene-positive cells only within each sample. UMAP dimensionality reduction of transgene-positive cells showed similar clustering for both NV-CAR and RV-CAR T cells but not NV-mCh T cells, indicating that the presence of CAR signaling alters the phenotype of the cells even prior to antigen stimulation (**Fig. 2.1k, Fig. A-2a-d**). We observed a variety of differentially expressed genes between both NV-CAR and RV-CAR T cells, and NV-CAR and NV-mCh T cells, which were significant for both donors (p<0.001 cutoff; see also **Fig. A-3a-c** and **Table A-2** for full list of differentially expressed genes between NV-CAR/RV-CAR and NV-CAR/NV-mCh pairs). Gene set enrichment analysis of the 6,209 differentially expressed genes (p<0.001 cutoff) between the CAR-positive T cells from the donor-matched NV-CAR and RV-CAR samples revealed enrichment of T cell activation and innate immune response pathways in the RV-CAR T cells (**Fig. 2.1l**; see **Table A-3** for full list of Reactome pathways), indicating that RV-CAR T cells activate broad signaling in response to the retroviral manufacturing process, CAR transgene, or retroviral vector elements. In comparison, none of these pathways were significantly enriched when comparing transgene-positive NV-CAR T cells to NV-mCh T cells (**Fig. 2.1l**). Transgene-positive RV-CAR T cells

exhibited elevated levels of transcripts associated with an exhausted T cell signature (high *CTLA4, ENTPD1, LAG3, TIGIT, CD244*; **Fig. 2.1l**) relative to transgene-positive NV-CAR T cells, but there were minimal significant differences in the exhaustion transcriptional profile between transgene-positive, donor-matched NV-CAR and NV-mCh T cells (**Fig. A-4a**). Finally, we observed no significant changes in transcript levels for genes at or within 5 kb of off-target sites predicted by CHANGE-seq (**Table A-1**), indicating that any potential genomic disruptions at these sites did not lead to detectable changes in proximal transcripts.

On day 9 of manufacturing, cytokine production levels were measured from the conditioned culture media. Prior to antigen exposure, RV-CAR T cells had higher levels of IFNγ, TNFα, IL-2, IL-4, IL-10, and IL-13, in comparison to both the NV-CAR and NV-mCh T cells (**Fig. 2.1m**). This result is consistent with the above transcriptional analysis showing hyperactive CAR signaling and recent observations that some RV-CAR T cells display elevated levels of tonic signaling prior to antigen exposure [128]. After a 24 h co-culture between the engineered T cells and GD2+ CHLA20 neuroblastoma, NV-CAR T cells either matched or surpassed the level of cytokine production of the RV-CAR T cells (**Fig. 2.2a**), indicating that NV-CAR T cells were capable of mounting a response to their target antigen, and suggesting that the RV-CAR T cells may be more exhausted prior to antigen exposure than the NV-CAR T cells. These trends, both pre-antigen exposure and post-antigen exposure, were also observed for IL-6, IL-1β and IL-12p70, but not for IL-8 (**Fig. A-4c** and **Fig. A-5a**).

After characterizing cellular phenotypes and gene expression at the end of the manufacturing process, we measured the *in vitro* potency of NV-CAR T cells against two GD2+ solid tumors: CHLA20 neuroblastoma and M21 melanoma (**Fig. A-5b**). We observed robust killing using a 5:1 effector:target ratio for both NV-CAR and RV-CAR T cells (**Fig. 2.2b, Fig. A-**

5c). We again performed scRNA-seq on T cells that were co-cultured with CHLA20 neuroblastoma for 24 hours (**Fig. 2.2c, d**). Gene set enrichment analysis of the 1,588 differentially expressed genes (p<0.001 cutoff) between the transgene-positive T cells from the NV-CAR and NV-mCh samples revealed high activation of T cell activation pathways in transgene-positive NV-CAR T cells (**Fig. 2.2e**), specifically CD28 activation pathways involving the CAR. When comparing the enrichment scores of pathways within CAR-positive cells between NV-CAR/RV-CAR paired samples, lower differences were observed in T cells post-antigen exposure relative to pre-antigen exposure (**Fig. 2.2e** vs. **Fig. 2.1l; Fig. A-4b**). These results, corroborated by elevated cytokine production observed after CHLA20 co-culture (**Fig. 2.2a**), demonstrate that NV-CAR T cells can properly achieve high levels of activation upon antigen exposure, while avoiding potentially detrimental high tonic-signaling prior to antigen exposure.

Finally, we assessed CAR T cell potency *in vivo* in an established human GD2+ neuroblastoma xenograft model. After 9 total days of culture, multiple replicate wells of RV-CAR, NV-CAR, or NV-mCh T cells were pooled for injection into NOD-SCID-$\gamma c^{-/-}$ (NSG) mice. Ten million T cells were delivered via tail vein injection to each NSG mouse with an established luciferase-expressing CHLA20 neuroblastoma tumor identified by bioluminescence (**Fig. 2.2f**). Tumor sizes were quantified over time by IVIS imaging and digital caliper (**Fig. 2.2g**). Both CAR-treated cohorts showed robust tumor regression in the first 3 weeks post-infusion (**Fig. 2.2h, Fig. A-6a, b**). These cohorts also showed significantly improved survival as compared to NV-mCh-treated mice; however, there was no significant difference in survival between NV-CAR and RV-CAR treated mice by day 80 (p-value=0.4099, n.s.). The percentage of CAR+ cells per dose was lower in NV-CAR T cells, which may have contributed to a slight decrease in complete remission rates (5/8 RV-CAR vs. 4/9 NV-CAR) but had no significant impact on overall survival, suggesting

enhanced potency of the CAR-positive NV-CAR T cells. None of the control NV-mCh mice showed tumor regression, and all seven mice died of tumor progression by day 60. We also assessed persistence, memory and exhaustion phenotypes in T cells isolated from spleens and tumors. NV-CAR T cells persisted in both the spleens and tumors of the treated mice, but not for NV-mCh T cell treatments, indicating successful trafficking of NV-CAR T cells to the tumor microenvironment (**Fig. 2.2i, Fig. A-6c-f**). Additionally, we observed that cells in the spleen had lower levels of PD-1 and TIM-3 exhaustion markers after NV-CAR treatment relative to the RV-CAR treatment (**Fig. 2.2j**), suggesting that the higher CAR MFI on RV-CARs (**Fig. 2.1d**) and detrimental signaling after expansion **(Fig. 2.1l)** could be contributing to increased propensity for exhaustion in RV-CARs. These findings demonstrate comparable potency of NV-CAR T cells to standard RV-CAR T cells, establishing the potential clinical relevance of NV-CAR T cells.

Discussion

Overall, we describe a rapid 9-day manufacturing of third generation GD2-specific CAR T cells using recombinant SpyCas9 protein and nucleic acids which results in stable, genomically-integrated, durable CAR expression (>80 days *in vivo*) without the use of any viral vectors. NV-CAR T cells exhibit proper *TRAC*-specific integration of the CAR transgene and an increased percentage and expression level of CD62L relative to conventional strategies. Robust upregulation of gene transcripts prevalent in cytotoxic transcriptional programs and secretion of pro-inflammatory cytokines like IFNγ and TNFα occur only after target antigen exposure, in contrast to conventional RV-CAR T cells that exhibit detrimental signaling during manufacturing. After injection into a GD2+ human neuroblastoma xenograft model, NV-CAR T cells induce strong regression of solid tumors compared to mock-edited T cells, and at levels comparable to RV-CAR

T cells. NV-CAR T cells show reduced propensity to exhaustion at the gene expression and protein levels before antigen exposure, and at the protein level after antigen exposure.

Relative to conventional T cell manufacturing, our streamlined, nonviral manufacturing process could: *1)* reduce the batch-to-batch variability, supply chain challenges, and costs associated with vector production [54], [165] (see **Table A-4**); *2)* alleviate a number of regulatory considerations (e.g., the need to monitor replication competency of the vector and the levels of xenogeneic components in the clinical cell product, notably plasmid DNA and serum during cell culture that can introduce infectious agents or toxic components [166]; and *3)* eliminate the potential for integration of viral elements into the human genome, which can generate a high degree of gene perturbation, up to 10^4-10^5 different insertional sites within a single product [148]. Integration of the vector, in particular, presents risks of insertional oncogenesis [167], transgene silencing or overexpression, and adverse immune response to the vector, which could result in the rejection of therapeutic cells. While off-target analysis of genome editors is necessary for any clinical translation of our approach, there are now many experimental and computational tools that can readily be used for this purpose [164], [168] and next-generation high-fidelity Cas9 enzymes [169] could be used to further decrease the potential for any off-target effects. Our fully-defined, nonviral manufacturing method therefore has high potential to enable the rapid and flexible manufacture of highly-defined and highly-potent CAR T cell products.

Acknowledgments

We thank members of the Saha and Capitini labs and John Hosmer-Quint for helpful discussion and comments on the manuscript, the University of Wisconsin (UW) Carbone Cancer Center Flow Cytometry Laboratory for assistance with flow cytometry experiments, and Aldevron for technical

support with Cas9 proteins. We thank Tyler Duellman and the UW Biotechnology Center for scRNA-seq library preparation and experimental design assistance. We thank Malcolm Brenner (Baylor College of Medicine) for sharing of the RV-CAR plasmid, Paul Sondel and the National Cancer Institute for 1A7 anti-CAR antibody, James Thomson and Jue Zhang (Morgridge Institute for Research) for the AkaLUC-GFP CHLA20 cancer line used for *in vivo* studies, and Sushmita Roy, Sunnie Grace McCalla, Madeline Smerchansky and Kurt Mueller for helpful discussions and assistance with scRNA-seq analysis. We acknowledge generous support from the National Science Foundation CBET-1645123 (CMC and KS), AWD-101645-G3/RJ375-G3 (KS), and NSF Graduate Research Fellowship Program DGE-1747503, to K.P.M and N.J.P.); National Institutes of Health/National Cancer Institute R01 CA215461 (CMC), National Institute of General Medical Sciences R35 GM119644-01 (KS), Biotechnology Training Program T32GM008349 (K.P.M); University of Wisconsin Carbone Cancer Center Support Grant P30 CA014520 Cell Based Immunotherapy Supplement (CMC and KS); St. Baldrick's – Stand up to Cancer Pediatric Dream Team Translational Research Grant SU2C-AACR-DT-27-17 (CMC); American Cancer Society Research Scholar grant RSG-18-104-01-LIB (CMC); and the MACC Fund (CMC). Stand Up to Cancer is a division of the Entertainment Industry Foundation. Research grants are administered by the American Association for Cancer Research, the Scientific Partner of SU2C. The contents of this article do not necessarily reflect the views or policies of the Department of Health and Human Services, nor does mention of trade names, commercial products, or organizations imply endorsement by the US Government.

Authors' contributions: These authors contributed equally: K.P.M. and N.J.P. K.P.M. and L.A.S. designed and cloned the NV-CAR and NV-mCh plasmids. K.P.M. and N.J.P. isolated and cultured

T cells, and performed nonviral transfections. K.P.M. and A.D. performed viral transductions. K.P.M. performed and analyzed scRNA-seq experiments. M.F., L.A.S., and A.D. performed flow cytometry. N.J.P. and B.R. performed and analyzed NGS. N.J.P and M.F. performed cytokine experiments and N.J.P. analyzed cytokine data. M.F. conducted *in vivo* experiments. K.P.M., N.J.P. and A.A. performed *in vitro* co-cultures. K.P.M. and N.J.P. wrote the manuscript with input from all authors. S.T., K.S. and C.M.C. supervised the research. K.P.M., N.J.P., M.F., L.A.S., C.L., A.D., A.A., and B.R. performed experiments and analyzed the data.

Conflicts of interest: K.P.M., N.J.P., M.H.F., L.A.S., A.D., C.M.C. and K.S. are inventors on a patent application related to this manuscript. No other conflicts of interest are reported.

Methods

Data Availability. The data that support the findings of this study will be made available in the public domain upon publication.

Data Reporting. The Reporting Summary document includes information about the statistics, software, data, and sample preparation methods used for this study. For *in vivo* experiments, established tumor burden was verified by IVIS luciferase imaging prior to infusion. Mice were arranged according to tumor burden and distributed evenly across conditions. The experiments were not randomized and the investigators were not blinded during experiments and outcome assessment.

Antibodies. Antibodies and titrations used in this study for flow cytometry and fluorescence-activated cell sorting are listed in **Table A-5**.

Guide RNAs. All guide RNAs used in this study are listed in **Table A-6**.

Primers. All primers used in this study are listed in **Table A-6**.

Cell lines. CHLA20 human neuroblastoma cells were a gift from Dr. Mario Otto and M21 human melanoma cells were a gift from Dr. Paul Sondel (University of Wisconsin-Madison). These cells were maintained in Dulbecco's Modified Eagle Medium high glucose (Gibco) supplemented with 10% Fetal Bovine Serum (Gibco) and 1% Penicillin-Streptomycin (Gibco). AkaLUC-GFP CHLA20 cells were a gift from Dr. James Thomson (Morgridge Institute for Research). Phoenix cells (ATCC) for viral preparation were maintained in DMEM (high glucose) supplemented with 10% Fetal Bovine Serum (Gibco), and selected using 1 μg/mL diphtheria toxin (Cayman Biologics) and 300 μg/mL hygromycin (Thermo Fisher Scientific) prior to use. Selection for transgene positive cells was confirmed by flow cytometry for mouse Lyt2 expression (Biolegend)

(>70%+). 3T3 cells were maintained in Dulbecco's Modified Eagle Medium (Gibco) supplemented with 10% Fetal Bovine Serum (Gibco) and 1% Penicillin-Streptomycin (Gibco). Cell authentication was performed using short tandem repeat analysis (Idexx BioAnalytics, Westbrook, ME) and per ATCC guidelines using morphology, growth curves, and *Mycoplasma* testing within 6 months of use using the e-Myco mycoplasma PCR detection kit (iNtRON Biotechnology Inc, Boca Raton, FL). Cell lines were maintained in culture at 37°C in 5% CO_2, and used after 3-5 passages in culture after thawing.

Plasmid constructs. NV-*TRAC*-CAR: A 2kb region surrounding the *TRAC* locus was amplified by PCR from human genomic DNA and cloned into a pCR blunt II TOPO backbone (Thermo Fisher Scientific). The CAR transgene from a pSFG.iCasp9.2A.14G2A-CD28-OX40-CD3z RV-CAR plasmid (gift from Dr. Malcolm Brenner, Baylor College of Medicine) was then cloned into the TOPO *TRAC* vector using Gibson Assembly (New England Biolabs (NEB)). Plasmid sequence was verified by Sanger sequencing. NV-TRAC-mCherry was designed, synthesized, and sequence-verified (GenScript). All plasmids were grown in 5-alpha competent *E. coli* (NEB) and purified using the PureYield MidiPrep system (Promega).

Double-stranded DNA HDR template production. Plasmid donors were used as PCR templates for NV products. In brief, NV-CAR and NV-mCh plasmids were MidiPrepped using the PureYield MidiPrep system (Promega). PCR amplicons were generated from plasmid templates using Q5 Hot Start Polymerase (NEB), and pooled into 100 µl reactions for Solid Phase Reversible Immobilization (SPRI) cleanup (1X) using AMPure XP beads according to the manufacturer's instructions (Beckman Coulter). Each 100 µl starting product was eluted into 5 µl of water. Bead incubation and separation times were increased to 5 minutes, and elution time was increased to 15 minutes at 37°C to improve yield. PCR products from round 1 cleanup were pooled and subjected

to a second round of SPRI cleanup (1X) to increase total concentration; round 2 elution volume was 20% of round 1 input volume. Template concentration and purity was quantified using NanoDrop 2000 and Qubit dsDNA BR Assays (Thermo Fisher Scientific), and templates were diluted in water to an exact concentration of 2 µg/µl.

SpyCas9 RNP preparation. RNPs were produced by complexing a two-component gRNA to SpyCas9. In brief, tracrRNA and crRNA were ordered from IDT, suspended in nuclease-free duplex buffer at 100 µM, and stored in single-use aliquots at -80°C. tracrRNA and crRNA were thawed, and 1 µl of each component was mixed 1:1 by volume and annealed by incubation at 37°C for 30 minutes to form a 50 µM gRNA solution in individual aliquots for each electroporation replicate. Recombinant sNLS-SpCas9-sNLS Cas9 (Aldevron, 10 mg/ml, total 0.8 µl) was added to the complexed gRNA at a 1:1 molar ratio and incubated for 15 minutes at 37°C to form an RNP. Individual aliquots of RNPs were incubated for at least 30 seconds at room temperature with HDR templates for each sample prior to electroporation.

Isolation of primary T cells from healthy donors. This study was approved by the Institutional Review Board of the University of Wisconsin-Madison (#2018-0103), and informed consent was obtained from all donors. Peripheral blood was drawn from healthy donors into sterile syringes containing heparin, and transferred to sterile 50 mL conical tubes. Primary human T cells were isolated using negative selection per the manufacturer's instructions (RosetteSep Human T Cell Enrichment Cocktail, STEMCELL Technologies). T cells were counted using a Countess II FL Automated Cell Counter (Thermo Fisher Scientific) with 0.4% Trypan Blue viability stain (Thermo Fisher Scientific). T cells were cultured at a density of 1 million cells/mL in ImmunoCult-XF T cell Expansion Medium (STEMCELL) supplemented with 200 U/mL IL-2 (Peprotech) and

stimulated with ImmunoCult Human CD3/CD28/CD2 T cell Activator (STEMCELL) immediately after isolation, per the manufacturer's instructions.

T cell culture. Bulk T cells were cultured in ImmunoCult-XF T cell Expansion Medium at an approximate density of 1 million cells/mL. In brief, T cells were stimulated with ImmunoCult Human CD3/CD28/CD2 T cell Activator (STEMCELL) for 2 days prior to electroporation. On day 3, (24 hours post-electroporation), NV-CAR and NV-mCh T cells were transferred without centrifugation to 1 mL of fresh culture medium (with 500 U/mL IL-2, without activator) and allowed to expand. T cells were passaged, counted, and adjusted to 1 million/mL in fresh medium + IL-2 on days 5 and 7 after isolation. RV-CAR T cells were spinoculated with RV-CAR construct on day 3 and passaged on day 5 along with the NV-CAR and NV-mCh T cells. Prior to electroporation or spinoculation, the medium was supplemented with 200 U/mL IL-2; post-gene editing, medium was supplemented with 500 U/mL IL-2 (Peprotech).

T cell electroporation. RNPs and HDR templates were electroporated 2 days after T cell isolation and stimulation. During crRNA and tracrRNA incubation, T cells were centrifuged for 3 minutes at 200g and counted using a Countess II FL Automated Cell Counter with 0.4% Trypan Blue viability stain (Thermo Fisher). 1 million cells per replicate were aliquoted into 1.5 mL tubes. During the RNP complexation step (see RNP production), T cell aliquots were centrifuged for 10 min at 90g. During the spin step, 2 µl HDR template (total 4 µg) per condition were aliquoted to PCR tubes, followed by RNPs (2.8 µl per well; pipette should be set to a higher volume to ensure complete expulsion of viscous solution). Templates and RNPs were incubated at room temperature for at least 30 seconds. After cell centrifugation, supernatants were aspirated, and cells were resuspended in 20 µl P3 buffer (Lonza), then transferred to PCR tubes containing RNP, bringing the total volume per sample to 24 µl. Each sample was transferred directly to a 16 well

electroporation cuvette. Typically, no more than 8 reactions were completed at a time to minimize the amount of time T cells spent in P3 buffer. T cells were electroporated with a Lonza 4D nucleofector with X Unit using pulse code EH115. Immediately after nucleofection, 80 µl of pre-warmed media with 500 U/mL IL-2 and 25 µl/mL ImmunoCult CD3/CD28/CD2 activator was added to each well of the cuvette. Cuvettes were rested at 37°C in the cell culture incubator for 15 minutes. After 15 minutes, cells were moved to 200 µl total volume of media with IL-2 and activator (see above) in a round bottom 96 well plate.

Retrovirus production. CAR retrovirus was manufactured using Phoenix cells (ATCC). In brief, pSFG.iCasp9.2A.14G2A-CD28-OX40-CD3z plasmid was MidiPrepped using the PureYield MidiPrep system (Promega). One day prior to transfection, selected Phoenix cells were plated on 0.01% Poly-L-Lysine coated 15 cm dishes (Sigma Aldrich) at a density of 76,000 cells/cm^2, or ~65% confluency. On transfection day, media was replaced 1 hour prior to transfection of 10 µg pSFG.iCasp9.2A.14G2A-CD28-OX40-CD3z plasmid/plate using iMFectin according to the manufacturer's instructions (GenDEPOT). Media was replaced 18-24 hours later with 10 mL of 50 mM HEPES buffered DMEM + 10% FBS (Gibco). 48 hours later, media was collected, stored at 4°C, and replaced. A second aliquot of media was collected 24 hours later; media aliquots were pooled and centrifuged for 10 min at 2000g to pellet contaminating cells, and supernatants were transferred to a clean conical tube. 1/3 volume Retro-X concentrator (Takara) was added, and supernatants were refrigerated at 4°C for 12-18 hours, then concentrated according to the manufacturer's instructions. Viruses were tested on 3T3 cells prior to use; yields from one 15 cm dish were used for 5 replicate wells of 160,000 T cells per transduction. Viruses were either used immediately for T cell spinoculation or stored at -80°C in single use aliquots.

Retroviral transduction. T cells for RV infection were cultured similarly to NV-CAR and NV-mCh T cells, with two exceptions: 1) T cells were passaged and resuspended without ImmunoCult CD2/CD28/CD3 activator on day 2 post-isolation, and spinoculated on Day 3. RV-CAR T cells returned to the regular passaging schedule on day 5 post-isolation (See **Fig. 2.1b**). Prior to spinoculation, non-tissue culture treated 24 well plates were coated with Retronectin according to the manufacturer's instructions (Takara/Clontech). On day 3 post-isolation, T cells were centrifuged at 200 g for 3 minutes, counted, and resuspended to a concentration of 200,000 cells/mL, then stored in the incubator until plates were prepared. Virus was added to retronectin-coated plates in a volume of 400 µl virus in ImmunoCult medium and centrifuged at 2000g for 2 hours at 32°C. 160,000 T cells in 800 µl were added to each well and spinoculated at 2000g for 60 minutes at 32°C, brake off. T cells were then transferred to the incubator and left undisturbed for two days.

Flow cytometry and fluorescence activated cell sorting. CAR was detected using 1A7 anti-14G2a idiotype antibody (gift from Paul Sondel) conjugated to APC with the Lightning-Link APC Antibody Labeling kit (Novus Biologicals). T cells were stained in BD Brilliant Stain Buffer (BD Biosciences). For panels including TRAC and CD3, cells were permeabilized and fixed using the BD Cytofix/Cytoperm Plus kit according to the manufacturer's instructions. Flow cytometry was performed on an Attune NxT Flow cytometer (Thermo Fisher Scientific), and fluorescence-activated cell sorting was performed on a FACS Aria (BD). All antibodies used in this study are described in **Table A-5**. T cells from Donors 1 and 2 were stained and analyzed on day 9 of manufacture using fresh cells. For donors 3 and 4, only TCR, CAR, and CD62L were measured on day 9 of manufacture. The change in protocol was made due to equipment restrictions related

to institutional COVID-19 biosafety precautions, and CD62L was selected for analysis due to the known effects of cryopreservation on expression levels[170].

"In-Out PCR". Genomic DNA was extracted from 100,000 cells per condition using DNA QuickExtract (Lucigen), and incubated at 65°C for 15 min, 68°C for 15 min, and 98°C for 10 min. Genomic integration of the CAR was confirmed by In-out PCR using a forward primer upstream of the *TRAC* left homology arm, and a reverse primer binding within the CAR sequence. Primer sequences are listed in **Table A-6**. PCR was performed according to the manufacturer's instructions using Q5 Hot Start Polymerase (NEB) using the following program: 98°C (30 s), 35 cycles of 98°C (10 s), 62°C (20 s), 72°C (2 min), and a final extension at 72°C (2 min).

Next Generation Sequencing of genomic DNA. Indel formation at the *TRAC* locus was measured using Next Generation Sequencing (Illumina). Genomic PCR was performed according to the manufacturer's instructions using Q5 Hot Start polymerase (NEB); primers are listed in **Table A-6**. Products were purified using SPRI cleanup with AMPure XP beads (Beckman Coulter), and sequencing indices were added with a second round of PCR using indexing primers (Illumina), followed by a second SPRI cleanup. Samples were pooled and sequenced on an Illumina MiniSeq according to the manufacturer's instructions. Analysis was performed using CRISPR RGEN (rgenome.net).

G**enome-wide, off-target analysis.** Genomic DNA from human primary $CD4^+$/$CD8^+$ T cells was isolated using Gentra Puregene Kit (Qiagen) according to the manufacturer's instructions. CHANGE-seq was performed as previously described[164]. Briefly, purified genomic DNA was tagmented with a custom Tn5-transposome to an average length of 400 bp, followed by gap repair with Kapa HiFi HotStart Uracil+ DNA Polymerase (KAPA Biosystems) and Taq DNA ligase (NEB). Gap-repaired tagmented DNA was treated with USER enzyme (NEB) and T4

polynucleotide kinase (NEB). Intramolecular circularization of the DNA was performed with T4 DNA ligase (NEB) and residual linear DNA was degraded by a cocktail of exonucleases containing Plasmid-Safe ATP-dependent DNase (Lucigen), Lambda exonuclease (NEB) and Exonuclease I (NEB). *In vitro* cleavage reactions were performed with 125 ng of exonuclease-treated circularized DNA, 90 nM of SpCas9 protein (NEB), NEB buffer 3.1 (NEB) and 270 nM of sgRNA, in a 50 µL volume. Cleaved products were A-tailed, ligated with a hairpin adaptor (NEB), treated with USER enzyme (NEB) and amplified by PCR with barcoded universal primers NEBNext Multiplex Oligos for Illumina (NEB), using Kapa HiFi Polymerase (KAPA Biosystems). Libraries were quantified by qPCR (KAPA Biosystems) and sequenced with 151 bp paired-end reads on an Illumina NextSeq instrument. CHANGE-seq data analyses were performed using open-source CHANGE-seq analysis software (https://github.com/tsailabSJ/changeseq).

Cytokine Analysis. Cytokine analysis was performed using a V-PLEX Proinflammatory Panel 1 Human Kit (Meso Scale Discovery, Catalog No K15049D-2) according to the manufacturer's protocol. Measured cytokines include IFNγ, IL-1β, IL-2, IL-4, IL-6, IL-8, IL-10, IL-12p70, IL-13, and TNF-α. In brief, media was collected from the final day of cell culture before injection into mice and flash frozen and stored at -80°C. For co-culture samples, 250,000 T cells were co-cultured with 50,000 cancer cells in 250 µl ImmunoCult XF T cell expansion medium for 24 hours prior to media collection. On the day of the assay, media was thawed and 50 µl of media was used to perform all measurements in duplicate. Figures were produced using GraphPad PRISM 8. Data were normalized by calculating cytokine production per cell based on the total concentration of cells calculated at media collection.

***In Vitro* Cytotoxicity Assays.** *For Fig. 2b:* 10,000 AkaLUC-GFP CHLA20 cells were seeded in triplicate per condition in a 96 well flat bottom plate. 48 hours later, 50,000 T cells were added to

each well. 1 µl (0.05 µg) of CF® 594 Annexin V antibody (Biotium) was added to the wells. The plate was centrifuged at 100g for 1 minute and then placed in The IncuCyte® S3 Live-Cell Analysis System (Sartorius, Catalog No 4647), stored at 37°C, 5% CO_2. Images were taken every 2 hours for 48 hours. Green object count was used to calculate the number of cancer cells in each well. Red object count was used to calculate the number of objects staining positive for Annexin V, an early apoptosis marker. Fluorescent images were analyzed with IncuCyte Base Analysis Software. *For Extended Data Fig. 5c:* 10,000 AkaLUC-GFP CHLA20 cells or 10,000 H2B-mCherry M21 cells were seeded in triplicate per condition in a 96 well flat bottom plate. 24 hours later, 50,000 T cells were added to each well. The 96 well plate was placed in a live cell imaging chamber at 37°C and 5% CO_2 and imaged on a Nikon Epifluorescent scope, with images taken every 12 hours for 48 hours.

Single cell RNA sequencing. 24 hours prior to assay, 200,000 AkaLUC-CHLA20 cells were plated in 12 well plates and cultured overnight. One week after electroporation (day 9 post-isolation), T cells were counted and pooled into a single bank for characterization studies (scRNA-seq, IncuCyte cytotoxicity assay and *in vivo* experiments). Media was aspirated from cancer cells, and 1 million T cells in ImmunoCult-XF Medium + 500 U/mL IL-2 were seeded on the cancer cells, then cultured for 24 hours. A parallel T cell-only single culture (termed “pre-antigen”) was set up at the same density in a separate 12 well plate. The next day, co-culture cells were trypsinized for donor 1 and washed off the plate with media, and cells were singularized with a 35 µM cell strainer (Corning). For donor 2, co-culture cells were stained for CD45 and CAR, and FACS sorted into $CD45^+CAR^+$ and $CD45^+CAR^-$ fractions prior to sample submission. Cells were counted with a Countess II FL cell counter using trypan blue exclusion (Thermo Fisher Scientific), and samples were prepared for single cell RNA sequencing with the 10X Genomics 3’ kit (v3

chemistry) according to the manufacturer's instructions. Libraries were sequenced using the Illumina NovaSeq 6000 system. FASTQ files were aligned with Cellranger v3.0.1 to custom reference genomes that included added sequences for the transgene(s) used in each culture condition (e.g., the *TRAC* NV-CAR donor sequence, mCherry donor sequence, etc.). Downstream analyses were performed using Seurat 3. In brief, each dataset was filtered to include only cells with 200 or more unique genes, and genes expressed in three or more cells. Data were normalized and scaled, and mitochondrial mapping percentage was regressed out as a confounding source of variation. Datasets were then integrated, and dimensionality reduction was performed with Principal Components Analysis. Cells were clustered based on their genome-wide transcriptional profiles using Uniform Manifold Approximation and Projection (UMAP), and differential gene expression was calculated using Seurat 3. For each sample, cells either expressing the transgene of interest (CAR or mCherry) were identified, and transgene-negative cells were removed from the dataset. Differentially expressed genes across sample pairs in **Fig. A-3** were determined by identifying all significant differentially expressed genes for each donor ($p<0.001$), then identifying the intersection of genes that were significantly differentially expressed in both donors. All cells from each sample type were then pooled from both donors, and differential expression was recalculated for each sample pair (**Fig. A-3**). All analysis scripts will be deposited in the Saha Lab GitHub repository upon publication.

Gene set enrichment analysis (GSEA). GSEA[171] was performed using the natural log-fold change values between sample pairs, using only the set of transgene-positive cells in each dataset. GSEA v.4.0.3 (Broad Institute) with the v7.1 Reactome signatures database from MSigDB was used with default parameters (1000 permutations). Data were exported and graphed in Microsoft Excel.

***In vivo* human neuroblastoma xenograft mouse model.** All animal experiments were approved by the University of Wisconsin-Madison Animal Care and Use Committee (ACUC). Male and female NSG mice (9-25 weeks old) were subcutaneously injected with 10 million AkaLUC-GFP CHLA20 human neuroblastoma cells in the side flank to establish tumors. Six days later (Day 0), established tumors were verified by bioluminescence with the PerkinElmer *In Vivo* Imaging System (IVIS), and 10 million T cells were injected through the tail vein into each mouse. Mice were followed for weight loss and overall survival. On imaging days, mice were sedated using isoflurane and received intraperitoneal injections of ~120 mg/kg D-luciferin (GoldBio). Fifteen minutes later, mice were imaged via IVIS. Imaging was repeated every 3 to 4 days, starting 1 day before initial T cell injection (Day -1). Mice were injected with 100,000 IU of human IL-2 subcutaneously on day 0, day 4, and with each subsequent IVIS reading. In order to quantify the total flux in the IVIS images, a region of interest (ROI) was drawn around the bottom half of each mouse with the total flux being calculated by Living Image® software (PerkinElmer; Total flux = the radiance (photons/sec) in each pixel summed or integrated over the ROI area (cm^2) x 4π). The absolute minimum total flux value was subtracted from each image to minimize background signal. For donors 1, 3, and 4, mice were maintained until tumors reached 20mm in any dimension by digital caliper as defined by the ACUC.

Flow cytometric analysis of splenic and tumor-infiltrating T cells. For donor 2, all mice were euthanized on day 25. Tumors and spleens were removed, mechanically dissociated, and passed through a Corning® 35µm cell strainer. Cell suspensions were centrifuged at 300g for 10 minutes, and then digested with ACK lysing buffer (Lonza). The cells were then washed and centrifuged at 300g for 10 minutes, and then resuspended in 10 ml PBS, 10 µl of which was added to 10 ml of ISOTON® diluent and counted on the COULTER COUNTER® Z1 Series Particle Counter

(Beckman Coulter). From this count, $1x10^6$ cells were added to flow cytometry tubes in staining buffer (PBS with 2% FBS) and stained with antibodies for hCD45, mCD45, scFV 14G2a CAR, and PD-1 (see **Table A-5 for antibody information**). The cells were then washed with PBS, centrifuged at 300g for 10 minutes, and 0.5ul of Ghost Dye™ Red 780 viability dye (Tonbo Biosciences) was added for 20 minutes at room temperature. Cells were then washed with staining buffer, spun down, and resuspended in 400 µl of staining buffer. Cells were then run on an Attune™ NXT flow cytometer (Thermo Fisher Scientific). Subsequent analysis was performed using Flowjo™ software (BD). For donors 3 and 4, spleens and tumors were analyzed as mice reached euthanasia criteria and were stained with an extended antibody panel outlined in **Table A-5**.

Statistical analysis. Unless otherwise specified, all analyses were performed using GraphPad Prism (v.8.0.1), and error bars represent mean +- SD; ns = $p>=0.05$, * for $p<0.05$, ** for $p<0.01$, *** for $p<0.001$,**** for $p<0.0001$. For Fig. 2b, error bars show SEM. Statistical analyses for cytokine data (Figure 1m, Figure 2a, Extended Data Figure 1e, Extended Data Fig 2a) were performed using a two-tailed Mann-Whitney test in GraphPad Prism. All box plots show median (horizontal line), interquartile range (hinges), and smallest and largest values (whiskers). Statistical significance for differential gene expression was determined with Seurat 3 using the non-parametric Wilcoxon rank sum test. All 11 scRNA-seq samples were integrated and normalized, and 2 replicate samples per donor were combined to calculate differential expression between transgene-positive cells in each sample type. P values were adjusted using Bonferroni correction. $p<0.001$ was used as the threshold for assigning significant versus non-significant changes in gene expression. Volcano plots were generated in RStudio (v 1.1.456) using the ggplot2 and

EnhancedVolcano packages. Statistical significance for Fig. 2h was calculated using the Mantel-Cox Test.

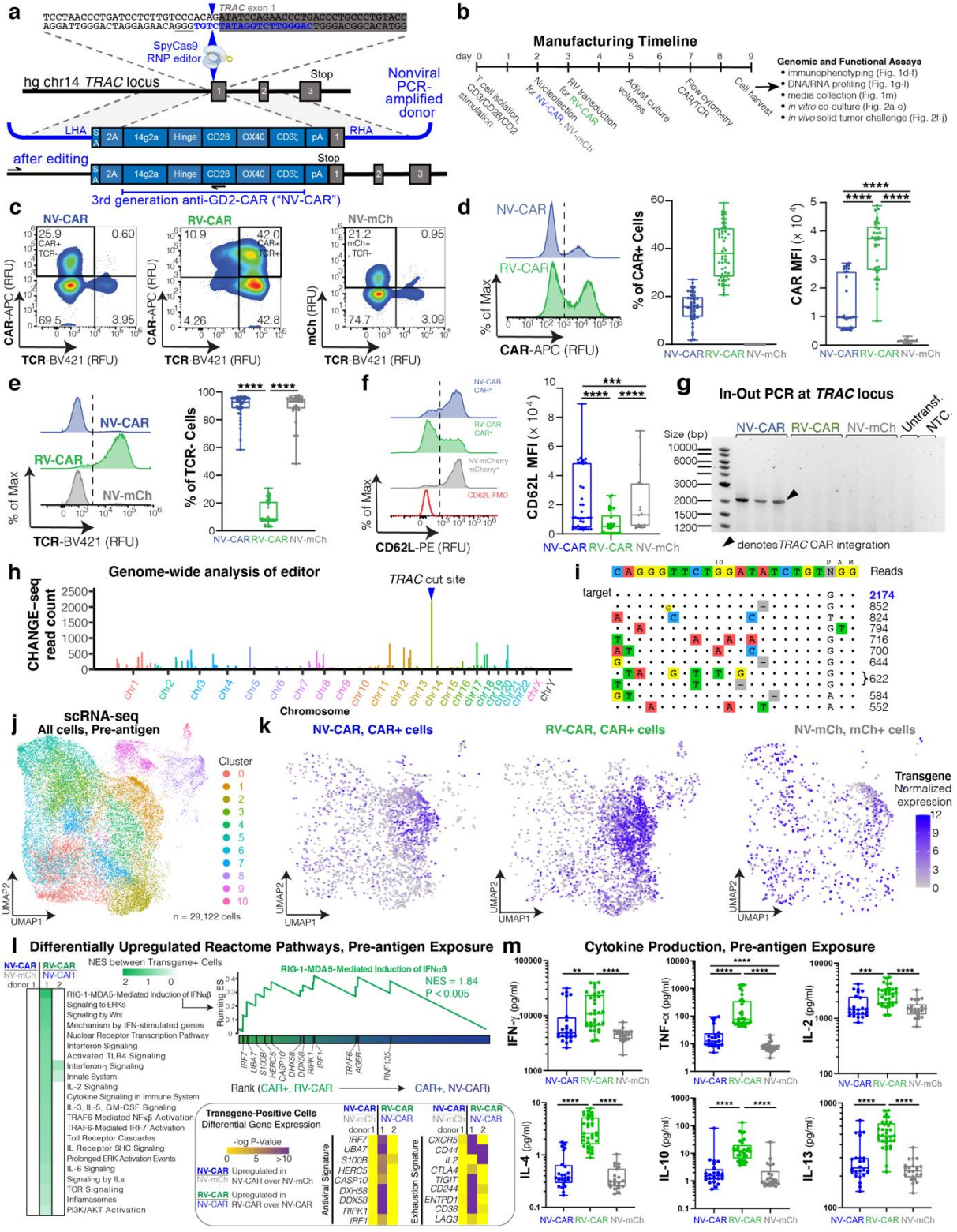
a
TRAC exon 1
TCCTAACCCTGATCCTCTTGTCCCACAGATATCCAGAACCCTGACCCTGCCGTGTACC
AGGATTGGGACTAGGAGAACAGGGTGTCTATAGGTCTTGGGACTGGGACGGCACATGG
SpyCas9 RNP editor
hg chr14 TRAC locus
Stop
Nonviral PCR-amplified donor
LHA
SA
2A
14g2a
Hinge
CD28
OX40
CD3ζ
pA
RHA
after editing
3rd generation anti-GD2-CAR ("NV-CAR")
b
Manufacturing Timeline
day 0 1 2 3 4 5 6 7 8 9
T cell isolation, CD3/CD28/CD2 stimulation
Nucleofection for NV-CAR, NV-mCh
RV transduction for RV-CAR
Adjust culture volumes
Flow cytometry CAR/TCR
Cell harvest
Genomic and Functional Assays
• immunophenotyping (Fig. 1d-f)
• DNA/RNA profiling (Fig. 1g-l)
• media collection (Fig. 1m)
• in vitro co-culture (Fig. 2a-e)
• in vivo solid tumor challenge (Fig. 2f-j)
c
NV-CAR
RV-CAR
NV-mCh
CAR-APC (RFU)
mCh (RFU)
TCR-BV421 (RFU)
d
NV-CAR
RV-CAR
% of Max
CAR-APC (RFU)
% of CAR+ Cells
CAR MFI (x 10⁴)
NV-CAR RV-CAR NV-mCh
e
% of TCR- Cells
f
CD62L MFI (x 10⁴)
CD62L-PE (RFU)
g
In-Out PCR at TRAC locus
Size (bp)
Untransf.
NTC.
denotes TRAC CAR integration
h
Genome-wide analysis of editor
TRAC cut site
CHANGE-seq read count
Chromosome
i
Reads
target
2174
852
824
794
716
700
644
622
584
552
j
scRNA-seq
All cells, Pre-antigen
Cluster
n = 29,122 cells
UMAP1
UMAP2
k
NV-CAR, CAR+ cells
RV-CAR, CAR+ cells
NV-mCh, mCh+ cells
Transgene Normalized expression
l
Differentially Upregulated Reactome Pathways, Pre-antigen Exposure
NES between Transgene+ Cells
RIG-1-MDA5-Mediated Induction of IFNαβ
NES = 1.84
P < 0.005
Running ES
Rank (CAR+, RV-CAR → CAR+, NV-CAR)
Signaling to ERKs
Signaling by Wnt
Mechanism by IFN-stimulated genes
Nuclear Receptor Transcription Pathway
Interferon Signaling
Activated TLR4 Signaling
Interferon-γ Signaling
Innate System
IL-2 Signaling
Cytokine Signaling in Immune System
IL-3, IL-5, GM-CSF Signaling
TRAF6-Mediated NFκβ Activation
TRAF6-Mediated IRF7 Activation
Toll Receptor Cascades
IL Receptor SHC Signaling
Prolonged ERK Activation Events
IL-6 Signaling
Signaling by ILs
TCR Signaling
Inflamasomes
PI3K/AKT Activation
Transgene-Positive Cells Differential Gene Expression
-log P-Value
NV-CAR Upregulated in NV-CAR over NV-mCh
RV-CAR Upregulated in RV-CAR over NV-CAR
Antiviral Signature
Exhaustion Signature
m
Cytokine Production, Pre-antigen Exposure
IFN-γ (pg/ml)
TNF-α (pg/ml)
IL-2 (pg/ml)
IL-4 (pg/ml)
IL-10 (pg/ml)
IL-13 (pg/ml)

Figure 2.1

Nonviral CRISPR-CAR T cells are efficiently manufactured in 9 days and exhibit decreased detrimental signaling and exhaustion before encountering their target antigen. a, Schematic showing the CAR genetic construct and nonviral strategy to insert the CAR into the first exon of the human *TRAC* locus. The seed sequence of the gRNA is in blue and the protospacer adjacent motif (PAM) for SpyCas9 is underlined. LHA: left homology arm, SA: splice acceptor, 2A: self-cleaving peptide, pA: rabbit ß-globin polyA terminator. **b,** Summary of manufacturing schedule and analyses for all cell products. RV-CAR, donor-matched CAR T cell product generated by retroviral transduction with the same third generation anti-GD2 CAR shown in a; NV-mCh, donor-matched control T cell product manufactured nonvirally as in **a** but with an mCherry fluorescent protein instead of the CAR. **c,** Representative density flow cytometry plots for transgene and TCR surface protein levels on the manufactured cell products. Y-axis shows CAR or mCherry transgene levels and X-axis shows TCR levels on day 7 post isolation (day 5 post-electroporation for NV-CAR and NV-mCh, and day 4 post viral transfection for control RV-CAR). Boxes show populations selected for downstream analysis in d-f. **d,** Histograms show CAR expression for the three test groups. Boxplots show the percentage of CAR positive cells in each sample, and mean fluorescence intensity (MFI) values for the CAR expression levels, respectively. NV-CAR (blue) N=31; RV-CAR (green) N=39; NV-mCh (gray) N=27. **e,** Histograms show TCR expression on the three test groups. Boxplots show the percentage of CAR positive cells in each sample. NV-CAR (blue) N=31; RV-CAR (green) N=39; NV-mCh (gray) N=27. **f,** Histograms show CD62L expression for the three test groups. Boxplots show mean fluorescence intensity (MFI) for CD62L expression. NV-CAR (blue) N=31; RV-CAR (green) N=39; NV-mCh (gray) N=27. Replicates from 97 samples across 4 separate donors**. g,** In-out PCR indicates proper on-target genomic integration of the CAR transgene in NV-CAR cells. Primer locations are shown in a by arrows upstream of the LHA and within the CD28 sequence of the CAR. Untransf., untransfected donor-matched T cells; NTC = non-template control. **h,** Manhattan plot of CHANGE-seq-detected on- and off-target sites organized by chromosomal position with bar heights representing CHANGE-seq read count. The on-target site is indicated with the blue arrow. **i,** Visualization of sites detected by CHANGE-seq. The intended target sequence is shown in the top line. Cleaved sites (on- and off-target) are shown below and are ordered top to bottom by CHANGE-seq read count, with mismatches to the intended target sequence indicated by colored nucleotides. Insertions are shown in smaller lettering between genomic positions, deletions are shown by (-). Note that output is truncated to top sites, with a full listing in **Supplementary Table 2.1**. **j,** UMAP projection of single cell RNA-seq data from 11 samples of manufactured cell products, both pre- and post-antigen exposure; 29,122 single cells from NV-CAR, RV-CAR, and NV-mCh T cell products at the end of manufacture (prior to antigen exposure) are shown here. Full UMAP for all 11 samples together is shown in **Extended Data Fig. 2.2a**. **k,** UMAP projections as in j showing only cells for which transgene-positive cells were detected. Transgene-positive cells cluster similarly for both NV-CAR and RV-CAR T cells, but not NV-mCh T cells. **l,** Enrichment of Reactome pathway gene signatures (rows) in the transgene-positive cells from donors 1 and 2. NES, Normalized

Enrichment Score. At right, representative gene set enrichment analysis (GSEA) plot of a signature within CAR-positive T cells from a RV-CAR sample (green), where genes differentially expressed in CAR-positive RV-CAR cells versus CAR-positive NV-CAR cells from donor 1 are listed and ranked. FDR < 0.001 for each comparison, by gene-set permutation test. Below the GSEA plot is a heatmap representing transcripts with significant differential expression. Rows represent adjusted p-value using Bonferroni correction for all features in the dataset. **m,** Cytokine production from conditioned media taken from T cell products at the end of manufacturing (pre-antigen exposure). Values are pooled from all 4 donors. NV-CAR (blue) N=24; RV-CAR (green) N=33; NV-mCherry (gray) N=22. * indicates p<=0.05; ** indicates p<=0.01; *** indicates p<=0.001; **** indicates p<=0.0001.

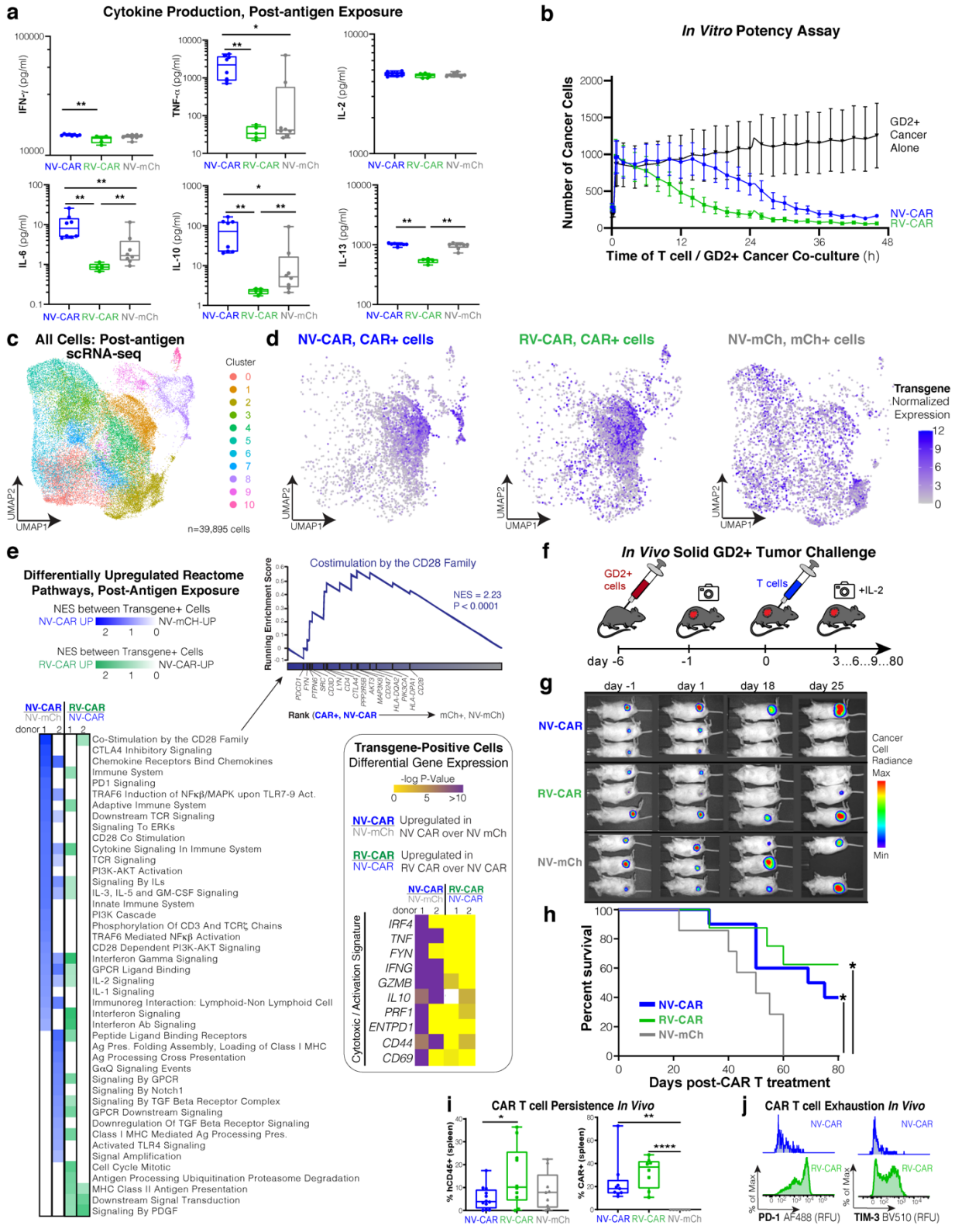
a
Cytokine Production, Post-antigen Exposure
IFN-γ (pg/ml)
TNF-α (pg/ml)
IL-2 (pg/ml)
IL-6 (pg/ml)
IL-10 (pg/ml)
IL-13 (pg/ml)
NV-CAR RV-CAR NV-mCh
b
In Vitro Potency Assay
Number of Cancer Cells
GD2+ Cancer Alone
NV-CAR
RV-CAR
Time of T cell / GD2+ Cancer Co-culture (h)
c
All Cells: Post-antigen scRNA-seq
Cluster
n=39,895 cells
d
NV-CAR, CAR+ cells
RV-CAR, CAR+ cells
NV-mCh, mCh+ cells
Transgene Normalized Expression
e
Differentially Upregulated Reactome Pathways, Post-Antigen Exposure
NES between Transgene+ Cells
NV-CAR UP
NV-mCH-UP
NES between Transgene+ Cells
RV-CAR UP
NV-CAR-UP
Costimulation by the CD28 Family
NES = 2.23
P < 0.0001
Running Enrichment Score
Rank (CAR+, NV-CAR → mCh+, NV-mCh)
donor 1 2 1 2
Co-Stimulation by the CD28 Family
CTLA4 Inhibitory Signaling
Chemokine Receptors Bind Chemokines
Immune System
PD1 Signaling
TRAF6 Induction of NFκβ/MAPK upon TLR7-9 Act.
Adaptive Immune System
Downstream TCR Signaling
Signaling To ERKs
CD28 Co Stimulation
Cytokine Signaling In Immune System
TCR Signaling
PI3K-AKT Activation
Signaling By ILs
IL-3, IL-5 and GM-CSF Signaling
Innate Immune System
PI3K Cascade
Phosphorylation Of CD3 And TCRζ Chains
TRAF6 Mediated NFκβ Activation
CD28 Dependent PI3K-AKT Signaling
Interferon Gamma Signaling
GPCR Ligand Binding
IL-2 Signaling
IL-1 Signaling
Immunoreg Interaction: Lymphoid-Non Lymphoid Cell
Interferon Signaling
Interferon Ab Signaling
Peptide Ligand Binding Receptors
Ag Pres. Folding Assembly, Loading of Class I MHC
Ag Processing Cross Presentation
GαQ Signaling Events
Signaling By GPCR
Signaling By Notch1
Signaling By TGF Beta Receptor Complex
GPCR Downstream Signaling
Downregulation Of TGF Beta Receptor Signaling
Class I MHC Mediated Ag Processing Pres.
Activated TLR4 Signaling
Signal Amplification
Cell Cycle Mitotic
Antigen Processing Ubiquitination Proteasome Degradation
MHC Class II Antigen Presentation
Downstream Signal Transduction
Signaling By PDGF
Transgene-Positive Cells
Differential Gene Expression
-log P-Value
NV-CAR Upregulated in NV-mCh NV CAR over NV mCh
RV-CAR Upregulated in NV-CAR RV CAR over NV CAR
Cytotoxic / Activation Signature
IRF4
TNF
FYN
IFNG
GZMB
IL10
PRF1
ENTPD1
CD44
CD69
f
In Vivo Solid GD2+ Tumor Challenge
GD2+ cells
T cells
+IL-2
day -6
-1
0
3...6...9...80
g
day -1
day 1
day 18
day 25
NV-CAR
RV-CAR
NV-mCh
Cancer Cell Radiance
Max
Min
h
Percent survival
NV-CAR
RV-CAR
NV-mCh
Days post-CAR T treatment
i
CAR T cell Persistence In Vivo
% hCD45+ (spleen)
% CAR+ (spleen)
NV-CAR RV-CAR NV-mCh
j
CAR T cell Exhaustion In Vivo
NV-CAR
RV-CAR
% of Max
PD-1 AF488 (RFU)
TIM-3 BV510 (RFU)

Figure 2.2

Nonviral CRISPR-CAR T cells exhibit a robust cytotoxic response to target antigen-positive tumor cells *in vitro* and induce tumor regression *in vivo* with a reduced exhaustion phenotype. **a,** Cytokine production in conditioned media after a 24 hour co-culture of manufactured T cell products with the target GD2-antigen on CHLA20 neuroblastoma cells. Values are pooled from 2 donors. NV-CAR (blue) N=8; RV-CAR (green) N=5; NV-mCh (gray) N=8. **b,** IncuCyte *in vitro* assay of T cell potency, averaged across donors. AnnexinV was added as a marker of cell death; y-axis shows GFP-positive cancer cells in each well of a 96-well plate. The ratio of T cells to cancer cells is 5:1. The consistent decrease in CHLA20 cells after 15 hours indicates high potency of both NV-CAR and RV-CAR T cells. NV-CAR (blue) N=12; RV-CAR (green) N=12; CHLA20 neuroblastoma alone (black) N=9. **c,** UMAP projection of single cell RNA-seq data from cells across 11 samples, both pre- and post-antigen exposure; 39,895 single cells from NV-CAR, RV-CAR, and NV-mCh T cell products after 24 h of GD2-antigen exposure are shown here. **d,** UMAP projections as in **c** showing only cells for which transgene was detected. Transgene-positive cells cluster similarly for both NV-CAR and RV-CAR T cells, but not for NV-mCh T cells. **e,** Enrichment of Reactome pathway gene signatures (rows) in the transgene-positive cells from donors 1 and 2 after co-culture with GD2-positive CHLA20 cancer cells. NES, Normalized Enrichment Score. At right, representative GSEA showing differential cytotoxicity signature of NV-CAR/NV-mCh paired samples for two donors (blue), and NV-CAR/RV-CAR samples (green). NV-CAR T cells show significant upregulation of cytotoxicity markers relative to NV-mCh control cells after GD2 antigen exposure, while NV-CAR and RV-CAR T cells show no significant difference in activation signature upon GD2 antigen stimulation. FDR < 0.001 for each comparison, by gene-set permutation test. Bottom GSEA plot is a heatmap representing transcripts with significant differential expression. Rows represent adjusted p-value using Bonferroni correction for all features in the dataset. **f,** Schematic of the *in vivo* mouse dosing strategy using NSG mice harboring GD2-positive CHLA20 neuroblastoma tumors. **g,** Representative IVIS images of NSG mice with CHLA20 tumors that were treated with either 10 million NV-CAR, RV-CAR, or NV-mCh T cells. **h,** Kaplan-Meyer survival curve for mice. NV-CAR (blue) N=10; RV-CAR (green) N=8; NV-mCh (gray) N=7. **i,** Box plots on the amount of human T cells present in mouse spleens, as measured by the presence of human CD45 using flow cytometry, and the percentage of those cells in the spleen that were CAR-positive. **j,** Histograms showing the expression levels of PD-1 and TIM-3 on the human CD45+ cells in the mouse spleens. *indicates p<=0.05; ** indicates p<=0.01; *** indicates p<=0.001; **** indicates p<=0.0001.

CHAPTER 3: *In Vitro* Microwell Cytotoxicity Assays to Predict CAR T Cell Therapeutic Response

Portions of the work in this chapter were adapted from:

Predicting Outcomes in CAR T Cell Therapies for Cancer using *In Vitro* Potency Assays.

Nicole J. Piscopo, Daniel Aguilar-Hidalgo, Tiam Heydari, Yasmin Alvarez-Garcia, Katherine P. Mueller, Matthew H. Forsberg, Christian M. Capitini, David Beebe, Peter Zandstra, Krishanu Saha

Article in Preparation.

Abstract

The manufacture of chimeric antigen receptor (CAR) T cell therapy is expanding along both autologous and allogenic workflows. In both workflows, manufacturers will need to define a set of critical quality attributes (CQA) that are measurable prior to infusion of the CAR product into patients. Current quality assurance and quality control (QA/QC) includes flow cytometry for expression of the CAR on the surface of the T cells, but CAR expression alone has not been informative in predicting remission in patients. In this work, we used flow cytometry, cytokine production, *in vitro* cytotoxicity, and RNA sequencing measurements to aid in the prediction of tumor response to CAR T cell therapy in a xenogeneic solid tumor model. We identify a combination of cytokine production pre-antigen exposure, RNAseq, and CAR surface expression, which when used together can be highly predictive (81.8% of variance in outcomes explained). Insights from these results have the potential to inform clinical CAR T manufacturing workflows by defining pre-infusion measurements that aid in predicting the efficacy of CAR T products post-infusion for inducing remissions of solid tumors.

Introduction

Chimeric antigen receptor (CAR) T cells are genetically engineered T cells that have been designed to express the scFv fragment of an antibody with co-stimulatory and cytotoxicity signaling molecules to target and eliminate tumor cells in a cell surface antigen-specific manner. Traditionally, CAR T cells are generated by collecting peripheral blood from a cancer patient using leukapheresis, isolating their T cells, virally transducing the cells to express the CAR, expanding the T cells and then delivering them back to the patient after lymphodepletion [172]. CAR T cell therapy has seen high levels of success in B cell malignancies, with as many as 80% of patients

undergoing complete remission using anti-CD19 CARs which targets the malignant and healthy B cells [23], [173].

Three autologous CAR T cell products have been FDA approved for hematological malignancies, but outside of a few patient outliers, CAR T cells have not yet been consistently effective in treating solid tumors. The inherent variation in cellular product manufactured from an autologous source have prevented us from gaining significant insight as to the key parameters that might enable success of CAR T cells to the treatment of solid tumors [5]. In autologous workflows, the starting cellular composition will vary from patient to patient based on prior chemotherapy as well as the site of random insertion of the CAR due to viral insertion and copy number which can all impact the quality of the end product delivered back to the patient. Such variations can influence the rate of proliferation, cytotoxicity, and exhaustion of CAR T cells after delivery [174].

While the approved CAR T products are autologous, there are multiple advantages to providing an allogeneic CAR T cell therapy product that could allow for improvements for tumor treatment such as knocking out the *TRAC*, *PD-1*, *B2M*, or *CD52* loci among others [175]. Engineering an "off-the-shelf" allogenic product opens the door for some of the many new approaches that are being published to make CAR T cells more cytotoxic and better prone to form memory without adding to the amount of manufacturing lead time that patients would have to wait to receive their therapy. To maximize the potential of an allogenic CAR T cell manufacture workflow, manufacturers will need minimize interventions needed on a patient-by-patient basis (if any) and delivering the product as quickly as possible without sacrificing efficiency. The primary QA/QC for CAR T potency is to run flow cytometry to verify the presence the CAR protein on the surface of the cells and verify cytokine production upon exposure to antigen, but this assay is not sufficient to predict if the cell product will lead to cancer regression[176]–[180]. For solid tumors,

emerging evidence shows that CAR T cell expansion and persistence *in vivo* after infusion is the best indicator if a solid tumor will respond to treatment [151]. A setback is that if the CAR T cells do not expand well *in vivo*, there are no available means to intervene other than re-infusing the patient with more CAR T cells, which has not yet been effective.

Microwells have been increasingly studied to assay various cellular functions such as NK cell associated cytotoxicity [181], [182], nanoparticle-induced cell death [183], and trogocytosis and cooperative killing [184]. Many of these assays have moved single cell scale platforms to observe serial killing and additional clonal behaviors [185]–[187]. The one-on-one interaction of CAR T cells and tumors may better recapitulate the immune synapse against hematological cancers on a cell-by-cell basis in blood and bone marrow, but this platform does not recreate the complex, 3-dimensional microenvironment of solid tumors where CAR T cells infiltrate a combination of tumor cells, immune cells, fibroblasts and vascular endothelium as well as secreted molecules from these cells. While technologies exist that generate 3-dimensional (3D) models to study CAR T cell infiltration into tumors and cytotoxicity, the need for higher powered microscopes are required and may not be as readily available for a clinical manufacturing GMP workflow. In recent years. the IncuCyte Live Cell Analysis System has emerged as a technique that can be adapted to most cell culture incubators to perform real-time, long term imaging to elucidate cell to cell co-culture growth as well as activation, function, and differentiation of T cells [188],[189]. More recently, 2-dimensional (2D) impedance based methods such as the xCELLigence System have become emerged to explore the potency of CAR T cells in a glioma model [125], [190], [191].

In this report, we describe a 2D microwell platform that simplifies preparation, imaging, and analysis of CAR T cells for potency. The measurements taken from the microwell system allow for the derivation of a cytotoxicity rate, β, for the assayed T cells. This cytotoxicity constant

is then combined with other measurements taken prior to infusion of the CAR T product and input into a partial least square regression (PLSR) model to determine the rate of growth of a GD2+ neuroblastoma tumor in a murine xenograft. This work builds a novel predictive mathematical model, as well as provide information about which *in vitro* measurements can best predict the *in vivo* response of the CAR T cells.

Results

Development of High Throughput Microwell Coculture Pipeline

Polydimethylsiloxane (PDMS) microwells were constructed using photolithography (**Figure 3.1a)** both alone and with cocultures of GD2+ cancer cells and engineered T cells (**Figure 3.1b).** The cancer cells are seeded onto a gelatin coating for 24 hours on their own to adhere to the microwells (**Figure 3.1c)** allowing for one microwell to be imaged every few hours (**Figure 3.1d**). The GD2+ M21 human melanoma line was edited using CRISPR Cas9 to constitutively express H2B-mCherry and seeded into microwells. T cells were stained with Hoechst to label all cell nuclei and added to the M21 cells. The microwells were then treated with CellEvent Caspase-3/7 to monitor cell apoptosis (**Figure 3.1e)** [183].

Workflow for the CellProfiler imaging pipeline can be seen in **Figure 3.1f**. In short, H2B-mCherry (λ_{EX} 587nm, λ_{EM} 610nm) objects are identified as cells based on pixel intensity and a specified diameter. These objects are then measured and their eccentricity is used to help filter out any background fluorescence that may be incorrectly identified as a cell. A mask is then made of the mCherry image and applied to the images taken in the GFP (λ_{EX} 488nm, λ_{EM} 509nm) channel. This mask helps to only allow for the identification of apoptotic M21 cells in locations where H2B-mCherry positive cells were present, and the specified diameter does not allow for the identification of smaller cells such as dead T cells.

Deriving Mathematical Immune Cell Killing Constants from In Vitro Coculture Systems

Previous coculture platforms have been used to measure the interactions between individual T cells and cancer cells to help to define a systems of ordinary differential equations (ODEs) to model CAR T cell therapy [192], [193]. To establish our own model, both non-viral (NV)-CAR and retroviral (RV)-CAR T cells that were engineered from T cells from four healthy donors (as previously described in Chapter 2) were cocultured with a H2B-mCherry+ human GD2+ melanoma line M21 on microwells. We also utilized a known cytotoxic natural killer cell line (NK92) as a positive control. The number of CellEvent Caspase-3/7 positive cells that overlapped with the H2B-mCherry+ M21 cells was subtracted from the number of H2B-mCherry+ M21 cells to determine the number of living M21 left in each microwell every 4 hours over the 48-hour period. The results from Donor 1 cocultures, shown as the number of living M21 per microwell, can be seen in **Figure 3.2a.** On microwells where only cancer cells were seeded and no cytotoxic immune cells were added, the cancer cell number either remained constant or grew slightly over the 48-hour period (**Fig. 3.2a**, black). In the NV-CAR T, RV-CAR T, and NK92 cell coculture microwells, (**Fig. 3.2a**, blue, green, orange, respectively), most microwells saw a decrease in the number of M21 cells present.

To determine the killing constant, β, for each population of cytotoxic immune cells, a differential equation had to be established. **Equation 1** shows the differential equation to model the presence of living cancer cells in the microwells. **Equation 2** is the solution of **Equation 1**, which shows an exponential response in the number of living cancer cells, C_a, in each well at a given time, t, as a function of the number of cancer cells at t=0, C_0, with respect to the number of immune cells present at t=0, I, and the respective immune cells killing constant, β.

(1) $$\frac{dC_a}{dt} = -(\beta * I)C_a$$

(2) $$C_a = C_0 e^{(-\beta * I)t}$$

To ensure that the experimentally measured number of living cancer cells could be modeled with this equation, we normalized the number of living cancer cells in each well to the number of cancer cells that were present at the initial timepoint. The normalized equation for the number of cancer cells at t=0 can be seen in **Equation 3**:

(3) $$\frac{C_a}{C_0} = \frac{C_0 e^{(-\beta * I)t}}{C_0} = e^{(-\beta * I)t}$$

To determine the cytotoxic constant, β, for the various immune cell populations in each microwell, we normalized the number of M21 cells present at each timepoint in each microwell and applied the exponential fit function to the cells (**Fig 3.2b).** This fit provided values for β*I. We then plotted the number of immune cells at time zero on the x-axis and the corresponding β*I values on the y-axis. A line was fit to these points, where the slope of this line provides the average β value for each population of immune cells across the microwells for those conditions **(Fig. 3.2c,d)**.

From the analysis above, we can establish that the survival dynamics of cancer cells follows an exponential function. We can see this by making a transformation to Equation 3. In this case, we applied a power of 1/(β*I), as is shown in **Equation 4**:

(4) $$\left(\frac{C_a}{C_0}\right)^{\frac{1}{\beta * I}} = \left(e^{(-\beta * I)t}\right)^{\frac{1}{\beta * I}} = e^{-t}$$

Equation 4 provides a universal scaling law for the growth of cancer cells, which is parameter free. In **Figure 3.2e**, we show the transformed data (dots) together with the scaling law.

The agreement between our theory and the data suggests that the cancer cells adapt their growth dynamics to the presence of different concentrations of immune cells such that they follow an exponential pattern.

Figure 3.2b shows the curves that were fit to the number of viable M21 cells per microwell for each of the four conditions. The step by step process described here is for the manipulation of the microwell data (**Figure B-1**) and IncuCyte data (**Figure B-2)**. The plots where the number of immune cells present at time zero are on the x-axis and the individual β values for each fit exponential equation are on the y-axis can be seen in **Figures 3.2c** and **3.2d** for the NV-CAR and RV-CAR microwells, respectively. These β values were calculated for all NV-CAR and RV-CAR samples for all 4 donors and can be seen in **Figure 3.2f**. Across all four donors, NV-CAR has a higher calculated β value in comparison to the RV-CAR (n=65, per donor). For 3 of the 4 donors, the NV-CAR T cells also have a more compact spread, as is shown in **Figure 3.2g** by having a smaller standard deviation. Positive β values indicate a decrease in the number of M21 cells with time, whereas microwells with a negative β did not see a decrease in M21 cells. **Figure 3.2h** shows the associated r-squared values for the calculated β which are generally higher in wells that had a more drastic change in the growth or decay in number of M21 cells.

Predicting In Vivo Response with Partial Least Squares Regression

We decided to use partial least squares regression (PLSR) to allow for the incorporation of various types of data to predict one dependent outcome, which has been done before in other areas of cell-based research such as cellular reprogramming [194]. JMP was used to run PLSR on the *in vitro* data taken prior to CAR T infusion. This data includes cytokine production values, both pre- and post-antigen exposure, as well as the percent of each test population of cells expressing specific genes as was measured by single cell RNA sequencing, both pre- and post-antigen exposure. The

percent of cells expressing the CAR and TCR on the cell surface is also included, as was measured by flow cytometry. The final piece of information provided to aid in the prediction of *in vivo* tumor response is the flux measurement of the tumor, taken with IVIS, on the day of CAR T infusion into the mice.

To determine the appropriate response variable PLSR modeling, both the cytokine production data and RNAseq data, were analyzed separate from one another to see if they differed in the optimal end variable predictor. Potential end variables assayed include final tumor flux value, linear tumor growth rate (calculated by final tumor flux measurement minus initial tumor flux divided by number of days lived), exponential tumor growth rate (calculated by fitting the initial and final tumor flux measurements to the exponential function), and number of days lived. In both the cytokine production and RNAseq PLSR models, exponential tumor growth rate had a higher percent of variance explained and a lower root mean PRESS value than the other potential end point variables (**Figure 3.3a**). As a result, all future PLSR models described here used exponential tumor growth rate as the predicted variable.

Pre-Antigen Exposure Cytokine Production Measurements Aid in Prediction of In Vivo Response

When paired with the initial tumor flux value and the percent of CAR+ and TCR- cells as measured by flow cytometry, a combination of pre- and post-antigen exposure cytokine production values allowed for 47.84% of the variance in the exponential tumor growth with a root mean PRESS of 0.84913 (**Table 3.1**).

Cytokine Production	% Var. Explained	Root Mean PRESS
Pre- and Post Antigen Exposure	47.84	0.84913
Pre-Antigen Exposure	51.89%	0.79167
Post-Antigen Exposure	46.16%	0.91019

Table 3.1. PLSR outputs for cytokine production data sets from Donors 3 and 4.

This calculation was run only on data from donors 3 and 4 because we did not record post-antigen exposure cytokine production from donors 1 and 2. When only the post-antigen exposure cytokine production values were input, percent of variance explained dropped slightly to 46.16% and the root mean PRESS increased slightly to 0.91019. When pre-antigen exposure cytokine production values were switched to replace the post-antigen exposure values, the percent variance explained increased slightly to 51.89% and the root mean PRESS dropped to 0.79167. This suggests that the pre-antigen exposure cytokine production values may be more indicative of *in vivo* response than the post-antigen exposure data. When the pre-antigen cytokine production measurements from all 4 donors was used to predict *in vivo* exponential tumor growth rate, the percent variance explained increased to 65.77% and the root mean PRESS dropped further to 0.74011.

Impact of Single Cell Transcriptional Measurements on In Vivo Response

The values put into the single cell RNA sequencing model were the percent of cells in the population that expressed each given gene. Data was collected both pre and post-antigen exposure, and in bulk (for all cells that were sequenced) as well as in the transgene positive only fraction (cells expressing the CAR or the mCherry gene). **Table 3.2** shows the percent variance explained, root mean PRESS, and number of factors when PLSR models were fit to each of the sub-groups of RNA seq values. While there was little change in the percent variance explained and the root

mean PRESS, the factors required to reach this level of explanation is lower in the transgene only fraction of the cells.

	Whole T Cell Population			Transgene Positive Cells Only		
	% Var. Explained	Root Mean PRESS	Factors	% Var. Explained	Root Mean PRESS	Factors
Pre-Antigen Exposure	77.65%	0.65853	4	77.42%	0.63277	3
Post-Antigen Exposure	77.65%	0.65335	4	77.32%	0.64014	2

Table 3.2. PLSR outputs for RNAseq data sets.

The loadings plots for the variables in the transgene positive only samples can be seen in **Figure 3.3b** for the pre-antigen exposure values and **Figure 3.3c** for the post-antigen exposure values. For the pre-antigen exposure model, factor 1 had high loadings for genes relating to T cell activation such as *CD69, CD27, IL-2,* and *PRF1*. Factor 2 was split between activation markers (*ICOS, TNF-α, IFN-γ*) as well as exhaustion markers *(CTLA4, PD-1, BTLA, KIR3DXL1*), whereas factor 3 was mostly exhaustion markers (*CTLA4, TIM-3, LAG3*) but also included *GZMB*. In the post-antigen exposure model, both factor 1 and factor 2 had a mixture of high loadings for activation and memory markers, (*TNF-α, IFN-γ, TNFRSF4, TNFRSF9, PD-1, CTLA4, BTLA* for factor 1 and *ICOS, CD27, IL-2, TIM-3, LAG-3, GZMB, PRF1* for factor 2).

Impact of In Vitro Cytotoxicity Measurements on In Vivo Response

Building upon the pre-antigen exposure cytokine production model, we next added in the calculated cytotoxicity constant, β, to evaluate whether it could increase the percent variance explained. **Figure 3.4a, black** shows the change in the amount of variance explained for the cytokine data, using on the pre-antigen exposure values, when adding in either the β calculated from the microwells or the β calculated from the IncuCyte assay. When the β for the microwell is added to the model, the percent variance explained increased from 65.77% to 70.1% and the root

mean PRESS dropped to 0.78262. Furthermore, the loading for the microwell β was among the highest in factor 1 for that model. When the Incucyte β value was substituted in place of the microwell β, the percent variance explained dropped down from the microwell model to 67.99% (which is still higher than the 65.77% without any β value) while the root mean PRESS remained similar, at 0.77161. The Incucyte β had a similar loading as was seen with the microwell β.

In the pre-antigen exposure and transgene positive RNAseq model, when only looking at the NV-CAR and RV-CAR conditions the percent variance explained was 68.15% (**Figure 3.4a, gray**). When adding in the microwell β, the new percent variance explained is similar at 68.47%. With the addition of the Incucyte β, the percent variance explained increases to 70.93%. In both models, the β have similar loadings in factor 1.

NV-CAR T cells are more predictive than RV-CAR T cells

To see how well all of the data gathered here could be used to predict *in vivo* efficacy, we combined the flow data and flux measurements with the pre-antigen exposure cytokine production data and the pre-antigen exposure RNAseq data sets. When analyzing data for both NV-CAR and RV-CAR at once and with no β, the percent variance explained was 68.60%. In **Figure 3.4b, blue and green** striped bars show that adding either the microwell β or the Incucyte β did little to change the percent variance explained.

When using the combined the pre-antigen exposure cytokine production data with the pre-antigen exposure RNAseq data sets to look at the NV-CAR samples alone, we saw that without β, the percent variance explained is 81.87% (**Figure 3.4b, blue bars**). Adding the microwell β resulted in the same percent explained variance but adding in the IncuCyte β instead resulted in a slight decrease in explained variance to 76.89%. When applying the same data sets to only the RV-

CAR samples, without β, the percent variance explained was 51.77% (**Figure 3.4b, green bars)**. Adding either the microwell β or the IncuCyte β increased the variance explained slightly to 54.55%. Therefore, using pre-antigen exposure cytokine production data, pre-antigen exposure RNAseq data sets, and an *in vitro* calculated β, the *in vivo* outcome for the NV-CAR T cell populations were more predictable than the RV-CAR T cells.

Looking at the loadings for the models incorporating the flow data, flux measurements, pre-antigen exposure cytokine production data, and the pre-antigen exposure RNAseq data sets, we can see how the models vary for each of the various cell populations. **Figure 3.4c** shows the loadings for the model combining NV-CAR and RV-CAR data. In this model, the cytokine data loadings have a higher magnitude across the board, whereas the RNA seq data varies in its loading values. The model for the NV-CAR samples alone have inverse loadings in the cytokine data (**Fig. 3.4d**) and predominantly positive loading values for the RNA seq data. The RV-CAR only also had mostly positive values for the RNA seq data but had varied loadings on the cytokine data (**Fig. 3.4e**). The variations in the loadings of these models suggests that there may not be a universal model to predict tumor growth *in vivo*. Between the NV-CAR only and the RV-CAR only models, genes that consistently had high loadings were *CD2, CD28, IL2RA, CD69, ICOS TNFRSF9, IL2, TNF-α, IFN-γ, CTLA4, BTLA, TIM-3, LAG-3, KIR3DX1, FOXP3,* and the *CAR*. Interestingly, CD8A and B had loadings with high, negative magnitudes, as did *CCR7*.

Discussion

The success seen with autologous CAR T-cell therapy for hematological malignancies has not yet translated to solid tumors, and allogenic CAR T cell products may allow scientists the ability to engineer more potent and predictable batches of CAR T cells. From a scientific standpoint,

allogeneic CAR T therapies remove the pressure to manufacture a CAR T product in as short a time as possible since theoretically the patient would receive these cells “off-the-shelf” and not actively have to endure toxic bridging chemotherapy while waiting for their cells to be manufactured and shipped to them, as is the case with autologous CAR T workflows. Patients will also not have to undergo leukapheresis and the starting population for their cell therapy will come from healthy a donor who has T cells that have not already been subject to multiple rounds of cancer treatment. Furthermore, the potential to treat multiple patients with multiple doses is possible and not limited by the cell dose of a leukapheresis.

In terms of being able to predict *in vivo* response from purely pre-infusion measurements, the field of CAR T cell therapy lacks reliable potency assays and predictive mathematical models to inform prescribing clinicians. Using a 2D microwell cytotoxicity assay, we were able to develop a PLSR mathematical model that demonstrates that cytokine production values rom CAR T cells pre-antigen exposure offer more percent variance explained than post-antigen exposure. This is an interesting finding because of increasing evidence of tonic signaling observed by out group and others within RV-CAR cell products even prior to antigen exposure, and this may be part of what is being detected in the PLSR models [82],[128]. Cytokine production may be more predictive than RNA sequencing data, which is beneficial because single cell RNA sequencing (scRNAseq) is costly and takes time for comprehensive bioinformatic analysis, making it unlikely to be clinically useful in real time management of patients. Additionally, most analysis of these large data sets focuses on genes or pathways that we already know play a role in the cell types that we are assaying. However, advances in scRNAseq analysis tools and supercomputing may impact the quality and predictive potential of this assay moving forward.

An *in vitro* cytotoxicity measurement can inform the predictability of tumor growth post CAR T infusion. Depending on the assays used, 2D microwell cocultures or live cell imaging such as with Incucyte could be more effective at adding to the predictive capabilities of these models. In recent years, ODEs have been developed to model CAR T Cell treatment in patients with preconditioning, as well as in the presence of monoclonal antibody therapy or corticosteroids [176], [195]. However, many of these models are based on data acquired from patients, post-treatment [178]. While this work is informative, there is still a need to make pre-infusion measurements to better predict the potency of autologous or allogeneic CAR T cell products. In order to increase the amount of variance that the microwell system can contribute, a higher ratio of effector to target cells should be used to add augment killing in all wells as it is likely that in wells with fewer cells, there may be insufficient numbers of CAR positive T cells present to detect an effect. This may be why for some of the donors, there was a tighter range of β values calculated for the RV-CAR conditions (RV-CAR were ~40% CAR+ while NV-CAR were ~20% CAR+).

A limitation to the data presented here is that since the many gene editing replicates are pooled before they go into the mice, each of the mice had the same batch of cells delivered to them. While the flow cytometry and ELISA data was collected on each individual gene editing replicate, these values had to be averaged as they were pooled together before going into mice. Only pooling 2 or 3 gene editing replicates, instead of all of the replicates, would allow us to have distinct surface expression and cytokine production values for each mouse. This also applies to the microwell data as the cells to be used for the microwells were taken from the pooled populations before infusion into mice. Furthermore, we only had RNAseq data on two of the donors which limits some of the power in those PLSR models.

An important consideration to developing *in vitro* potency assays is that the higher the cell count required to conduct the assays, the more cells that have to be extracted from the manufactured CAR T product and thus are less available as a starting dose for the patients. In addition, there are economies of scale to consider. For example, the IncuCyte requires 50,000 cells for each well whereas the microwells could provide an n=55 with 50,000 cells. Furthermore, decreasing trends of a viable cancer cells can be observed more readily with 2D microwells even when only imaging every 4 hours as opposed to more frequently with the IncuCyte. The lower frequency of imaging needed in the 2D microwell coculture assay both decreases the chances of photo-bleaching and the amount of image processing required to acquire the resulting cytotoxicity value. In terms of aiding in the derivation of a β killing constant for the cytotoxic CAR T cells in the microwells, the higher number of replicates afforded by the microwell system, in addition to the more random seeding of the cells into the wells, allows for better prediction of actual β values. Microwells provide a wide distribution of values, which allows for better prediction and heterogeneity of potential β values.

One potential limitation of the 2D microwell studies were GD2+ M21 human melanoma, not the GD2+ CHLA20 neuroblastoma cells that were used in the IncuCyte and in the xenograft mouse model. Despite the difference in target cancer cells populations, the microwell system still proved to be a suitable surrogate for measuring cytotoxicity for GD2+ tumors by GD2 specific CAR T cells. This indicates that the 2D microwell coculture assay has the potential to be applicable as a potency assay across different solid tumor histologies, but there are still aspects of the treatment of solid tumors with CAR T cells that are not captured within this 2D microwell coculture assay. Little work has been done thus far to identify how much of the infused CAR T product successfully traffics to various tumor sites, and it is feasible that different tumor anatomic

sites and microenvironments will have varying levels of accessibility to infiltrating T cells. The tumor microenvironment itself will also present challenges to the CAR T cells, including hypoxia, low sugar, and presence of immunosuppressive cell subsets and cytokines. Variables that contribute to CAR T exhaustion and immune exclusion may play a large role in inhibiting CAR T cells from successfully causing regression of solid tumors.

The current lack of biomarkers and assays that reliably predict the potency of a CAR T product prior to infusion to patients is a major gap in the field of cancer immunotherapy. Successful development of predictive potency assays and computational models may reduce variation in clinical trial outcomes and has the capacity to predict tumor regression prior to infusion. These data support the development of *in vitro* assays to detect the cytotoxic potential of CAR T products for solid tumors and could be used to probe the cytotoxicity potential of not only immune effector cells being developed for patients, like tumor infiltrating lymphocytes or NK cells, but also induced pluripotent stem cell derived products that could be used for CAR T cell manufacturing [196], [197]. The computational models presented here can be used to quickly assess the cytotoxic potential of CAR T cell products on a batch-to-batch basis pre-infusion and their ability to induce tumor regression post-infusion.

Methods

Cells and Culture. The T cells (NV-CAR and RV-CAR) used in this in vitro cytotoxicity microwell platform were the same cells manufactured in Chapter 2. The NK92 cell line is cultured in Alpha Minimum Essential medium without ribonucleotides and deoxyribonucleosides but with 2 mM L-glutamine and 1.5 g/L sodium bicarbonate and 0.2 mM inositol, 0.1 mM 2-

mercaptoethanol, 0.02 mM folic acid, 100 U/ml recombinant IL-2, 12.5% horse serum, and 12.5% fetal bovine serum.

Microwell Fabrication and Preparation. Polydimethylsiloxane (PDMS) microwells are generated using standard photolithography techniques. In short, soft lithography was used to fabricate a master mold of circular microarray devices, as previously described [198]. Silicon wafers were spin coated with SU-8 100, soft baked and exposed to UV through a transparent mask with the desired pattern before baking again. PDMS was applied to the master molds using a 10:1 ratio of base to curing agent and cured at 80C for 3 hours. PDMS devices were first placed in 95% ethanol for 12-24 hours to remove uncross-linked oligomers. Extracted devices were then dried and plasma bonded to a glass microscope slide. These wells are 300x300um wide and 100um deep. Prior to seeding, microwells are UV sterilized for 15 minutes and coated with 0.1% gelatin for 1 hour.

Co-culture. *Microwells.* 12,000 constitutively expressing H2B-mCherry M21 human melanoma cells are seeded onto each Gelatin coated microfeature in RPMI. M21 are given 24 hours to adhere to the microwells before coculture begins. On the day of imaging, the CellEvent Caspase-3/7 Green Detection Reagent from Thermo Fisher (Catalog # C10423) is prepared at 8uM in Immunocult. Media is pipetted off of the microwells and 40ul of the CellEvent media is applied to the microwells. 60,000 T cells are then seeded on top of the cancer cells (5:1 effector to target ratio). T cells do not undergo FACS prior to seeding on the microwells.

IncuCyte. 10,000 AkaLUC-GFP CHLA20 cells were seeded in wells of a 96 well plate, in triplicate per condition. 48 hours later, 50,000 T cells were added to each well. 1 ul (0.05 ug) of CF® 594 Annexin V antibody (Biotium) was added to the wells. The plate was centrifuged at 100g for 1

minute and then placed in The IncuCyte® S3 Live-Cell Analysis System (Sartorious, Catalog No 4647), stored in a 37C incubator. Images were taken every 2 hours for 48 hours. Green object count was used to calculate the number of cancer cells in each well. Red object count was used to calculate the number of objects staining positive for Annexin V, an early apoptosis marker. Overlap object count was used to calculate the number of dying or dead cancer cells in each well at each timepoint. Figures were produced using GraphPad PRISM 8.

Microwell Co-culture Imaging. A 4-well OmniTray is prepared for imaging by laser cutting a rectangle to remove the plastic bottom and applying a glass bottom sheet. Microwells are placed on top of the glass bottom sheet and water is placed into the adjacent well to prevent evaporation. The OmniTray is placed in a live cell imaging chamber at 37C and 5% CO2. Cells are incubated for 30 minutes prior to round 1 of imaging in order to allow for the T cells to sink as well as for the CellEvent to enter the cells. Cells are imaged on a Nikon Epifluorescent scope using an automated system to image every individual microwell at 10x on TxRed, DAPI, and GFP channels, every 6 hours for a period of 48 hours. At 24 hours, more Immunocult and CellEvent is added to the microwells to make up for volume lost to evaporation.

Image Analysis and Cytotoxicity Measurement. Fiji Is Just ImageJ (FIJI) is used to parse the output files from the Nikon imaging software from one large .nd2 file into smaller .tif files based on condition and timepoint. These .tif files are then analyzed in CellProfiler using a user defined pipeline. This pipeline allows for counting of each cell type in each frame.

The CellProfiler pipeline begins by importing the images to be analyzed, extracting their metadata, and defining names and types for each of the images to be called on later in the pipeline. Images are then cropped to remove any excess image space that does not include the microwell.

From there, the pixel intensity is rescaled to use the full intensity range to provide more contrast for the following pipeline modules to discern one "object" from another. Frames imaged in the mCherry channel are then subject to the "IdentifyPrimaryObjects" module. Objects are defined as areas with a higher brightness index that fit within the estimated range of cell diameter. This module uses a "Global" strategy to define its threshold with an "Otsu" method. Typical diameter of objects in pixel units are between 22 to 60 for the M21 nuclei, as the mCherry signal comes from a fused H2B-mCherry protein. To remove background signal that lead to incorrect object identification, any objects with an eccentricity greater than 0.75 are discarded. The outlines drawn by the identified M21 nuclei are then expanded by 12 pixels, and a mask is created off of these new outlines. This mask of expanded M21 nuclei is then applied to the frames that were imaged in the GFP channel. This ensures that only cells in the same position as the M21 can be identified as dead M21. The diameter of object is helpful here as well the lower limit of the diameter for M21 is still above the upper limit for T cells. The output of CellProfiler is the number of objects, or cells, in each single microwell for each microfeature. This process is repeated for each color channel and time point to measure the change in cell number over time.

Calculating Beta. The counts of the number of M21 and dead M21 undergo Outlier identification in GraphPad Prism using the ROUT method and a Q of 10%. Remaining values are exported to an Excel sheet which is imported into Matlab. A line is plotted for each microwell at all 13 timepoints and the fit(x,y,fitType) function in MatLab was used to fit exponential curves to the data for each microwell. This created an array of a and b values to describe an eqtn(x) = a*exp(b*x) for each microwell. The number of immune cells present in the wells is then plotted on the x-axis and the b value associated with the fit exponential model is plotted on the y-axis. A line is fit to all of these points and the slope of that line is the calculated β for that group of microwells.

Partial Least Squares Regression. PLSR analysis was completed in JMP Pro Software. PLSR was performed using nonlinear iterative partial least squares (NIPALS) method and was validated using the leave one out method.

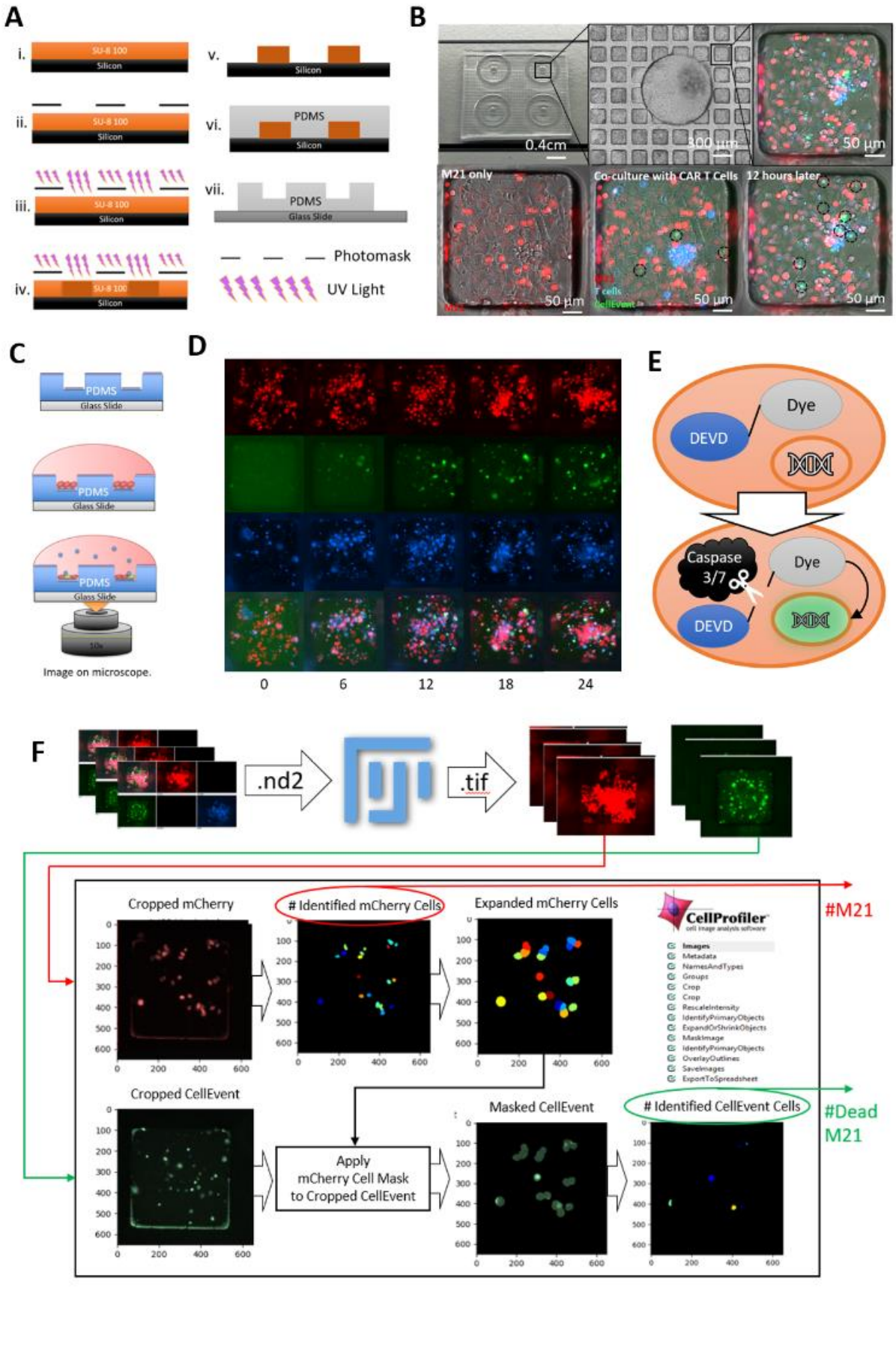
A
i.
SU-8 100
Silicon
ii.
SU-8 100
Silicon
iii.
SU-8 100
Silicon
iv.
SU-8 100
Silicon
v.
Silicon
vi.
PDMS
Silicon
vii.
PDMS
Glass Slide
Photomask
UV Light
B
0.4cm
300 µm
50 µm
M21 only
Co-culture with CAR T Cells
12 hours later
50 µm
50 µm
50 µm
C
PDMS
Glass Slide
PDMS
Glass Slide
PDMS
Glass Slide
Image on microscope.
D
0
6
12
18
24
E
Dye
DEVD
Caspase
3/7
Dye
DEVD
F
.nd2
.tif
Cropped mCherry
Identified mCherry Cells
Expanded mCherry Cells
CellProfiler
cell image analysis software
Images
Metadata
NamesAndTypes
Groups
Crop
Crop
RescaleIntensity
IdentifyPrimaryObjects
ExpandOrShrinkObjects
MaskImage
IdentifyPrimaryObjects
OverlayOutlines
SaveImages
ExportToSpreadsheet
#M21
Cropped CellEvent
Apply
mCherry Cell Mask
to Cropped CellEvent
Masked CellEvent
Identified CellEvent Cells
#Dead
M21

Figure 3.1

Development of a high throughput microwell cytotoxicity assay. A, The photolithography process utilized to construct the PDMS microwells. **B,** Picture of the microwell. **C,** Cell seeding on the microwells. Microwells are coated with 0.1% gelatin and then the H2B-mCherry M21 are seeded and allowed to culture on the microwells for 24 hours before Hoechst stained immune cells are seeded on top of the M21 in a 5:1 immune to cancer cell ratio. **D,** Schematic detailing the cell permeable CellEvent Caspase-3/7 Green Dye. The DEVD peptide quencher is cleaved in the presence of Caspase-3/7 and the nuclei of the dying cells fluoresces green. **E,** Representative images from 1 microwell imaged over time in all three channels with the fourth being merged. **F,** The image analysis pipeline involving FIJI and CellProfiler.

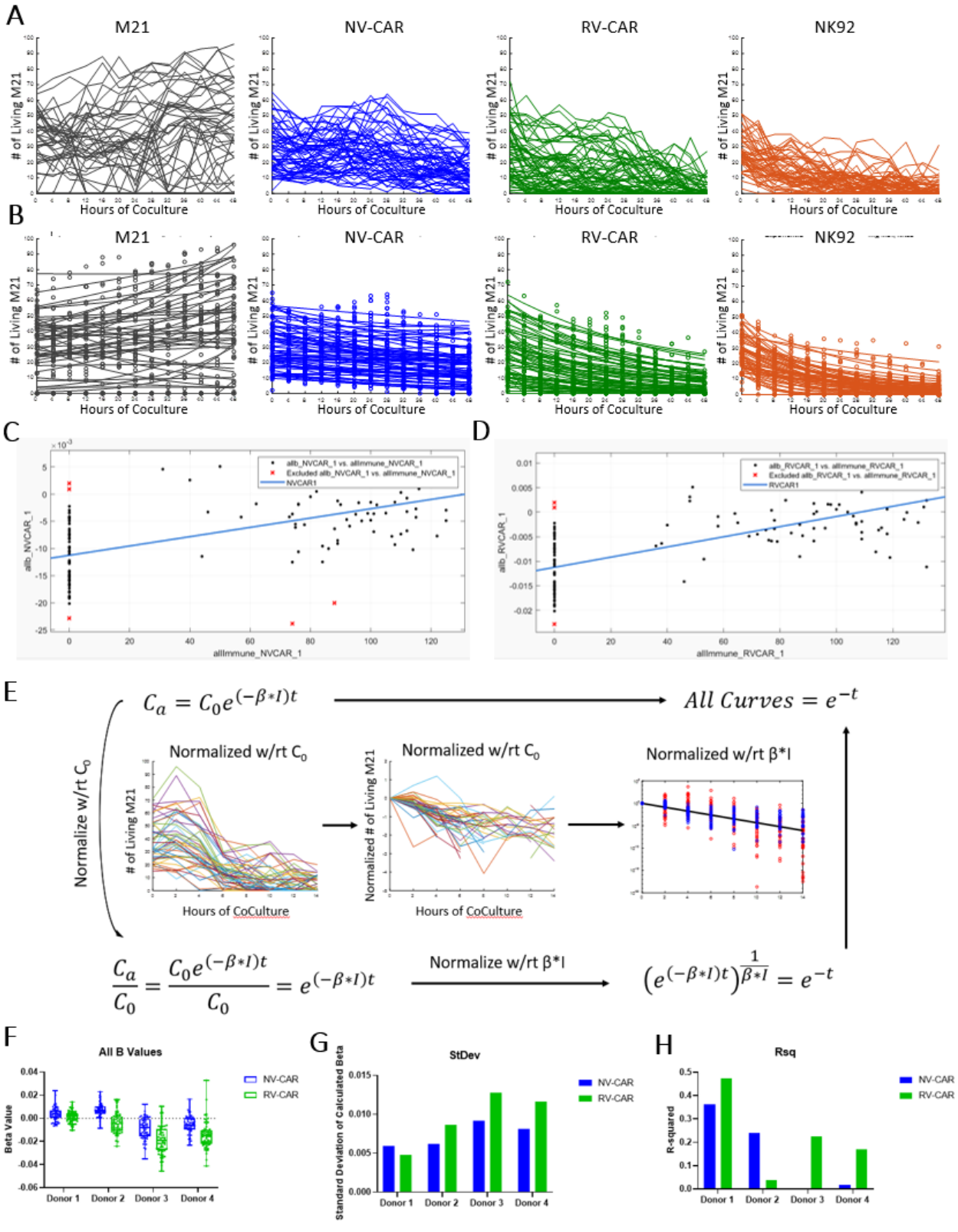
A
M21
NV-CAR
RV-CAR
NK92
# of Living M21
Hours of Coculture
B
C
D
E
Normalize w/rt C0
$C_a = C_0 e^{(-\beta * I)t}$
$All\ Curves = e^{-t}$
Normalized w/rt C0
Normalized w/rt β*I
Hours of CoCulture
Normalized # of Living M21
$\frac{C_a}{C_0} = \frac{C_0 e^{(-\beta * I)t}}{C_0} = e^{(-\beta * I)t}$
Normalize w/rt β*I
$\left(e^{(-\beta * I)t}\right)^{\frac{1}{\beta * I}} = e^{-t}$
F
All B Values
Beta Value
NV-CAR
RV-CAR
Donor 1
Donor 2
Donor 3
Donor 4
G
StDev
Standard Deviation of Calculated Beta
H
Rsq
R-squared

Figure 3.2

Deriving Immune Cell Killing Constants from In Vitro Coculture Systems. A, The number of living M21 cells per microwell, where each line is another microwell. M21 alone without any immune cells in black, M21 with NV-CAR in blue, M21 with RV-CAR in green, M21 with NK92 in orange. n=65 per condition**. B,** The exponential curve fit to each of the number of living cells per microwell, where was line represents the function fit for each microwells. **C,** The transformation of data from the solution to the differential equation. The equation is first normalized with respect to the number of M21 at time zero. Then the universal scaling law for the growth of cancer cells (dots) together with the scaling law. The agreement between our theory and the data suggests that the cancer cells adapt their growth dynamics to the presence of different concentrations of immune cells such that they follow an exponential law. **D,** The line fit to the scatter plot between the number of immune cells at t=0 and the b values calculated from the fit exponential curves for the NV-CAR data. **E,** The line fit for the RV-CAR data. **F,** All of the calculated β values for all 4 donors and both NV-CAR in blue and RV-CAR in green, n=65 per condition per donor. **G,** The standard deviation for each calculated β values. **H,** The r-squared values for the calculated β.

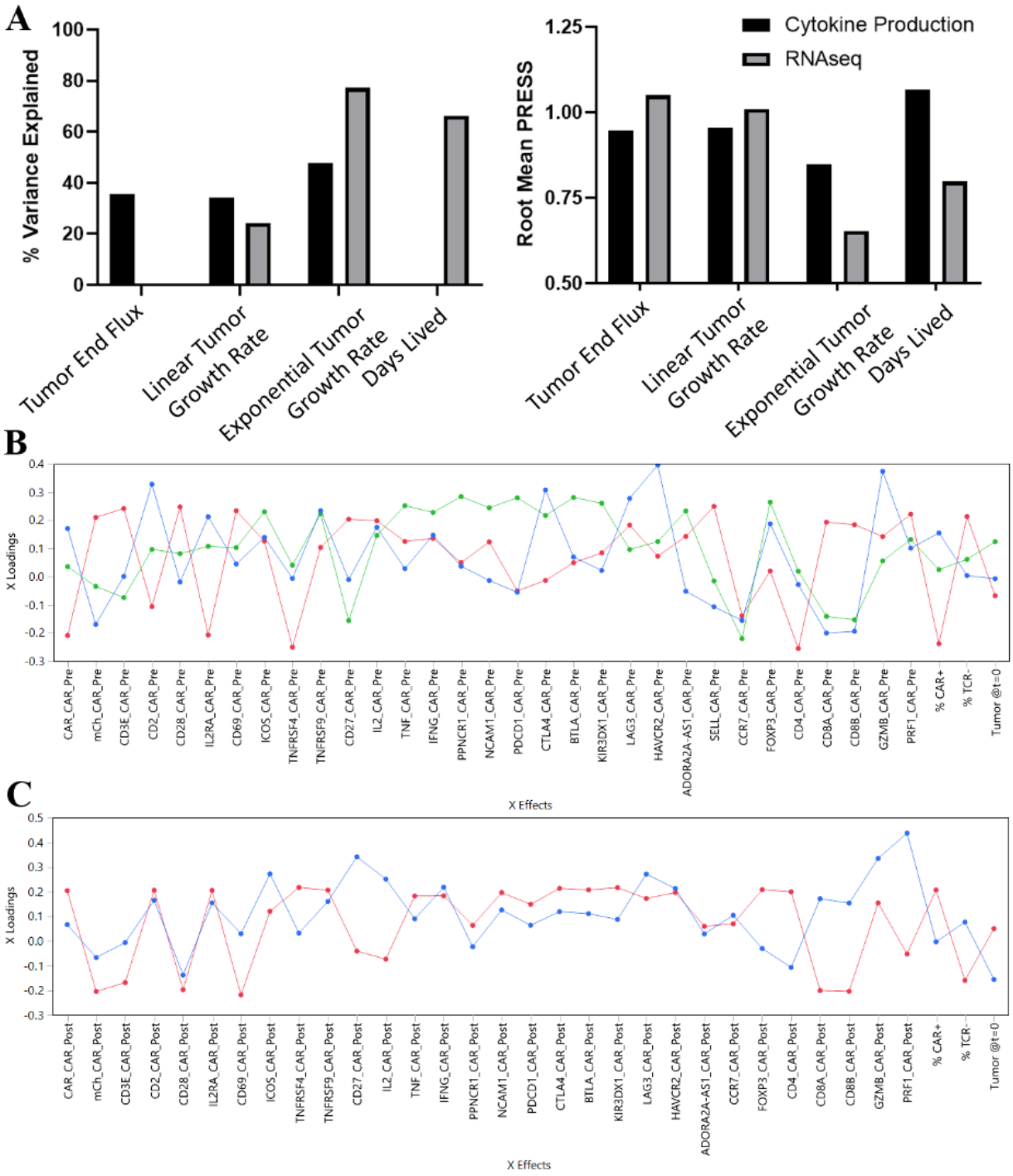
A
% Variance Explained
100
80
60
40
20
0
Tumor End Flux
Linear Tumor Growth Rate
Exponential Tumor Growth Rate
Days Lived
Root Mean PRESS
1.25
1.00
0.75
0.50
Cytokine Production
RNAseq
B
X Loadings
CAR_CAR_Pre
mCh_CAR_Pre
CD3E_CAR_Pre
CD2_CAR_Pre
CD28_CAR_Pre
IL2RA_CAR_Pre
CD69_CAR_Pre
ICOS_CAR_Pre
TNFRSF4_CAR_Pre
TNFRSF9_CAR_Pre
CD27_CAR_Pre
IL2_CAR_Pre
TNF_CAR_Pre
IFNG_CAR_Pre
PPNCR1_CAR_Pre
NCAM1_CAR_Pre
PDCD1_CAR_Pre
CTLA4_CAR_Pre
BTLA_CAR_Pre
KIR3DX1_CAR_Pre
LAG3_CAR_Pre
HAVCR2_CAR_Pre
ADORA2A-AS1_CAR_Pre
SELL_CAR_Pre
CCR7_CAR_Pre
FOXP3_CAR_Pre
CD4_CAR_Pre
CD8A_CAR_Pre
CD8B_CAR_Pre
GZMB_CAR_Pre
PRF1_CAR_Pre
% CAR+
% TCR-
Tumor @t=0
C
X Effects
X Loadings
CAR_CAR_Post
mCh_CAR_Post
CD3E_CAR_Post
CD2_CAR_Post
CD28_CAR_Post
IL2RA_CAR_Post
CD69_CAR_Post
ICOS_CAR_Post
TNFRSF4_CAR_Post
TNFRSF9_CAR_Post
CD27_CAR_Post
IL2_CAR_Post
TNF_CAR_Post
IFNG_CAR_Post
PPNCR1_CAR_Post
NCAM1_CAR_Post
PDCD1_CAR_Post
CTLA4_CAR_Post
BTLA_CAR_Post
KIR3DX1_CAR_Post
LAG3_CAR_Post
HAVCR2_CAR_Post
ADORA2A-AS1_CAR_Post
CCR7_CAR_Post
FOXP3_CAR_Post
CD4_CAR_Post
CD8A_CAR_Post
CD8B_CAR_Post
GZMB_CAR_Post
PRF1_CAR_Post
% CAR+
% TCR-
Tumor @t=0
X Effects

Figure 3.3

Predicting in vivo response with partial least square regression. A, Left, The percent variance explained for each of the various potential predicted variables. Black bars are based on cytokine production values and gray bars for RNA seq data. **Right,** The root mean PRESS values for the PLSR models. **B,** The loadings for the input variables for the pre-antigen exposure RNA seq data PLSR model. Red is Factor 1, Blue is Factor 2, and Green is Factor 3. **C,** The loadings for the input variables for the post-antigen exposure RNA seq data PLSR model. Red is Factor 1, Blue is Factor 2.

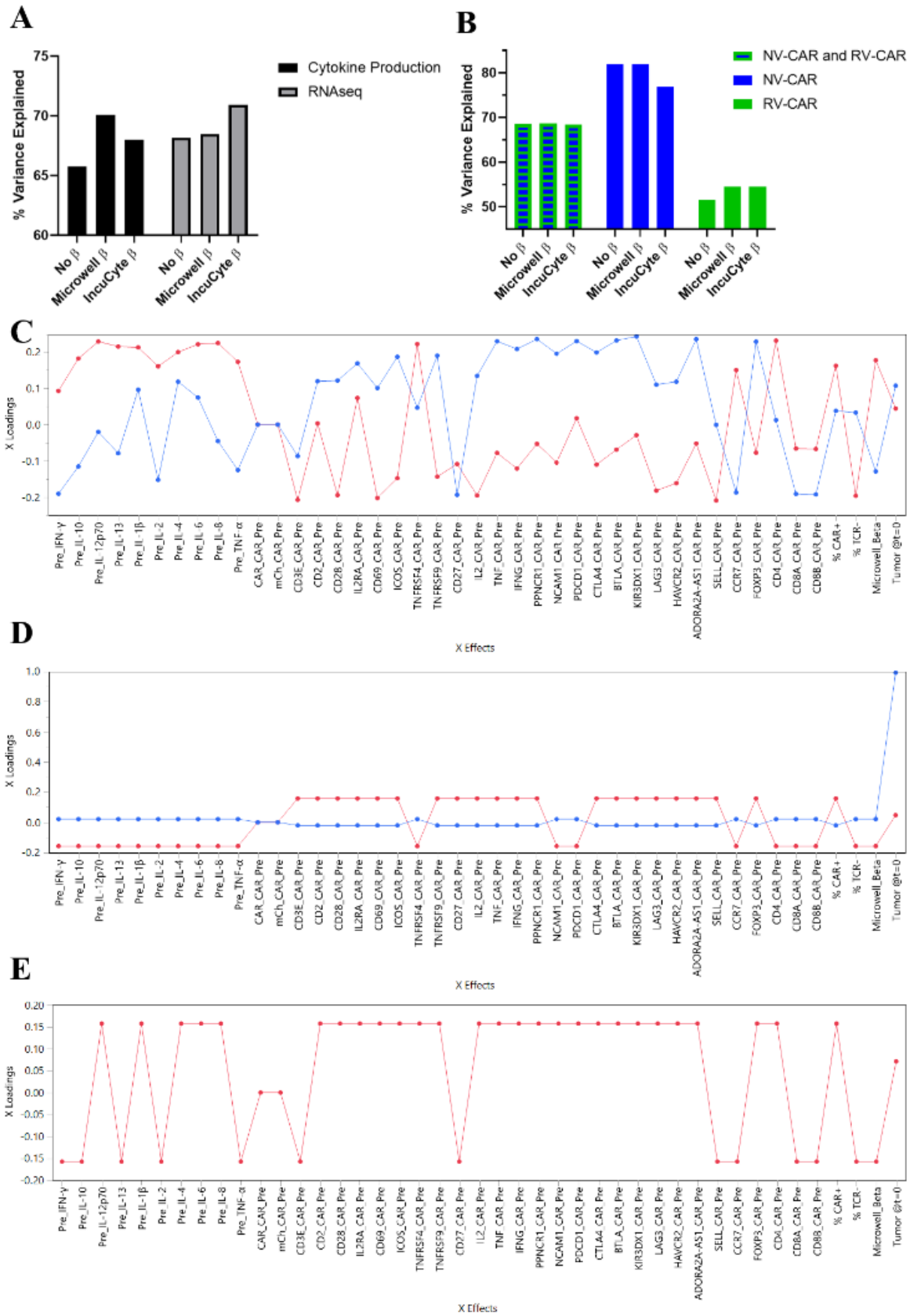
A
% Variance Explained
Cytokine Production
RNAseq
No β
Microwell β
IncuCyte β
B
% Variance Explained
NV-CAR and RV-CAR
NV-CAR
RV-CAR
C
X Loadings
D
X Loadings
X Effects
E
X Loadings
X Effects
Pre_IFN-γ
Pre_IL-10
Pre_IL-12p70
Pre_IL-13
Pre_IL-1β
Pre_IL-2
Pre_IL-4
Pre_IL-6
Pre_IL-8
Pre_TNF-α
CAR_CAR_Pre
mCh_CAR_Pre
CD3E_CAR_Pre
CD2_CAR_Pre
CD28_CAR_Pre
IL2RA_CAR_Pre
CD69_CAR_Pre
ICOS_CAR_Pre
TNFRSF4_CAR_Pre
TNFRSF9_CAR_Pre
CD27_CAR_Pre
IL2_CAR_Pre
TNF_CAR_Pre
IFNG_CAR_Pre
PPNCR1_CAR_Pre
NCAM1_CAR_Pre
PDCD1_CAR_Pre
CTLA4_CAR_Pre
BTLA_CAR_Pre
KIR3DX1_CAR_Pre
LAG3_CAR_Pre
HAVCR2_CAR_Pre
ADORA2A-AS1_CAR_Pre
SELL_CAR_Pre
CCR7_CAR_Pre
FOXP3_CAR_Pre
CD4_CAR_Pre
CD8A_CAR_Pre
CD8B_CAR_Pre
% CAR+
% TCR-
Microwell_Beta
Tumor @t=0

Figure 3.4

Impact of β, and the comparison between NV-CAR and RV-CAR predictability. A, The influence on the percent of variance explained by adding no β, the microwell β, or the IncuCyte β to the pre-antigen exposure cytokine production data only, black bars, or to the pre-antigen exposure RNA seq data only, gray bars. **B,** The influence of adding no β, the microwell β, or the IncuCyte β on the percent of variance explained on the final PLSR model incorporating the pre-antigen exposure cytokine data, pre-antigen exposure RNAseq data, flow cytometry data, and flux at t=0 when using NV-CAR and RV-CAR samples (blue and green striped bars), NV-CAR samples only (blue bars), or RV-CAR samples only (green bars). **C,** The loadings for the input variables for the PLSR model on both the NV-CAR and RV-CAR samples. Red is Factor 1, Blue is Factor 2. **D,** The loadings for the input variables for the PLSR model on the NV-CAR samples only. Red is Factor 1, Blue is Factor 2. **E,** The loadings for the input variables for the PLSR model on the RV-CAR samples only. Red is Factor 1.

CHAPTER 4: Conclusions and Future Directions

This thesis aimed at developing new technologies to engineer more potent and predictable CAR T cell therapies using a fully NV gene editing platform. First, I presented a fully NV method to engineer CAR T cells using CRISPR Cas9 to cut the *TRAC* locus and delivered a PCR product HDR template. Using this platform, we were able to consistently generate 20% CAR + cells per reaction, and these cells had a more desirable phenotype when compared to their retroviral generated counterparts and comparable *in vivo* efficacy. Second, I described a high throughput microwell coculture platform to assess the killing rate of various products consisting of engineered immune cells. This allowed for more precise measurement of the killing rate of these cells, while using fewer cells, in comparison to the current state-of-art systems. Finally, I demonstrated the value of using PLSR to predict the *in vivo* efficacy of engineered cellular therapies prior to infusion into animals. These methods and their applications demonstrate advances in the field of engineered cellular therapies and represent tangible ways to increase the accessibility of novel cell therapies.

Towards More Efficient CAR Cell Manufacture

CAR T cell therapy remains poised to revolutionize cancer treatment. Despite the progress made here, we expect to see progress made in the next decade to increase safety, efficacy, and accessibility of CAR therapies.

Safety

The predominant safety concerns for therapies currently in the clinic are cytokine release syndrome, neurotoxicities, and off-target CAR T cell activity, all of which have resulted in severe adverse events, and in some cases, patient deaths [199]. Efforts to mitigate these issues are of utmost importance. One approach has been to employ small molecule modulation of CAR T cells *in vivo*. For instance, apoptotic switches have been engineered into CAR T cells that allow them to be quickly destroyed if a patient experiences an adverse event [200] (completed clinical trial NCT02107963). Other studies have focused on tuning the functionality of the CAR itself. For instance, CARs have been designed with split signaling and recognition domains, which can be linked to form a single functionally active CAR following drug administration. This small molecule serves as an "ON-switch" for CAR activity, thus allowing it to be controlled or inactivated as necessary [201]. CAR affinities can also be manipulated to preferentially bind cancer cells over healthy tissue, thus preventing off-target effects and diversifying the range of antigens that can be safely targeted [81]. These designs exemplify the growing role for synthetic biology in allowing precise control over CAR T cells after infusion to safeguard the patient.

NV manufacture of CAR therapies can benefit the incorporation of synthetic biology because we have seen how the heterogenous profile of RV manufactured CAR therapies can influence cell behavior. While the genetic engineering above has the potential to create safer therapies, there is no guarantee that all cells in each batch that have been manufactured by viruses

will behave as intended. The TET2 CAR T cell story which showed that one clone could be capable of sending a patient into remission proves that there is potential for one single cell to hinder the reliability of on and off switches if we continue to rely on viral manufacture [202]. The NV workflow established in this thesis has the potential to ensure more predictable cell outcomes, and work in the near future should include determining if this extends to the cells ability to stay on target, as well as respond to "ON-switches" and "OFF-switches".

Bioengineers are also actively developing tissue engineered *in vitro* toxicity models, which may prove useful in the CAR T cell space. For instance, human embryonic stem cells have been used to generate brain organoids as a screening platform for chemical toxicity [203]. These models could be adapted using iPSCs to study neural toxicities on a patient-by-patient basis, thus providing personalized safety checks and quality control. The microwell cytotoxicity assay described in Chapter 3 should be readily adapted to provide more insight into the safety profiles of various gene edits on immune cell populations. Microwell cocultures could also serve as an inexpensive assay to check for GVHD to offer additional low-cost testing of new gene edits to engineer allogeneic therapies. Ultimately, bioengineers may combine *in vitro* modeling tools with *in vivo* synthetic biology approaches to both predict and rapidly reverse adverse events, thereby improving the safety of CAR T cell therapy.

Efficacy

In addition to increasing the overall safety of CAR T cell therapies, bioengineering solutions may also improve their efficacy. The Cas9 work shown here achieved both high knockouts of the TCR and also strong knock-in of the CAR transgene, indicating the potential for additional edits to be made. For instance, multiplexed gene edits may be combined with CAR transgene insertion to

boost CAR T cell performance. CRISPR-Cas9 technologies have been demonstrated to improve the performance of CAR T cells primarily through the knockout of PD-1 to limit *in vivo* exhaustion, and are now in clinical trials in China [204] (NCT02793856). Cellectis has developed CD52/DCK knockout strategies to generate T cells that are chemo-resistant to lymphodepletion agents, thus allowing such drugs to be deployed as combinatorial therapies [205]. Gene editing tools can also enable nuanced recognition of tumor antigens by implementing Boolean logic gates on CAR T cells using synthetic biology approaches [206]. Multiplexed CAR designs implementing AND [143], [207], NOT [208] and OR [209] gates have been demonstrated. The synthetic biology approach to CAR T cell design has also led to tuning CAR affinity to discriminate between healthy and cancerous tissue [81].

Recent modifications to the CRISPR system have been used to tune genomic transcription *in vivo* for directed reprogramming [210]. This approach could potentially be used to tune expression of genes involved in T cell activation or exhaustion, or even to control CAR T cell differentiation post-infusion. Catalytically dead Cas9 proteins, which lack the ability to induce double strand breaks, have been coupled with transcriptional modulators to selectively activate gene expression in various tissue types [211], [212], [213], enabling tunable implementation of biological circuits.

Finally, *in vitro* organ/disease-on-a-chip approaches are actively being developed to probe CAR T cell functionality, with the aim of assessing heterogeneity in T cell populations and selecting for therapeutically effective cells [214]. Like the aforementioned neural organoid models for safety testing, these could be used to recapitulate the patient's cancer microenvironment, thus informing a personalized treatment approach. Ultimately, the field is moving towards building smarter and more efficient CAR T cells, and new modeling technologies may go a long way toward

improving the therapy's reliability [53], [206], [215]. The microwell system described here could be used to assay combinatorial therapies to be delivered alongside CAR T cells. Cocultures could be conducted in the presence or absence of cytokines or small molecules to explore the impact of factors that could be delivered alongside CAR therapies.

Accessibility

As a final consideration, there is a pressing need to increase accessibility to CAR T cell therapies. Current estimates suggest that autologous therapy may cost over $500,000 per patient; as such, new cell sources are highly desirable [216], [217]. While allogeneic therapies have been limited in scope due to the risk of immune rejection, new engineering approaches may allow for the production of non-immunogenic T cells. Work to date has focused on knocking out HLA and the endogenous TCR locus to eliminate alloreactivity, thus creating potent "universal" CAR T cells, which could potentially be produced en masse for large patient populations [218]. Human iPSCs could also be used as a cell source to generate large quantities of T cells for patients for whom sufficient T cells cannot be acquired. Furthermore, elimination of viral vectors, as has been demonstrated here, through the use of novel non-viral transfection techniques could increase accessibility by simplifying manufacturing workflows.

Ultimately, *ex vivo* culture may become irrelevant with the advent of *in situ* transgenesis, which could eliminate significant costs and be easily scaled as an off-the-shelf therapy [219]. In one recent study, nanomaterials were used to perform CAR gene transfer *in situ* using anti-CD3 f(ab')2 fragments coupled to microtubule-associated-nuclear localization peptides to create CAR nanocarriers. These were directly injected into a murine model, resulting in successful regression of leukemia with no obvious toxicity. While still quite recent, this approach has the potential to

produce off-the-shelf gene editing products that eliminate the need for *ex vivo* culture altogether. These approaches highlight an interest in applying bioengineering innovations to move the field away from autologous therapy, and many of the problems inherent to T cell manufacture could be rectified with such an approach.

CAR NK Cells

Over the past few years, we have made efforts in our lab to extend our NV-CAR T manufacture workflow to natural killer (NK) cells. There are clinical trials ongoing with viral manufactured CAR NK cells where the NK cells come from the NK92 cell line. Using a cytotoxic cell line allows for a fully "off-the-shelf" product to be established. As the CAR NK92 cells are irradiated prior to infusion, such as to limit their ability to proliferate *in vivo*, CAR NK92 can be considered as a "booster shot" to be used in parallel to CAR T cell therapy. The CAR NK could either be used to bridge patients prior to their CAR T cell infusion, or they could be delivered alongside the CAR T cells to serve as an additional set of cytotoxic cells to give the CAR therapy an added kick, and can do so hopefully without additional side effects as they would not proliferate and therefore, not add to cytokine storms. Given that CAR NK92 are allogeneic, using Cas9 to engineer these cells in a fully non-viral manner will likely allow for level of homogeneity in the final cell product not seen in even a fully allogeneic CAR T cell product as one line of cells could theoretically treat all patients.

While targeting the CAR in the TRAC locus has added benefits for CAR T therapy, there is likely a NK cell specific locus that when the CAR transgene is placed there, affords the CAR NK cells additional functionality over viral manufactured counterparts where the CAR gene is randomly inserted in the genome. The loci for integration should be readily expressed in NK cells

and the knockout of it through gene disruption should be beneficial to the intended function. These NV-CAR NK cells could undergo the same assays as were conducted in Chapters 2 and 3 to measure their predictability. More complex mathematical models could then be developed to determine an optimal dosing strategy for a combination of CAR T and CAR NK therapy.

Generating More Predictable CAR T Cells using CRISPR/Cas9

In conclusion, not only can viral delivery of the CAR gene result in negative events such as oncogenesis and transduction of resistance, but viral delivery also has a higher inherent variability during the process of integration than precise gene editing does when using CRISPR-Cas9 HDR [167],[141]. Creating safer, and more homogenous CAR T cell products has the potential to create more effective CAR T cell therapies. By delivering the CAR gene to the *TRAC* locus using Cas9, the CAR transgenes will be surrounded by the same genetic regulatory elements and have similar expression levels, thus resulting in decreased heterogeneity [3]. Furthermore, delivery of the Cas9 and sgRNA as a ribonucleoprotein (RNP) will be clinically translatable because RNP delivery has shown lower rates of off target activity when compared to delivering Cas9 on a plasmid [220]. Coupling this new method of gene delivery with pre-infusion functional measurements such as cytokine production or cytotoxicity assays can allow for more predictive therapies. As the field progresses, it is hoped that CAR T cells may prove to be a safe and viable treatment for patients with diverse malignancies, and perhaps finally offering cures for conditions that previously had no treatment.

REFERENCES

[1] M. Sadelain, I. Rivière, and R. Brentjens, "Targeting tumours with genetically enhanced T lymphocytes.," *Nat. Rev. Cancer*, vol. 3, no. 1, pp. 35–45, 2003.

[2] N. J. Piscopo *et al.*, "Bioengineering Solutions for Manufacturing Challenges in CAR T Cells," *Biotechnol. J.*, vol. 13, no. 2, p. 1700095, Feb. 2018.

[3] M. Kranz *et al.*, "Comparison of T Cell Activities Mediated by Human TCRs and CARs That Use the Same Recognition Domains," *J. Immunol.*, vol. 200, pp. 1088–1100, 2018.

[4] P. Salmikangas, N. Kinsella, and P. Chamberlain, "Chimeric Antigen Receptor T-Cells (CAR T-Cells) for Cancer Immunotherapy – Moving Target for Industry?," *Pharm Res*, vol. 35, no. 152, pp. 151–159, 2018.

[5] S. Lin-Gibson, K. C. Rogers, and A. L. Plant, "Measurement Challenges for CAR-T Biomanufacturing: Highlights from a Meeting Sponsored by the National Institute of Standards and Technology (NIST)," *Hum. Gene Ther. Clin. Dev.*, vol. 27, no. 2, pp. 66–68, 2016.

[6] M. A. Huang, D. K. Krishnadas, and K. G. Lucas, "Cellular and Antibody Based Approaches for Pediatric Cancer Immunotherapy.," *J. Immunol. Res.*, vol. 2015, p. 675269, 2015.

[7] A. G. Murphy and L. Zheng, "Small molecule drugs with immunomodulatory effects in cancer.," *Hum. Vaccin. Immunother.*, vol. 11, no. 10, pp. 2463–8, 2015.

[8] S. A. Rosenberg, N. P. Restifo, J. C. Yang, R. A. Morgan, and M. E. Dudley, "Adoptive cell transfer: a clinical path to effective cancer immunotherapy," *Nat. Rev. Cancer*, vol. 8, no. 4, pp. 299–308, Apr. 2008.

[9] I. Mellman, G. Coukos, and G. Dranoff, "Cancer immunotherapy comes of age," *Nature*, vol. 480, no. 7378, pp. 480–489, Dec. 2011.

[10] M. Sadelain, R. Brentjens, and I. Rivière, "The basic principles of chimeric antigen receptor design," *Cancer Discov.*, vol. 3, no. 4, pp. 388–398, 2013.

[11] J. Maher, R. J. Brentjens, G. Gunset, I. Rivière, and M. Sadelain, "Human T-lymphocyte cytotoxicity and proliferation directed by a single chimeric TCRζ /CD28 receptor," *Nat. Biotechnol.*, vol. 20, no. 1, pp. 70–75, Jan. 2002.

[12] M. C. Jensen, L. J. N. Cooper, A. M. Wu, S. J. Forman, and A. Raubitschek, "Engineered CD20-specific primary human cytotoxic T lymphocytes for targeting B-cell malignancy," *Cytotherapy*, vol. 5, no. 2, pp. 131–138, 2003.

[13] T. Boon, P. G. Coulie, and B. Van den Eynde, "Tumor antigens recognized by T cells.," *Immunol. Today*, vol. 18, no. 6, pp. 267–8, Jun. 1997.

[14] L. J. Old and Y. T. Chen, "New paths in human cancer serology.," *J. Exp. Med.*, vol. 187, no. 8, pp. 1163–7, Apr. 1998.

[15] N. Vigneron, "Human Tumor Antigens and Cancer Immunotherapy," *Biomed Res. Int.*,

vol. 2015, pp. 1–17, 2015.

[16] M. L. Davila *et al.*, “Efficacy and Toxicity Management of 19-28z CAR T Cell Therapy in B Cell Acute Lymphoblastic Leukemia,” *Sci. Transl. Med.*, vol. 6, no. 224, Feb. 2014.

[17] G. Gross, T. Waks, and Z. Eshhar, “Expression of immunoglobulin-T-cell receptor chimeric molecules as functional receptors with antibody-type specificity.,” *Proc. Natl. Acad. Sci. U. S. A.*, vol. 86, no. 24, pp. 10024–8, Dec. 1989.

[18] M. C. Jensen and S. R. Riddell, “Design and implementation of adoptive therapy with chimeric antigen receptor-modified T cells,” *Immunol. Rev.*, vol. 257, no. 1, pp. 127–144, Jan. 2014.

[19] X. Wang and I. Rivière, “Manufacture of tumor- and virus-specific T lymphocytes for adoptive cell therapies.,” *Cancer Gene Ther.*, vol. 22, no. 2, pp. 85–94, 2015.

[20] S. Tyagarajan, T. Spencer, and J. Smith, “Optimizing CAR-T Cell Manufacturing Processes during Pivotal Clinical Trials,” *Molecular Therapy - Methods and Clinical Development*, vol. 16. Cell Press, pp. 136–144, 13-Mar-2020.

[21] Novartis, “CTL019 (tisagenlecleucel),” in *Oncologic Drugs Advisory Committee*, 2017.

[22] Z. Wang, Z. Wu, Y. Liu, and W. Han, “New development in CAR-T cell therapy,” *J. Hematol. Oncol.*, vol. 10, no. 1, p. 53, Feb. 2017.

[23] M. V Maus, S. a Grupp, D. L. Porter, and C. H. June, “Antibody-modified T cells: CARs take the front seat for hematologic malignancies,” *Blood*, vol. 123, no. 17, pp. 2625–2635, 2014.

[24] H. Auchincloss and D. H. Sachs, “Xenogeneic Transplantation,” *Annu. Rev. Immunol.*, vol. 16, no. 1, pp. 433–470, Apr. 1998.

[25] M. T. de la Morena and R. A. Gatti, “A History of Bone Marrow Transplantation,” *Hematol. Oncol. Clin. North Am.*, vol. 25, no. 1, pp. 1–15, Feb. 2011.

[26] R. R. Jenq and M. R. M. van den Brink, “Allogeneic haematopoietic stem cell transplantation: individualized stem cell and immune therapy of cancer,” *Nat. Rev. Cancer*, vol. 10, no. 3, pp. 213–221, Mar. 2010.

[27] D. Lorusso, E. Bria, A. Costantini, M. Di Maio, G. Rosti, and A. Mancuso, “Patients’ perception of chemotherapy side effects: Expectations, doctor-patient communication and impact on quality of life - An Italian survey,” *Eur. J. Cancer Care (Engl).*, vol. 26, no. 2, p. e12618, Mar. 2017.

[28] M. O. Jamil and S. Mineishi, “State-of-the-art acute and chronic GVHD treatment,” *Int. J. Hematol.*, vol. 101, no. 5, pp. 452–466, May 2015.

[29] D. E. Gilham, R. Debets, M. Pule, R. E. Hawkins, and H. Abken, “CAR–T cells and solid tumors: tuning T cells to challenge an inveterate foe,” *Trends Mol. Med.*, vol. 18, no. 7, pp. 377–384, Jul. 2012.

[30] C. U. Louis *et al.*, “Antitumor activity and long-term fate of chimeric antigen receptor-positive T cells in patients with neuroblastoma.,” *Blood*, vol. 118, no. 23, pp. 6050–6,

Dec. 2011.

[31] J. N. Kochenderfer and S. A. Rosenberg, “Treating B-cell cancer with T cells expressing anti-CD19 chimeric antigen receptors,” *Nat. Rev. Clin. Oncol.*, vol. 10, no. 5, pp. 267–276, Apr. 2013.

[32] I. Ray-Coquard *et al.*, “Lymphopenia as a Prognostic Factor for Overall Survival in Advanced Carcinomas, Sarcomas, and Lymphomas,” *Cancer Res.*, vol. 69, no. 13, 2009.

[33] C. D. Bolan *et al.*, “Pediatric large-volume leukapheresis: a single institution experience with heparin versus citrate-based anticoagulant regimens.,” *Transfusion*, vol. 44, no. 2, pp. 229–38, Feb. 2004.

[34] G. Lee and G. M. Arepally, “Anticoagulation techniques in apheresis: from heparin to citrate and beyond.,” *J. Clin. Apher.*, vol. 27, no. 3, pp. 117–25, 2012.

[35] J. Yang *et al.*, “The effects of storage temperature on PBMC gene expression,” *BMC Immunol.*, vol. 17, no. 1, p. 6, Dec. 2016.

[36] J. Weiner *et al.*, “Restimulation After Cryopreservation and Thawing Preserves the Phenotype and Function of Expanded Baboon Regulatory T Cells.,” *Transplant. direct*, vol. 1, no. 1, pp. 1–7, Feb. 2015.

[37] M. A. Cheever and C. S. Higano, “PROVENGE (Sipuleucel-T) in Prostate Cancer: The First FDA-Approved Therapeutic Cancer Vaccine,” *Clin. Cancer Res.*, vol. 17, no. 11, pp. 3520–3526, Jun. 2011.

[38] K. Coopman and N. Medcalf, *From production to patient: challenges and approaches for delivering cell therapies*. Harvard Stem Cell Institute, 2008.

[39] S. Jarosławski and M. Toumi, “Sipuleucel-T (Provenge®) - Autopsy of an Innovative Paradigm Change in Cancer Treatment: Why a Single-Product Biotech Company Failed to Capitalize on its Breakthrough Invention,” *BioDrugs*, vol. 29, no. 5. Springer International Publishing, pp. 301–307, 01-Oct-2015.

[40] A. D. Kaiser *et al.*, “Towards a commercial process for the manufacture of genetically modified T cells for therapy.,” *Cancer Gene Ther.*, vol. 22, no. 2, pp. 72–8, 2015.

[41] J. Hanna, A. Hubel, and E. Lemke, “Diffusion-based extraction of DMSO from a cell suspension in a three stream, vertical microchannel.,” *Biotechnol. Bioeng.*, vol. 109, no. 9, pp. 2316–24, Sep. 2012.

[42] J. M. Baust, Van Buskirk, and J. G. Baust, “Cell viability improves following inhibition of cryopreservation-induced apoptosis.,” *In Vitro Cell. Dev. Biol. Anim.*, vol. 36, no. 4, pp. 262–70, Apr. 2000.

[43] S. Gill, M. V. Maus, and D. L. Porter, “Chimeric antigen receptor T cell therapy: 25 years in the making,” *Blood Rev.*, vol. 30, no. 3, pp. 157–167, 2016.

[44] E. J. Wherry, “T cell exhaustion.,” *Nat. Immunol.*, vol. 12, no. 6, pp. 492–499, 2011.

[45] H. Singh *et al.*, “Manufacture of Clinical-Grade CD19-Specific T Cells Stably Expressing Chimeric Antigen Receptor Using Sleeping Beauty System and Artificial Antigen

Presenting Cells," *PLoS One*, vol. 8, no. 5, p. e64138, May 2013.

[46] M. Oelke, M. V. Maus, D. Didiano, C. H. June, A. Mackensen, and J. P. Schneck, "Ex vivo induction and expansion of antigen-specific cytotoxic T cells by HLA-Ig–coated artificial antigen-presenting cells," *Nat. Med.*, vol. 9, no. 5, pp. 619–625, May 2003.

[47] M. M. Suhoski *et al.*, "Engineering Artificial Antigen-presenting Cells to Express a Diverse Array of Co-stimulatory Molecules," *Mol. Ther.*, vol. 15, no. 5, pp. 981–988, May 2007.

[48] T. Harkness *et al.*, "High-content imaging with micropatterned multiwell plates reveals influence of cell geometry and cytoskeleton on chromatin dynamics," *Biotechnol. J.*, vol. 10, no. 10, pp. 1555–1567, 2015.

[49] D. G. Belair *et al.*, "Differential regulation of angiogenesis using degradable VEGF-binding microspheres.," *Biomaterials*, vol. 93, pp. 27–37, Jul. 2016.

[50] E. J. Wherry and M. Kurachi, "Molecular and cellular insights into T cell exhaustion," *Nat. Rev. Immunol.*, vol. 15, no. 8, pp. 486–499, 2015.

[51] K. Yu, Y. Mei, N. Hadjesfandiari, and J. N. Kizhakkedathu, "Engineering biomaterials surfaces to modulate the host response.," *Colloids Surf. B. Biointerfaces*, vol. 124, pp. 69–79, Dec. 2014.

[52] K. Shen, V. K. Thomas, M. L. Dustin, and L. C. Kam, "Micropatterning of costimulatory ligands enhances CD4+ T cell function," *Proc. Natl. Acad. Sci.*, vol. 105, no. 22, pp. 7791–7796, Jun. 2008.

[53] B. L. Levine, J. Miskin, K. Wonnacott, and C. Keir, "Global Manufacturing of CAR T Cell Therapy," *Mol. Ther. - Methods Clin. Dev.*, vol. 4, pp. 92–101, 2017.

[54] X. Wang and I. Rivière, "Clinical manufacturing of CAR T cells: foundation of a promising therapy," *Mol. Ther. - Oncolytics*, vol. 3, p. 16015, 2016.

[55] L. S. Hami, C. Green, N. Leshinsky, E. Markham, K. Miller, and S. Craig, "GMP production and testing of Xcellerated T Cells for the treatment of patients with CLL.," *Cytotherapy*, vol. 6, no. 6, pp. 554–62, 2004.

[56] F. Zhu *et al.*, "CAR-T Cell Production Using the Clinimacs® Prodigy System," *Blood*, vol. 128, no. 22, 2016.

[57] A.-M. Rasmussen *et al.*, "Ex vivo expansion protocol for human tumor specific T cells for adoptive T cell therapy," *J. Immunol. Methods*, vol. 355, no. 1–2, pp. 52–60, Apr. 2010.

[58] S. S. Ozturk, "Engineering challenges in high density cell culture systems," *Cytotechnology*, vol. 22, no. 1–3, pp. 3–16, 1996.

[59] M. Liu and C. T. Goudar, "Gene expression profiling for mechanistic understanding of cellular aggregation in mammalian cell perfusion cultures," *Biotechnol. Bioeng.*, vol. 110, no. 2, pp. 483–490, Feb. 2013.

[60] B. D. Plouffe, S. K. Murthy, and L. H. Lewis, "Fundamentals and application of magnetic particles in cell isolation and enrichment: a review.," *Rep. Prog. Phys.*, vol. 78, no. 1, p.

016601, Jan. 2015.

[61] A. C. Schnitzler *et al.*, “Bioprocessing of human mesenchymal stem/stromal cells for therapeutic use: Current technologies and challenges,” *Biochem. Eng. J.*, vol. 108, pp. 3–13, Apr. 2016.

[62] N. Wung, S. M. Acott, D. Tosh, and M. J. Ellis, “Hollow fibre membrane bioreactors for tissue engineering applications,” *Biotechnol. Lett.*, vol. 36, no. 12, pp. 2357–2366, Dec. 2014.

[63] F. Meuwly, P.-A. Ruffieux, A. Kadouri, and U. von Stockar, “Packed-bed bioreactors for mammalian cell culture: Bioprocess and biomedical applications,” *Biotechnol. Adv.*, vol. 25, no. 1, pp. 45–56, Jan. 2007.

[64] A. Foerster *et al.*, “Stainless steel surface functionalization for immobilization of antibody fragments for cardiovascular applications,” *J. Biomed. Mater. Res. Part A*, vol. 104, no. 4, pp. 821–832, Apr. 2016.

[65] A. Kumar, A. Srivastava, I. Y. Galaev, and B. Mattiasson, “Smart polymers: Physical forms and bioengineering applications,” *Prog. Polym. Sci.*, vol. 32, no. 10, pp. 1205–1237, 2007.

[66] A. Kumar, M. Kamihira, I. Y. Galaev, B. Mattiasson, and S. Iijima, “Type-specific separation of animal cells in aqueous two-phase systems using antibody conjugates with temperature-sensitive polymers.,” *Biotechnol. Bioeng.*, vol. 75, no. 5, pp. 570–80, Dec. 2001.

[67] R. Zenobi, “Single-Cell Metabolomics: Analytical and Biological Perspectives,” *Science (80-.).*, vol. 342, no. 6163, pp. 1243259–1243259, Dec. 2013.

[68] P. K. Chrysanthopoulos, C. T. Goudar, and M. I. Klapa, “Metabolomics for high-resolution monitoring of the cellular physiological state in cell culture engineering.,” *Metab. Eng.*, vol. 12, no. 3, pp. 212–22, May 2010.

[69] S. Tohyama *et al.*, “Distinct Metabolic Flow Enables Large-Scale Purification of Mouse and Human Pluripotent Stem Cell-Derived Cardiomyocytes,” *Cell Stem Cell*, vol. 12, no. 1, pp. 127–137, Jan. 2013.

[70] A. Ramanathan and S. L. Schreiber, “Direct control of mitochondrial function by mTOR.,” *Proc. Natl. Acad. Sci. U. S. A.*, vol. 106, no. 52, pp. 22229–32, Dec. 2009.

[71] J. D. Powell and G. M. Delgoffe, “The mammalian target of rapamycin: linking T cell differentiation, function, and metabolism.,” *Immunity*, vol. 33, no. 3, pp. 301–11, Sep. 2010.

[72] C. A. Opitz *et al.*, “An endogenous tumour-promoting ligand of the human aryl hydrocarbon receptor.,” *Nature*, vol. 478, no. 7368, pp. 197–203, Oct. 2011.

[73] C.-H. Chang and E. L. Pearce, “Emerging concepts of T cell metabolism as a target of immunotherapy.,” *Nat. Immunol.*, vol. 17, no. 4, pp. 364–8, Apr. 2016.

[74] E. L. Carr *et al.*, “Glutamine Uptake and Metabolism Are Coordinately Regulated by

ERK/MAPK during T Lymphocyte Activation," *J. Immunol.*, vol. 185, no. 2, pp. 1037–1044, Jul. 2010.

[75] R. Geiger *et al.*, "L-Arginine Modulates T Cell Metabolism and Enhances Survival and Anti-tumor Activity," *Cell*, vol. 167, no. 3, pp. 829-842.e13, Oct. 2016.

[76] J. Lee, M. C. Walsh, K. L. Hoehn, D. E. James, E. J. Wherry, and Y. Choi, "Regulator of Fatty Acid Metabolism, Acetyl Coenzyme A Carboxylase 1, Controls T Cell Immunity," *J. Immunol.*, vol. 192, no. 7, pp. 3190–3199, Apr. 2014.

[77] M. C. Skala *et al.*, "In vivo multiphoton microscopy of NADH and FAD redox states, fluorescence lifetimes, and cellular morphology in precancerous epithelia.," *Proc. Natl. Acad. Sci. U. S. A.*, vol. 104, no. 49, pp. 19494–9, Dec. 2007.

[78] J. R. Kraly, R. E. Holcomb, Q. Guan, and C. S. Henry, "Review: Microfluidic applications in metabolomics and metabolic profiling.," *Anal. Chim. Acta*, vol. 653, no. 1, pp. 23–35, Oct. 2009.

[79] B. Tumaini *et al.*, "Simplified process for the production of anti-CD19-CAR-engineered T cells.," *Cytotherapy*, vol. 15, no. 11, pp. 1406–15, Nov. 2013.

[80] S. Hacein-Bey-Abina *et al.*, "Insertional oncogenesis in 4 patients after retrovirus-mediated gene therapy of SCID-X1.," *J. Clin. Invest.*, vol. 118, no. 9, pp. 3132–42, Sep. 2008.

[81] H. G. Caruso *et al.*, "Tuning Sensitivity of CAR to EGFR Density Limits Recognition of Normal Tissue While Maintaining Potent Antitumor Activity," *Cancer Res.*, vol. 75, no. 17, pp. 3505–3518, Sep. 2015.

[82] J. Eyquem *et al.*, "Targeting a CAR to the TRAC locus with CRISPR/Cas9 enhances tumour rejection," *Nature*, vol. 543, no. 7643, pp. 113–117, 2017.

[83] C. L. Nobles, J. J. Melenhorst, and F. D. Bushman, "CD19-targeting CAR T cell immunotherapy outcomes correlate with genomic modification by vector integration Graphical abstract The Journal of Clinical Investigation," 2019.

[84] R. Morenweiser, "Downstream processing of viral vectors and vaccines," *Gene Ther.*, vol. 12, pp. S103–S110, Oct. 2005.

[85] A. McCarron, M. Donnelley, C. McIntyre, and D. Parsons, "Challenges of up-scaling lentivirus production and processing.," *J. Biotechnol.*, vol. 240, pp. 23–30, Dec. 2016.

[86] Z. Ivics, P. B. Hackett, R. H. Plasterk, and Z. Izsvák, "Molecular Reconstruction of Sleeping Beauty, a Tc1-like Transposon from Fish, and Its Transposition in Human Cells," *Cell*, vol. 91, no. 4, pp. 501–510, Nov. 1997.

[87] S. Ding, X. Wu, G. Li, M. Han, Y. Zhuang, and T. Xu, "Efficient Transposition of the piggyBac (PB) Transposon in Mammalian Cells and Mice," *Cell*, vol. 122, no. 3, pp. 473–483, Aug. 2005.

[88] R. Monjezi *et al.*, "Enhanced CAR T-cell engineering using non-viral Sleeping Beauty transposition from minicircle vectors.," *Leukemia*, vol. 31, no. 1, pp. 186–194, Jan. 2017.

[89] H. Singh, J. Moyes, M. Huls, and L. Cooper, “Manufacture of T cells using the Sleeping Beauty system to enforce expression of a CD19-specific chimeric antigen receptor,” *Cancer Gene Ther.*, vol. 2269, no. 10, pp. 95–100, 2015.

[90] P. V. R. Manuri *et al.*, “*piggyBac* Transposon/Transposase System to Generate CD19-Specific T Cells for the Treatment of B-Lineage Malignancies,” *Hum. Gene Ther.*, vol. 21, no. 4, pp. 427–437, Apr. 2010.

[91] S. Saha, L. E. Woodard, E. M. Charron, R. C. Welch, C. M. Rooney, and M. H. Wilson, “Evaluating the potential for undesired genomic effects of the piggyBac transposon system in human cells.,” *Nucleic Acids Res.*, vol. 43, no. 3, pp. 1770–82, Feb. 2015.

[92] Y. G. Kim, J. Cha, and S. Chandrasegaran, “Hybrid restriction enzymes: zinc finger fusions to Fok I cleavage domain.,” *Proc. Natl. Acad. Sci. U. S. A.*, vol. 93, no. 3, pp. 1156–60, Feb. 1996.

[93] J. Boch *et al.*, “Breaking the code of DNA binding specificity of TAL-type III effectors.,” *Science*, vol. 326, no. 5959, pp. 1509–12, Dec. 2009.

[94] A. Lombardo *et al.*, “Site-specific integration and tailoring of cassette design for sustainable gene transfer,” *Nat. Methods*, vol. 8, no. 10, pp. 861–869, Aug. 2011.

[95] Y. Kim *et al.*, “A library of TAL effector nucleases spanning the human genome,” *Nat. Biotechnol.*, vol. 31, no. 3, pp. 251–258, Feb. 2013.

[96] Y. Doyon *et al.*, “Enhancing zinc-finger-nuclease activity with improved obligate heterodimeric architectures.,” *Nat. Methods*, vol. 8, no. 1, pp. 74–9, Jan. 2011.

[97] X. M. Anguela *et al.*, “Robust ZFN-mediated genome editing in adult hemophilic mice.,” *Blood*, vol. 122, no. 19, pp. 3283–7, Nov. 2013.

[98] R. A. Voit, M. A. McMahon, S. L. Sawyer, and M. H. Porteus, “Generation of an HIV resistant T-cell line by targeted "stacking" of restriction factors.,” *Mol. Ther.*, vol. 21, no. 4, pp. 786–95, Apr. 2013.

[99] W. Qasim *et al.*, “Molecular remission of infant B-ALL after infusion of universal TALEN gene-edited CAR T cells,” *Sci. Transl. Med.*, vol. 9, no. 374, 2017.

[100] P. D. Hsu, E. S. Lander, and F. Zhang, “Development and Applications of CRISPR-Cas9 for Genome Engineering,” *Cell*, vol. 157, no. 6, pp. 1262–1278, Jun. 2014.

[101] M. Jinek, K. Chylinski, I. Fonfara, M. Hauer, J. A. Doudna, and E. Charpentier, “A programmable dual-RNA-guided DNA endonuclease in adaptive bacterial immunity.,” *Science*, vol. 337, no. 6096, pp. 816–21, Aug. 2012.

[102] L. Cong *et al.*, “Multiplex genome engineering using CRISPR/Cas systems.,” *Science*, vol. 339, no. 6121, pp. 819–23, Feb. 2013.

[103] P. Mali *et al.*, “RNA-guided human genome engineering via Cas9.,” *Science*, vol. 339, no. 6121, pp. 823–6, Feb. 2013.

[104] T. L. Roth *et al.*, “Reprogramming human T cell function and specificity with non-viral genome targeting,” *Nature*, vol. 559, no. 7714, pp. 405–409, Jul. 2018.

[105] Z. Odé, J. Condori, N. Peterson, S. Zhou, and G. Krenciute, “CRISPR-Mediated Non-Viral Site-Specific Gene Integration and Expression in T Cells : Protocol and Application for T-Cell Therapy,” *Cancers (Basel).*, pp. 1–16, 2020.

[106] E. A. Stadtmauer *et al.*, “CRISPR-engineered T cells in patients with refractory cancer,” *Science (80-.).*, vol. 367, no. 6481, Feb. 2020.

[107] N. N. Malik and M. B. Durdy, “Commercialisation of CAR T-cell therapies: business model spectrum,” *Drug Discovery Today*, vol. 22, no. 1. pp. 1–4, 2017.

[108] D. Q. Mayne, J. B. Rawlings, C. V. Rao, and P. O. M. Scokaert, “Constrained model predictive control: Stability and optimality,” *Automatica*, vol. 36, no. 6, pp. 789–814, Jun. 2000.

[109] W. Sommeregger, B. Sissolak, K. Kandra, M. von Stosch, M. Mayer, and G. Striedner, “Quality by control: Towards model predictive control of mammalian cell culture bioprocesses,” *Biotechnol. J.*, p. 1600546, Mar. 2017.

[110] D. A. M. Pais, M. J. Carrondo, P. M. Alves, and A. P. Teixeira, “Towards real-time monitoring of therapeutic protein quality in mammalian cell processes,” *Curr. Opin. Biotechnol.*, vol. 30, pp. 161–167, Dec. 2014.

[111] M. A. Orman, F. Berthiaume, I. P. Androulakis, and M. G. Ierapetritou, “Advanced stoichiometric analysis of metabolic networks of mammalian systems.,” *Crit. Rev. Biomed. Eng.*, vol. 39, no. 6, pp. 511–34, 2011.

[112] J. W. Locasale and L. C. Cantley, “Metabolic Flux and the Regulation of Mammalian Cell Growth,” *Cell Metab.*, vol. 14, no. 4, pp. 443–451, Oct. 2011.

[113] A. Walsh *et al.*, “Label-free Method for Classification of T cell Activation,” *bioRxiv*, p. 536813, Jan. 2019.

[114] M. Singh, J. Truong, W. B. Reeves, and J.-I. Hahm, “Emerging Cytokine Biosensors with Optical Detection Modalities and Nanomaterial-Enabled Signal Enhancement.,” *Sensors (Basel).*, vol. 17, no. 2, Feb. 2017.

[115] S. André, S. Lagresle, Z. Hannas, É. Calvosa, and L. Duponchel, “Mammalian cell culture monitoring using *in situ* spectroscopy: Is your method really optimised?,” *Biotechnol. Prog.*, vol. 33, no. 2, pp. 308–316, Mar. 2017.

[116] R. Luttmann *et al.*, “Soft sensors in bioprocessing: A status report and recommendations,” *Biotechnol. J.*, vol. 7, no. 8, pp. 1040–1048, Aug. 2012.

[117] A. Revzin, E. Maverakis, and H.-C. Chang, “Biosensors for immune cell analysis-A perspective.,” *Biomicrofluidics*, vol. 6, no. 2, pp. 21301–2130113, Jun. 2012.

[118] A. S. Rathore and H. Winkle, “Quality by design for biopharmaceuticals,” *Nat. Biotechnol.*, vol. 27, no. 1, pp. 26–34, Jan. 2009.

[119] M. A. Karimi *et al.*, “Measuring Cytotoxicity by Bioluminescence Imaging Outperforms the Standard Chromium-51 Release Assay,” *PLoS One*, vol. 9, no. 2, 2014.

[120] M. R. Verneris, M. Karami, J. Baker, A. Jayaswal, and R. S. Negrin, “Role of NKG2D

signaling in the cytotoxicity of activated and expanded CD8 T cells," *Blood*, vol. 103, no. 8, pp. 3065–3072, 2004.

[121] A. Rossignol, V. Bonnaudet, B. Clémenceau, H. Vié, and L. Bretaudeau, "A high-performance, non-radioactive potency assay for measuring cytotoxicity: A full substitute of the chromium-release assay targeting the regulatory-compliance objective," *MAbs*, vol. 9, no. 3, pp. 521–535, Apr. 2017.

[122] C. E. Brown *et al.*, "Biophotonic cytotoxicity assay for high-throughput screening of cytolytic killing," *J. Immunol. Methods*, vol. 297, pp. 39–52, 2005.

[123] R. Lichtenfels, W. E. Biddison, H. Schulz, A. B. Vogt, and R. Martin, "CARE-LASS (calcein-release-assay), an improved fluorescence-based test system to measure cytotoxic T lymphocyte activity," *J. Immunol. Methods*, vol. 172, pp. 227–239, 1994.

[124] K. Blomberg, C. Granberg, I. Hemmil~i, and T. Lovgren, "Europium-labelled target cells in an assay of natural killer cell activity II. A novel non-radioactive method based on time-resolved fluorescence. Significance and specificity of the method," *J. Immunol. Methods*, vol. 92, pp. 117–123, 1986.

[125] J. K. Peper, H. Schuster, M. W. Löffler, B. Schmid-Horch, H.-G. Rammensee, and S. Stevanović, "An impedance-based cytotoxicity assay for real-time and label-free assessment of T-cell-mediated killing of adherent cells," *J. Immunol. Methods*, vol. 405, pp. 192–198, Mar. 2014.

[126] D. Flieger, R. Gruber, G. Schlimok, C. Reiter, K. Pantel, and G. Riethmiiller, "A novel non-radioactive cellular cytotoxicity test based on the differential assessment of living and killed target and effector cells," *J. Immunol. Methods*, vol. 180, pp. 1–13, 1995.

[127] Y. Nakagawa, E. Watari, M. Shimizu, and H. Takahashi, "One-step simple assay to determine antigen-specific cytotoxic activities by single-color flow cytometry," *Biomed. Res.*, vol. 32, no. 2, pp. 159–166, 2011.

[128] R. C. Lynn *et al.*, "c-Jun overexpression in CAR T cells induces exhaustion resistance," *Nature*, vol. 576, 2019.

[129] D. T. Rodgers *et al.*, "Switch-mediated activation and retargeting of CAR-T cells for B-cell malignancies," 2015.

[130] E. Shifrut *et al.*, "Genome-wide CRISPR Screens in Primary Human T Cells Reveal Key Regulators of Immune Function," *Cell*, vol. 175, no. 7, pp. 1958-1971.e15, Dec. 2018.

[131] P. L. F. Johnson *et al.*, "Vaccination alters the balance between protective immunity, exhaustion, escape, and death in chronic infections.," *J. Virol.*, vol. 85, no. 11, pp. 5565–5570, 2011.

[132] A. Brú, S. Albertos, J. L. Subiza, J. Ló Pez García-Asenjo, and I. Brú, "The Universal Dynamics of Tumor Growth," 2003.

[133] T. Alarc, H. M. Byrne, and P. K. Maini, "A cellular automaton model for tumour growth in inhomogeneous environment," *J. Theor. Biol.*, vol. 225, pp. 257–274, 2003.

[134] T. Roose, S. J. Chapman, and P. K. Maini, “Mathematical Models of Avascular Tumor Growth *,” *Soc. Ind. Appl. Math.*, vol. 49, no. 2, pp. 179–208, 2007.

[135] F. Frascoli, P. S. Kim, B. D. Hughes, and K. A. Landman, “A dynamical model of tumour immunotherapy,” *Math. Biosci.*, vol. 253, pp. 50–62, 2014.

[136] D. Kirschner and J. C. Panetta, “Modeling immunotherapy of the tumor-immune interaction,” 1998.

[137] M. Pennisi, “A mathematical model of immune-system-melanoma competition,” *Comput. Math. Methods Med.*, vol. 2012, pp. 10–12, 2012.

[138] K. J. Mahasa, R. Ouifki, A. Eladdadi, and L. de Pillis, “Mathematical model of tumor–immune surveillance,” *J. Theor. Biol.*, vol. 404, pp. 312–330, Sep. 2016.

[139] L. G. de Pillis, A. E. Radunskaya, and C. L. Wiseman, “A validated mathematical model of cell-mediated immune response to tumor growth.,” *Cancer Res.*, vol. 65, no. 17, pp. 7950–8, Sep. 2005.

[140] A. A. Toor, A. Chesney, J. Zweit, J. Reed, and S. Hashmi, “A Dynamical Systems Perspective on Chimeric Antigen Receptor T-Cell Dosing,” *Bone Marrow Transpl.*, 2018.

[141] C. von Kalle, A. Deichmann, and M. Schmidt, “Vector Integration and Tumorigenesis,” *Hum. Gene Ther.*, vol. 25, no. 6, pp. 475–481, Jun. 2014.

[142] C.-Y. Wu, L. J. Rupp, K. T. Roybal, and W. a Lim, “Synthetic biology approaches to engineer T cells,” *Curr. Opin. Immunol.*, vol. 35, pp. 123–130, 2015.

[143] K. T. Roybal *et al.*, “Engineering T Cells with Customized Therapeutic Response Programs Using Synthetic Notch Receptors,” *Cell*, vol. 0, no. 0, Sep. 2016.

[144] A. H. Long *et al.*, “4-1BB costimulation ameliorates T cell exhaustion induced by tonic signaling of chimeric antigen receptors,” *Nat. Med.*, vol. 21, no. 6, pp. 581–90, 2015.

[145] D. L. Porter *et al.*, “Chimeric antigen receptor T cells persist and induce sustained remissions in relapsed refractory chronic lymphocytic leukemia[1] D. L. Porter, W.-T. Hwang, N. V. Frey, S. F. Lacey, P. A. Shaw, A. W. Loren, A. Bagg, K. T. Marcucci, A. Shen, V. Gonzalez, D.,” *Sci. Transl. Med.*, vol. 7, no. 303, Sep. 2015.

[146] D. Sommermeyer *et al.*, “Chimeric antigen receptor-modified T cells derived from defined CD8+ and CD4+ subsets confer superior antitumor reactivity in vivo,” *Leukemia*, vol. 30, no. 2, pp. 452–500, 2015.

[147] N. J. Piscopo *et al.*, “Bioengineering Solutions for Manufacturing Challenges in CAR T Cells,” *Biotechnol. J.*, vol. 13, no. 2, 2018.

[148] C. L. Nobles *et al.*, “CD19-targeting CAR T cell immunotherapy outcomes correlate with genomic modification by vector integration,” *J. Clin. Invest.*, vol. 130, no. 2, pp. 673–685, 2020.

[149] J. C. M. van der Loo and J. F. Wright, “Progress and challenges in viral vector manufacturing,” *Hum. Mol. Genet.*, vol. 25, no. R1, pp. R42–R52, 2016.

[150] J. B. Foster *et al.*, “Purification of mRNA Encoding Chimeric Antigen Receptor Is Critical for Generation of a Robust T-Cell Response,” *Hum. Gene Ther.*, vol. 30, no. 2, pp. 168–178, 2019.

[151] J. A. Fraietta *et al.*, “Determinants of response and resistance to CD19 chimeric antigen receptor (CAR) T cell therapy of chronic lymphocytic leukemia,” *Nat. Med.*, p. 1, Apr. 2018.

[152] R. A. Gardner *et al.*, “Intent-to-treat leukemia remission by CD19 CAR T cells of defined formulation and dose in children and young adults,” *Blood*, vol. 129, no. 25, pp. 3322–3331, 2017.

[153] J. Feucht *et al.*, “Calibration of CAR activation potential directs alternative T cell fates and therapeutic potency,” *Nat. Med.*, vol. 25, no. 1, pp. 82–88, Jan. 2019.

[154] M. Kalos, M. Kalos, B. L. Levine, D. L. Porter, S. Katz, and S. A. Grupp, “T Cells with Chimeric Antigen Receptors Have Potent Antitumor Effects and Can Establish Memory in Patients with Advanced Leukemia,” vol. 73, no. 95, 2011.

[155] Y. Xu *et al.*, “Closely related T-memory stem cells correlate with in vivo expansion of CAR.CD19-T cells and are preserved by IL-7 and IL-15,” *Blood*, vol. 123, no. 24, pp. 3750–3759, 2014.

[156] E. Zah *et al.*, “Systematically optimized BCMA/CS1 bispecific CAR-T cells robustly control heterogeneous multiple myeloma,” *Nat. Commun.*, vol. 11, no. 1, pp. 1–13, 2020.

[157] N. N. Shah and T. J. Fry, “Mechanisms of resistance to CAR T cell therapy,” *Nat. Rev. Clin. Oncol.*, vol. 16, no. 6, pp. 372–385, 2019.

[158] C. U. Louis *et al.*, “Antitumor activity and long-term fate of chimeric antigen receptor – positive T cells in patients with neuroblastoma,” *Mol. Ther. J. Am. Soc. Gene Ther.*, vol. 14, no. 11, pp. 1324–1334, 2011.

[159] B. D. Choi *et al.*, “CRISPR-Cas9 disruption of PD-1 enhances activity of universal EGFRvIII CAR T cells in a preclinical model of human glioblastoma,” *J. Immunother. Cancer*, vol. 7, no. 1, pp. 1–8, 2019.

[160] T. L. Roth *et al.*, “Pooled Knockin Targeting for Genome Engineering of Cellular Immunotherapies,” *Cell*, vol. 181, no. 3, pp. 728-744.e21, Apr. 2020.

[161] D. N. Nguyen *et al.*, “Polymer-stabilized Cas9 nanoparticles and modified repair templates increase genome editing efficiency,” *Nature Biotechnology*, vol. 38, no. 1. Nature Research, pp. 44–49, 01-Jan-2020.

[162] M. A. Pul??, K. C. Straathof, G. Dotti, H. E. Heslop, C. M. Rooney, and M. K. Brenner, “A chimeric T cell antigen receptor that augments cytokine release and supports clonal expansion of primary human T cells,” *Mol. Ther.*, vol. 12, no. 5, pp. 933–941, 2005.

[163] M. Goodwin *et al.*, “CRISPR-based gene editing enables FOXP3 gene repair in IPEX patient cells,” *Sci. Adv.*, vol. 6, no. 19, p. eaaz0571, May 2020.

[164] C. R. Lazzarotto *et al.*, “CHANGE-seq reveals genetic and epigenetic effects on CRISPR–

Cas9 genome-wide activity," *Nat. Biotechnol.*, 2020.

[165] K. Wang *et al.*, "A multiscale simulation framework for the manufacturing facility and supply chain of autologous cell therapies," *Cytotherapy*, vol. 21, no. 10, pp. 1081–1093, 2019.

[166] C. L. Hardee, L. M. Arévalo-Soliz, B. D. Hornstein, and L. Zechiedrich, "Advances in non-viral DNA vectors for gene therapy," *Genes*, vol. 8, no. 2. MDPI AG, p. 65, 01-Feb-2017.

[167] M. Ruella *et al.*, "Induction of resistance to chimeric antigen receptor T cell therapy by transduction of a single leukemic B cell," *Nat. Med.*, vol. 24, no. 10, pp. 1499–1503, Oct. 2018.

[168] K. Clement, J. Y. Hsu, M. C. Canver, J. K. Joung, and L. Pinello, "Technologies and Computational Analysis Strategies for CRISPR Applications," *Mol. Cell*, vol. 79, no. 1, pp. 11–29, 2020.

[169] C. A. Vakulskas *et al.*, "A high-fidelity Cas9 mutant delivered as a ribonucleoprotein complex enables efficient gene editing in human hematopoietic stem and progenitor cells," *Nat. Med.*, vol. 24, no. 8, pp. 1216–1224, Aug. 2018.

[170] A. Costantini *et al.*, "Effects of cryopreservation on lymphocyte immunophenotype and function," *J. Immunol. Methods*, vol. 278, no. 1–2, pp. 145–155, 2003.

[171] A. Subramanian *et al.*, "Gene set enrichment analysis: A knowledge-based approach for interpreting genome-wide expression profiles," *Proc. Natl. Acad. Sci. U. S. A.*, vol. 102, no. 43, pp. 15545–15550, 2005.

[172] H. J. Stauss, E. C. Morris, and H. Abken, "Cancer gene therapy with T cell receptors and chimeric antigen receptors," *Curr. Opin. Pharmacol.*, vol. 24, pp. 113–118, 2015.

[173] S. L. Maude *et al.*, "Chimeric Antigen Receptor T Cells for Sustained Remissions in Leukemia," *N. Engl. J. Med.*, vol. 371, no. 16, pp. 1507–1517, Oct. 2014.

[174] D. M. Barrett, "Improving CAR T cell immunotherapy–mediated remissions for pediatric leukemia," *Journal of Clinical Investigation*, vol. 129, no. 5. American Society for Clinical Investigation, pp. 1842–1844, 01-May-2019.

[175] S. Depil, P. Duchateau, S. A. Grupp, G. Mufti, and L. Poirot, "'Off-the-shelf' allogeneic CAR T cells: development and challenges," *Nature Reviews Drug Discovery*, vol. 19, no. 3. Nature Research, pp. 185–199, 01-Mar-2020.

[176] A. M. Stein *et al.*, "Tisagenlecleucel Model-Based Cellular Kinetic Analysis of Chimeric Antigen Receptor–T Cells," *CPT Pharmacometrics Syst. Pharmacol.*, vol. 8, no. 5, pp. 285–295, May 2019.

[177] K. T. Mueller *et al.*, "Cellular kinetics of CTL019 in relapsed/refractory B-cell acute lymphoblastic leukemia and chronic lymphocytic leukemia," *Blood*, vol. 130, no. 21, pp. 2317–2325, Nov. 2017.

[178] K. T. Mueller *et al.*, "Clinical Pharmacology of Tisagenlecleucel in B-cell Acute

Lymphoblastic Leukemia," *Clin. Cancer Res.*, vol. 24, no. 24, pp. 6175–6184, Dec. 2018.

[179] K. A. Hay *et al.*, "Kinetics and biomarkers of severe cytokine release syndrome after CD19 chimeric antigen receptor–modified T-cell therapy," *Blood*, vol. 130, no. 21, pp. 2295–2306, Nov. 2017.

[180] R. Awasthi *et al.*, "Tisagenlecleucel cellular kinetics, dose, and immunogenicity in relation to clinical factors in relapsed/refractory DLBCL," *Blood Adv.*, vol. 4, no. 3, pp. 560–572, Feb. 2020.

[181] J. M. Ayuso *et al.*, "Evaluating natural killer cell cytotoxicity against solid tumors using a microfluidic model," *Oncoimmunology*, vol. 8, no. 3, Mar. 2019.

[182] K. Guldevall *et al.*, "Microchip screening platform for single cell assessment of NK cell cytotoxicity," *Front. Immunol.*, vol. 7, no. APR, Apr. 2016.

[183] A. Murschhauser *et al.*, "A high-throughput microscopy method for single-cell analysis of event-time correlations in nanoparticle-induced cell death."

[184] Mohamad Hamieh1 *et al.*, "CAR T cell trogocytosis and cooperative killing regulate tumour antigen escape," *Nature*, vol. 568, no. April, p. 112, 2019.

[185] S. Hong, Q. Pan, and L. P. Lee, "Single-cell level co-culture platform for intercellular communication," *Integr. Biol.*, vol. 4, no. 4, pp. 374–380, Apr. 2012.

[186] K. Guldevall *et al.*, "Imaging Immune Surveillance of Individual Natural Killer Cells Confined in Microwell Arrays," *PLoS One*, vol. 5, no. 11, p. e15453, Nov. 2010.

[187] Y. S. Schiffenbauer *et al.*, "A cell chip for sequential imaging of individual non-adherent live cells reveals transients and oscillations," *Lab Chip*, vol. 9, no. 20, pp. 2965–2972, 2009.

[188] N. A. Zumwalde, E. Domae, M. F. Mescher, and Y. Shimizu, "ICAM-1–Dependent Homotypic Aggregates Regulate CD8 T Cell Effector Function and Differentiation during T Cell Activation," *J. Immunol.*, vol. 191, no. 7, pp. 3681–3693, Oct. 2013.

[189] A. Wolfe, B. O'Clair, V. E. Groppi, and D. P. McEwen, "Pharmacologic characterization of a kinetic in vitro human co-culture angiogenesis model using clinically relevant compounds," *J. Biomol. Screen.*, vol. 18, no. 10, pp. 1234–1245, Dec. 2013.

[190] F. Fasbender and C. Watzl, "Impedance-based analysis of Natural Killer cell stimulation," *Sci. Rep.*, vol. 8, no. 1, pp. 1–9, Dec. 2018.

[191] P. Sahoo *et al.*, "Mathematical deconvolution of CAR T-cell proliferation and exhaustion from real-time killing assay data," *J. R. Soc. Interface*, vol. 17, no. 162, Jan. 2020.

[192] I. Liadi *et al.*, "Individual Motile CD4(+) T Cells Can Participate in Efficient Multikilling through Conjugation to Multiple Tumor Cells.," *Cancer Immunol. Res.*, vol. 3, no. 5, pp. 473–82, 2015.

[193] I. Liadi, J. Roszik, G. Romain, L. J. N. Cooper, and N. Varadarajan, "Quantitative high-throughput single-cell cytotoxicity assay for T cells.," *J. Vis. Exp.*, no. 72, p. e50058, 2013.

[194] K. Molugu *et al.*, “Tracking and Predicting Human Somatic Cell Reprogramming Using Nuclear Characteristics,” *Biophys. J.*, vol. 118, no. 9, pp. 2086–2102, May 2020.

[195] K. Owens and I. Bozic, “MODELLING CAR T-CELL THERAPY WITH PATIENT PRECONDITIONING,” *bioRxiv*, p. 2020.06.20.162925, Jun. 2020.

[196] K. Shankar, C. M. Capitini, C. M. Capitini, K. Saha, K. Saha, and K. Saha, “Genome engineering of induced pluripotent stem cells to manufacture natural killer cell therapies,” *Stem Cell Research and Therapy*, vol. 11, no. 1. BioMed Central Ltd., pp. 1–14, 16-Jun-2020.

[197] M. E. Smerchansky and M. A. Kinney, “Engineered multicellular niches for pluripotent stem cell-derived immunotherapy,” *Curr. Opin. Biomed. Eng.*, Jun. 2020.

[198] D. C. Duffy, J. C. Mcdonald, O. J. A. Schueller, and G. M. Whitesides, “Rapid Prototyping of Microfluidic Systems in Poly(dimethylsiloxane),” *Anal. Chem.*, vol. 70, pp. 4974–4984, 1998.

[199] C. L. Bonifant, H. J. Jackson, R. J. Brentjens, and K. J. Curran, “Toxicity and management in CAR T-cell therapy.,” *Mol. Ther. oncolytics*, vol. 3, p. 16011, 2016.

[200] A. Di Stasi *et al.*, “Inducible Apoptosis as a Safety Switch for Adoptive Cell Therapy,” *N. Engl. J. Med.*, vol. 365, no. 18, pp. 1673–1683, 2011.

[201] C.-Y. Wu, K. T. Roybal, E. M. Puchner, J. Onuffer, and W. A. Lim, “Remote control of therapeutic T cells through a small molecule-gated chimeric receptor.,” *Science*, vol. 350, no. 6258, p. aab4077, Oct. 2015.

[202] J. A. Fraietta *et al.*, “Disruption of TET2 promotes the therapeutic efficacy of CD19-targeted T cells,” 2018.

[203] M. P. Schwartz *et al.*, “Human pluripotent stem cell-derived neural constructs for predicting neural toxicity,” *Proc. Natl. Acad. Sci.*, vol. 112, no. 40, pp. 12516–12521, Oct. 2015.

[204] L. J. Rupp *et al.*, “CRISPR/Cas9-mediated PD-1 disruption enhances anti-tumor efficacy of human chimeric antigen receptor T cells.,” *Sci. Rep.*, vol. 7, no. 1, p. 737, Apr. 2017.

[205] “Cellectis Submits IND Application for UCART123, an Allogeneic Gene Edited CAR T-Cell Product Candidate, in AML and BPDCN | Cellectis,” 2017. .

[206] W. A. Lim and C. H. June, “The Principles of Engineering Immune Cells to Treat Cancer,” *Cell*, vol. 168, no. 4, pp. 724–740, Feb. 2017.

[207] C. C. Kloss, M. Condomines, M. Cartellieri, M. Bachmann, and M. Sadelain, “Combinatorial antigen recognition with balanced signaling promotes selective tumor eradication by engineered T cells,” *Nat. Biotechnol.*, vol. 31, no. 1, pp. 71–75, Jan. 2013.

[208] V. D. Fedorov, M. Themeli, and M. Sadelain, “PD-1- and CTLA-4-based inhibitory chimeric antigen receptors (iCARs) divert off-target immunotherapy responses.,” *Sci. Transl. Med.*, vol. 5, no. 215, p. 215ra172, Dec. 2013.

[209] E. Zah, M.-Y. Lin, A. Silva-Benedict, M. C. Jensen, and Y. Y. Chen, “T Cells Expressing

CD19/CD20 Bispecific Chimeric Antigen Receptors Prevent Antigen Escape by Malignant B Cells.," *Cancer Immunol. Res.*, vol. 4, no. 6, pp. 498–508, 2016.

[210] J. B. Black *et al.*, "Targeted Epigenetic Remodeling of Endogenous Loci by CRISPR/Cas9-Based Transcriptional Activators Directly Converts Fibroblasts to Neuronal Cells," *Cell Stem Cell*, vol. 19, no. 3, pp. 406–414, Sep. 2016.

[211] L. S. Qi *et al.*, "Repurposing CRISPR as an RNA-Guided Platform for Sequence-Specific Control of Gene Expression," *Cell*, vol. 152, no. 5, pp. 1173–1183, Feb. 2013.

[212] P. Mali *et al.*, "CAS9 transcriptional activators for target specificity screening and paired nickases for cooperative genome engineering," *Nat. Biotechnol.*, vol. 31, no. 9, pp. 833–838, Aug. 2013.

[213] T. S. Klann *et al.*, "CRISPR–Cas9 epigenome editing enables high-throughput screening for functional regulatory elements in the human genome," *Nat. Biotechnol.*, Apr. 2017.

[214] R. G. Mannino *et al.*, "'Do-it-yourself in vitro vasculature that recapitulates in vivo geometries for investigating endothelial-blood cell interactions,'" *Sci. Rep.*, vol. 5, no. 1, p. 12401, Dec. 2015.

[215] M. Themeli, I. Rivière, and M. Sadelain, "New Cell Sources for T Cell Engineering and Adoptive Immunotherapy," *Cell Stem Cell*, vol. 16, no. 4, pp. 357–366, 2015.

[216] C. Morrison, "$1-million price tag set for Glybera gene therapy," *Nat. Biotechnol.*, vol. 33, no. 3, pp. 217–218, Mar. 2015.

[217] M. Keshavan, "Cancer therapy holds great promise — but at great cost," 2016. [Online]. Available: https://www.statnews.com/2016/08/23/cancer-car-t-side-effects/. [Accessed: 01-May-2017].

[218] J. Ren, X. Liu, C. Fang, S. Jiang, C. H. June, and Y. Zhao, "Multiplex Genome Editing to Generate Universal CAR T Cells Resistant to PD1 Inhibition," *Clin. Cancer Res.*, vol. 23, no. 9, pp. 2255–2266, May 2017.

[219] T. T. Smith *et al.*, "In situ programming of leukaemia-specific T cells using synthetic DNA nanocarriers," *Nat. Nanotechnol.*, vol. advance on, Apr. 2017.

[220] J. A. Zuris *et al.*, "Cationic lipid-mediated delivery of proteins enables efficient protein-based genome editing in vitro and in vivo," *Nat. Biotechnol.*, vol. 33, no. 1, pp. 73–80, Jan. 2015.

[221] E. Cameau, A. Pedregal, and C. Glover, "Cost modelling comparison of adherent multi-trays with suspension and fixed-bed bioreactors for the manufacturing of gene therapy products," *Cell Gene Ther. Insights*, vol. 5, no. 11, pp. 1663–1674, 2019.

APPENDICES

Appendix A: Supplemental Tables and Figures for Chapter 2

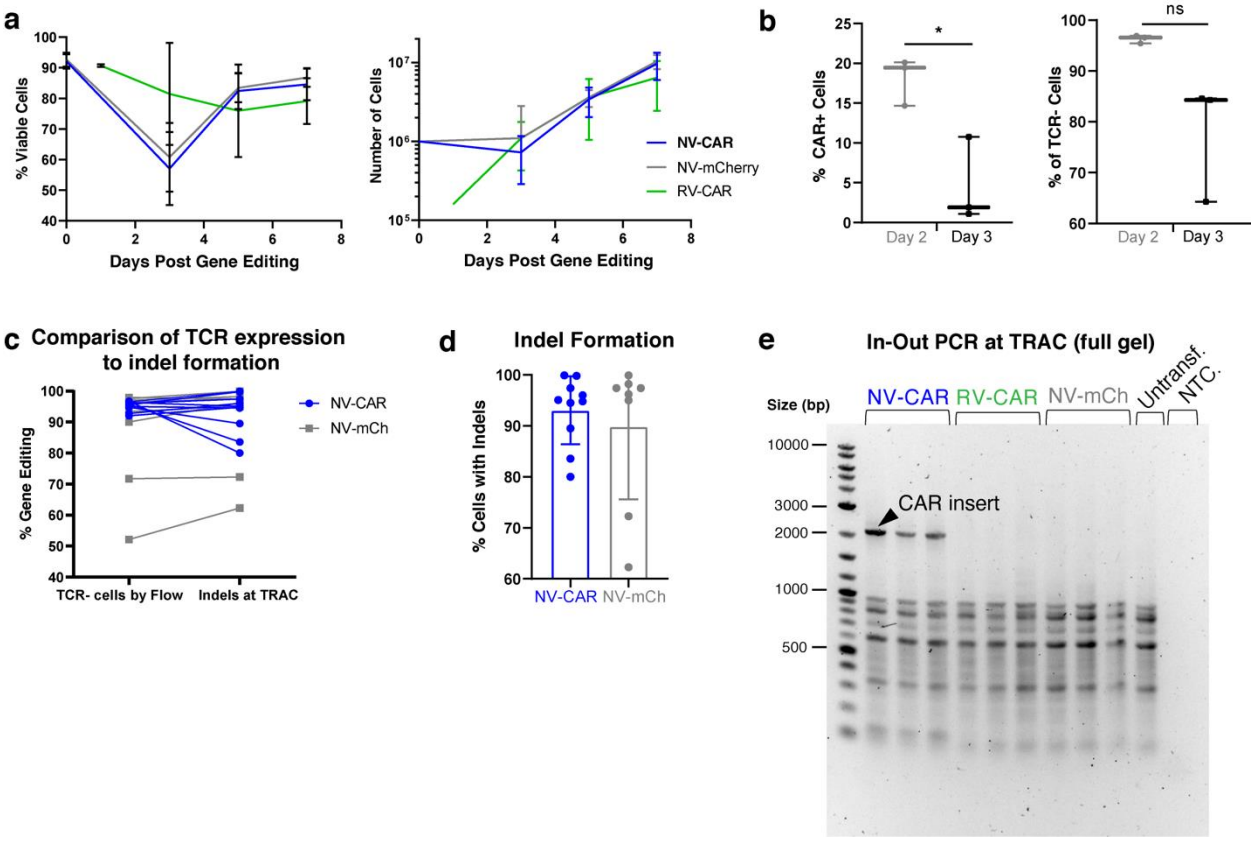

Figure A-1

Pre-antigen exposure characterization of NV-CAR T cells. a, Left, viability of cells throughout the manufacturing timeline, pooled for all 4 donors. Right, cell counts throughout the manufacture calendar, pooled for all 4 donors. NV-CAR (blue) N=36; RV-CAR (green) N=27; NV-mCh (gray) N=25. **b, Left**, Percent of CAR+ cells as measured by flow cytometry when electroporated on day 2 or day 3 post-isolation. **Right,** Percent of cells with TCR knockout as measured by flow cytometry when electroporated on day 2 or day 3 post-isolation. All groups, N=3. **c,** Level of TCR disruption in NV-CAR and NV-mCh T cells measured by both TCR surface expression by flow cytometry (right) and presence of indels at the *TRAC* locus (left). NV-CAR (blue) N=10, NV-mCh (grey) N=8. **d,** Percent of cells with indels at the TRAC locus in both NV-CAR and NV-mCh conditions. NV-CAR (blue) N=10; NV-mCh (grey) N=8, both for one donor. **e,** In-out PCR confirming NV-CAR insertion, full gel from **Fig. 1g** shown. PCR was optimized to minimize off-target amplification which occurs only for fragments <1 kb across the genome. N=3 for all samples from one donor. Untransf., donor matched untransfected control T cells; NTC = non-template control.

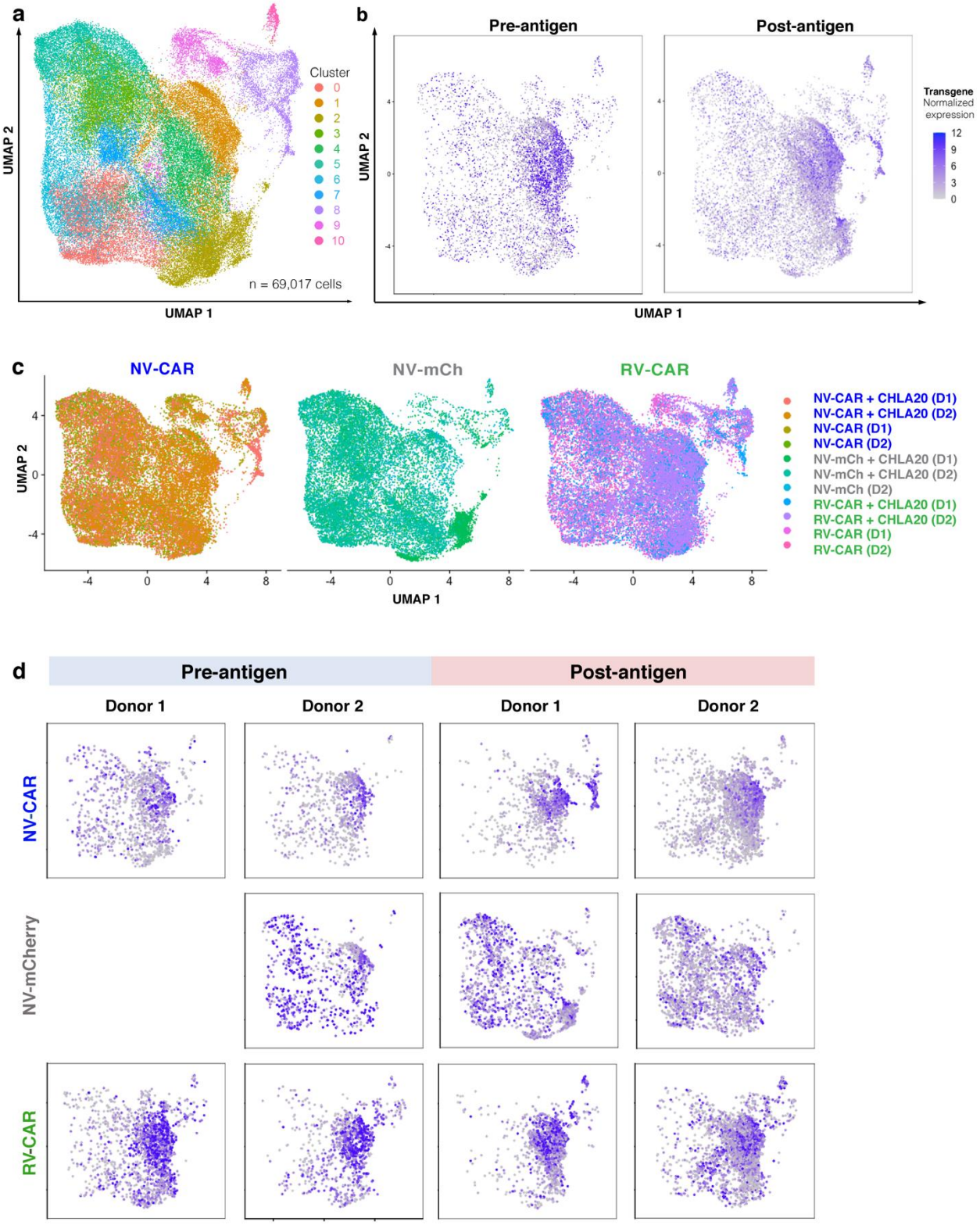
a
b
Pre-antigen
Post-antigen
Cluster
0
1
2
3
4
5
6
7
8
9
10
n = 69,017 cells
UMAP 1
UMAP 2
Transgene
Normalized expression
12
9
6
3
0
c
NV-CAR
NV-mCh
RV-CAR
NV-CAR + CHLA20 (D1)
NV-CAR + CHLA20 (D2)
NV-CAR (D1)
NV-CAR (D2)
NV-mCh + CHLA20 (D1)
NV-mCh + CHLA20 (D2)
NV-mCh (D2)
RV-CAR + CHLA20 (D1)
RV-CAR + CHLA20 (D2)
RV-CAR (D1)
RV-CAR (D2)
d
Pre-antigen
Post-antigen
Donor 1
Donor 2
Donor 1
Donor 2
NV-CAR
NV-mCherry
RV-CAR

Figure A-2

Single cell transcriptomic characterization across eleven samples shows distinct transcriptional signatures associated with CAR expression but not mCherry expression, both before and after antigen exposure. **a,** UMAP projection of single cell RNA-seq data showing cells across all eleven samples and two donors, both pre-and post-antigen exposure. N=69,017 single cells. **b**, UMAP projection as in **a**, separated to show clustering of transgene positive cells prior to antigen exposure (left) and after 24 hours of *in vitro* exposure to GD2+ CHLA20 neuroblastoma. **c**, UMAP projection as in **a**, separated to show clustering of cells by sample. None of the samples segregated into any particular area of the UMAP projection, indicating that batch effects are not of significant concern. D1 = donor 1, D2 = donor 2. **d,** UMAP projection as in **a**, showing transgene positive cells for each individual sample. CAR-positive cells from NV-CAR and RV-CAR groups consistently cluster regardless of the presence of GD2 antigen, while NV-mCh cells do not, suggesting a distinct transcriptional profile associated with CAR signaling.

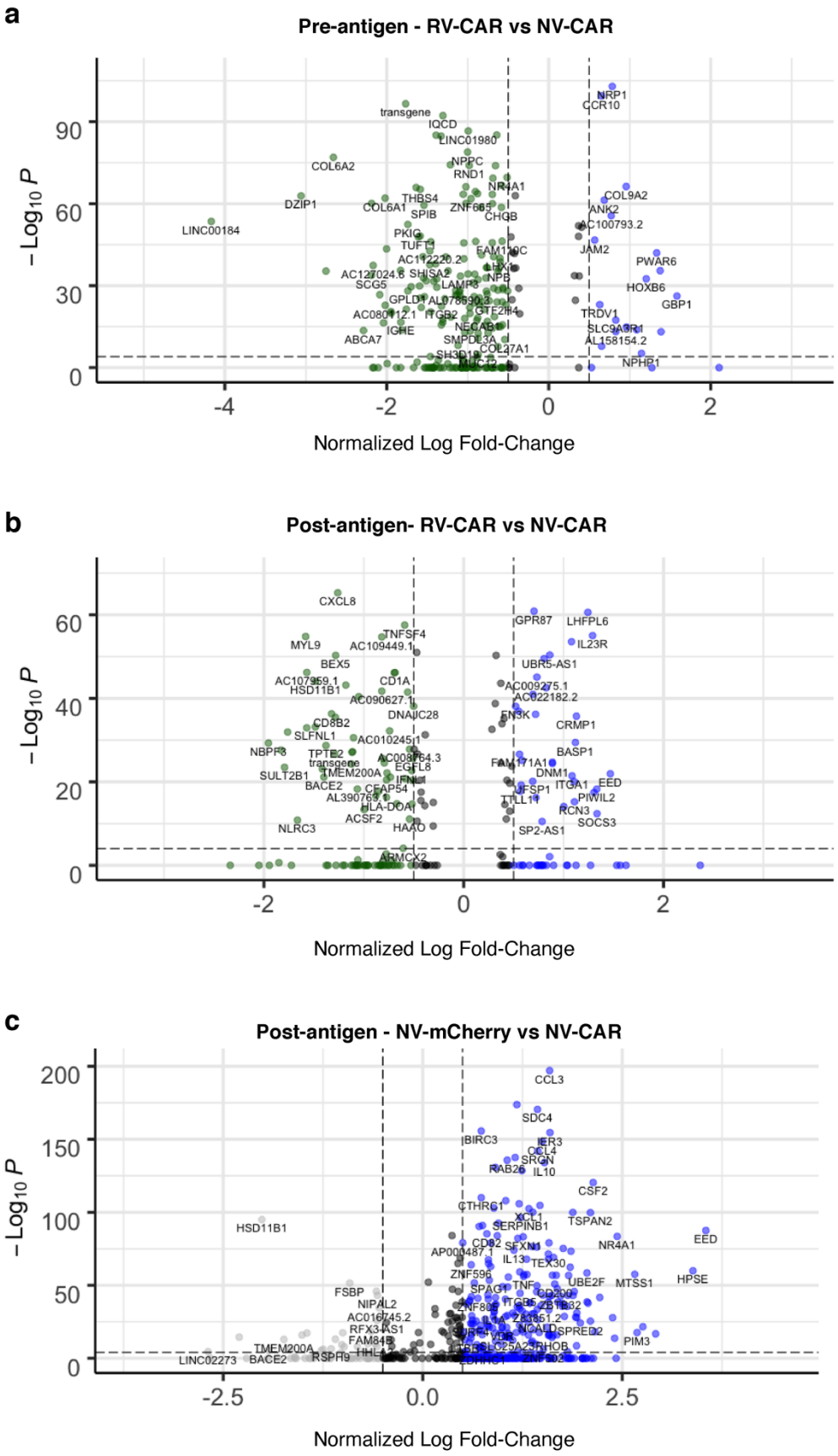
a
Pre-antigen - RV-CAR vs NV-CAR
– Log10 P
Normalized Log Fold-Change
b
Post-antigen- RV-CAR vs NV-CAR
– Log10 P
Normalized Log Fold-Change
c
Post-antigen - NV-mCherry vs NV-CAR
– Log10 P
Normalized Log Fold-Change

Figure A-3

scRNA-seq indicates unique transcriptional profiles associated with transgene-positive cells within NV-CAR and RV-CAR T cell products before antigen exposure, as well as CAR-signaling associated genes after target antigen exposure. a-c, Volcano plot for genes that showed significant differential expression ($p<0.001$) for transgene-positive cells from two donors for three comparison groups: RV-CAR/NV-CAR pre-antigen (**a**), RV-CAR/NV-CAR post-antigen exposure (**b**), and NV-mCh/NV-CAR post-antigen (**c**). Post-antigen exposure refers to 24 hours co-culture with GD2+ CHLA20 neuroblastoma. Named genes showed normalized log fold-change over 0.5 and $p<10e-5$. For a and b, genes shown in green (left) are upregulated in RV-CAR T cells; genes shown in blue (right) are upregulated in NV-CAR T cells. For c, genes shown in grey (left) are upregulated in NV-mCh T cells after antigen exposure; genes shown in blue (right) are upregulated in NV-CAR T cells. N=2 donors for all plots; full list of differential genes shown in **Supplementary Table 2.**

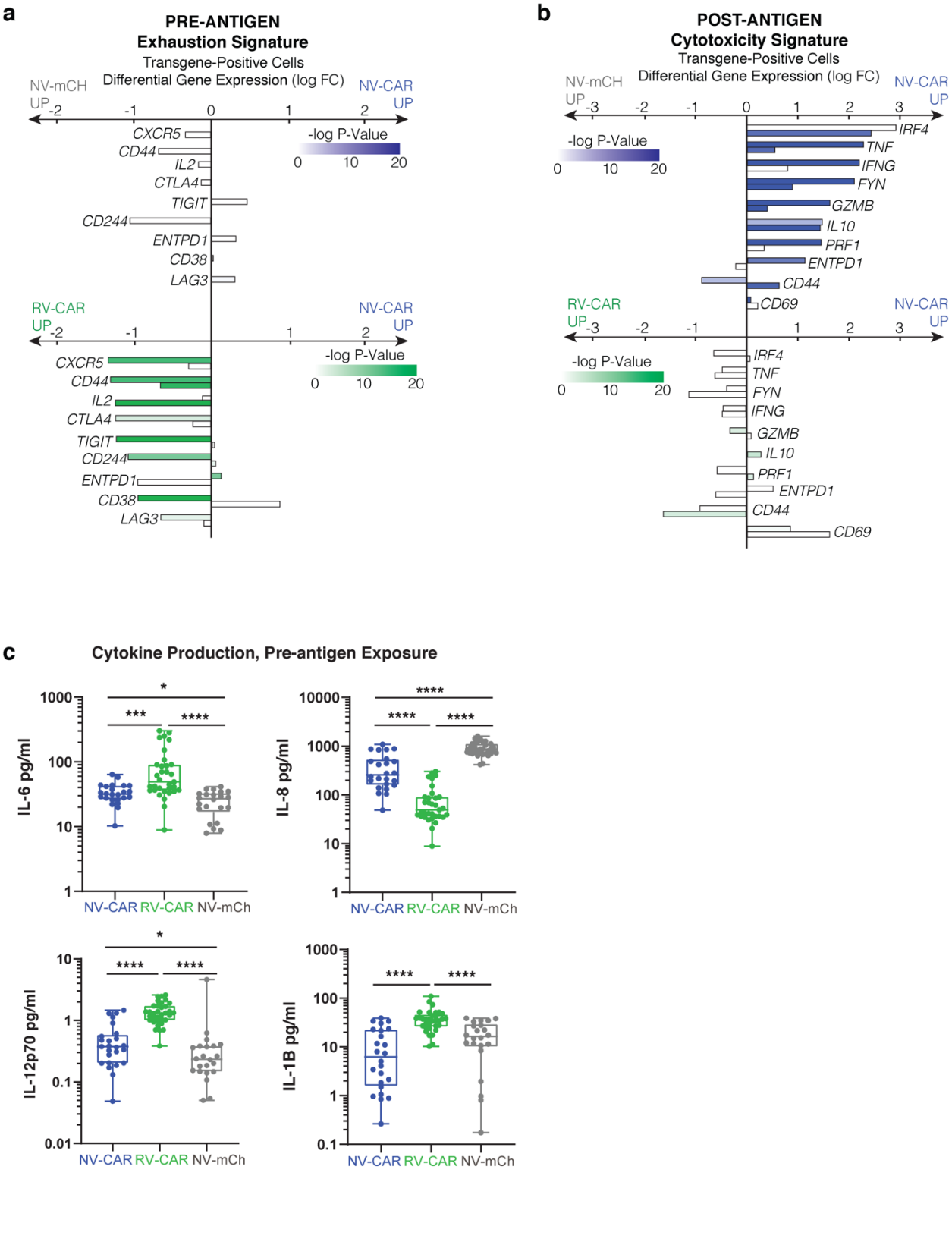
a
PRE-ANTIGEN
Exhaustion Signature
Transgene-Positive Cells
Differential Gene Expression (log FC)
NV-mCH UP
NV-CAR UP
-log P-Value
CXCR5
CD44
IL2
CTLA4
TIGIT
CD244
ENTPD1
CD38
LAG3
RV-CAR UP
NV-CAR UP
b
POST-ANTIGEN
Cytotoxicity Signature
Transgene-Positive Cells
Differential Gene Expression (log FC)
NV-mCH UP
NV-CAR UP
RV-CAR UP
NV-CAR UP
IRF4
TNF
IFNG
FYN
GZMB
IL10
PRF1
ENTPD1
CD44
CD69
c
Cytokine Production, Pre-antigen Exposure
IL-6 pg/ml
IL-8 pg/ml
IL-12p70 pg/ml
IL-1B pg/ml
NV-CAR
RV-CAR
NV-mCh

Figure A-4

NV-CAR T cells show less exhaustion and less cytokine production prior to antigen exposure, suggesting decreased tonic signaling. a Prior to antigen exposure, NV-CAR and NV-mCh T cells show minimal significant differences in expression of exhaustion related genes (**top**), while RV-CAR T cells upregulate exhaustion signature relative to NV-CAR T cells (**bottom). b**, post-antigen exposure, NV-CAR T cells significantly upregulate cytotoxicity signature relative to NV-mCh T cells (**top**), but show minimal differences in cytotoxicity relative to RV-CAR T cells (**bottom**). Top bar for each gene is for donor 1, bottom bar is for donor 2; color scales indicate adjusted P values with Bonferroni correction. **c,** Cytokine production values pre-antigen exposure. Values are pooled from all 4 donors. NV-CAR (blue) N=24; RV-CAR (green) N=33; NV-mCh (gray) N=22. * indicates p<=0.05; ** indicates p<=0.01; *** indicates p<=0.001; **** indicates p<=0.0001.

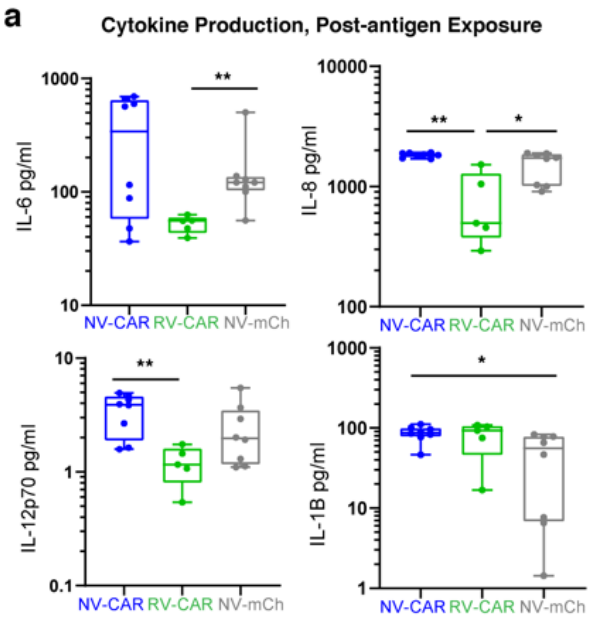
a
Cytokine Production, Post-antigen Exposure
IL-6 pg/ml
IL-8 pg/ml
IL-12p70 pg/ml
IL-1B pg/ml
NV-CAR RV-CAR NV-mCh

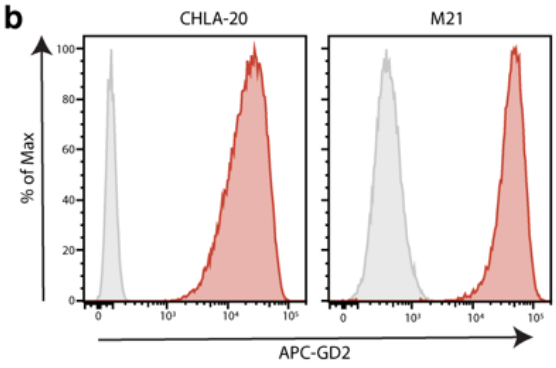
b
CHLA-20
M21
% of Max
APC-GD2

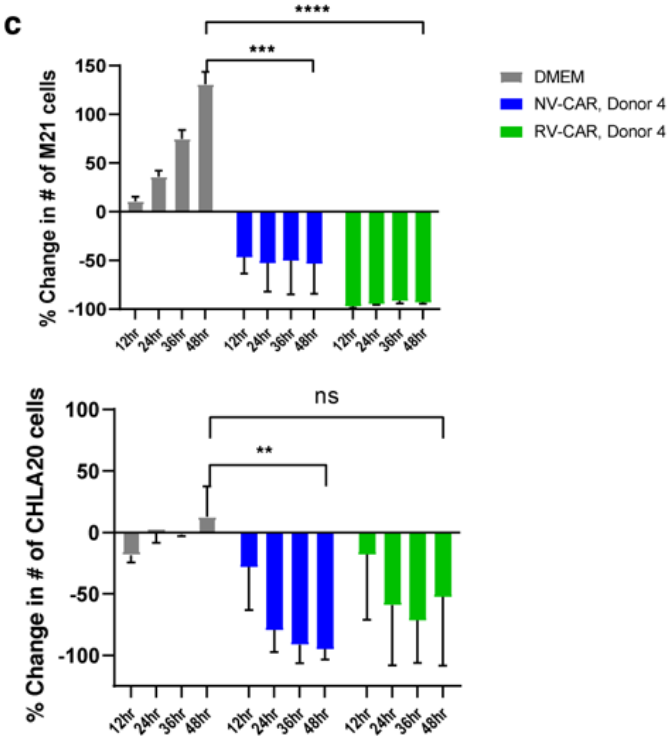
c
DMEM
NV-CAR, Donor 4
RV-CAR, Donor 4
% Change in # of M21 cells
% Change in # of CHLA20 cells
ns
12hr 24hr 36hr 48hr

Figure A-5

Post-antigen exposure characterization of manufactured CAR T cell products. a, Cytokine production after 24 h co-culture with the target antigen. Values are pooled from 2 donors. NV-CAR (blue) N=8; RV-CAR (green) N=5; NV-mCh (gray) N=8. **b,** Flow cytometry histograms show the levels of GD2 on M21 and CHLA20 cell lines (red) compared to isotype controls (grey). **c,** Graphs show the cytotoxic action of NV-CAR and RV-CAR T cells against two GD2-positive tumor cell lines, CHLA20 and M21, containing a stably integrated fluorescent transgene (AkaLuc-GFP and H2B-mCherry, respectively). Cytotoxicity measured by change number of mCherry-positive objects for each image. *indicates p<=0.05; ** indicates p<=0.01; *** indicates p<=0.001; **** indicates p<=0.0001.

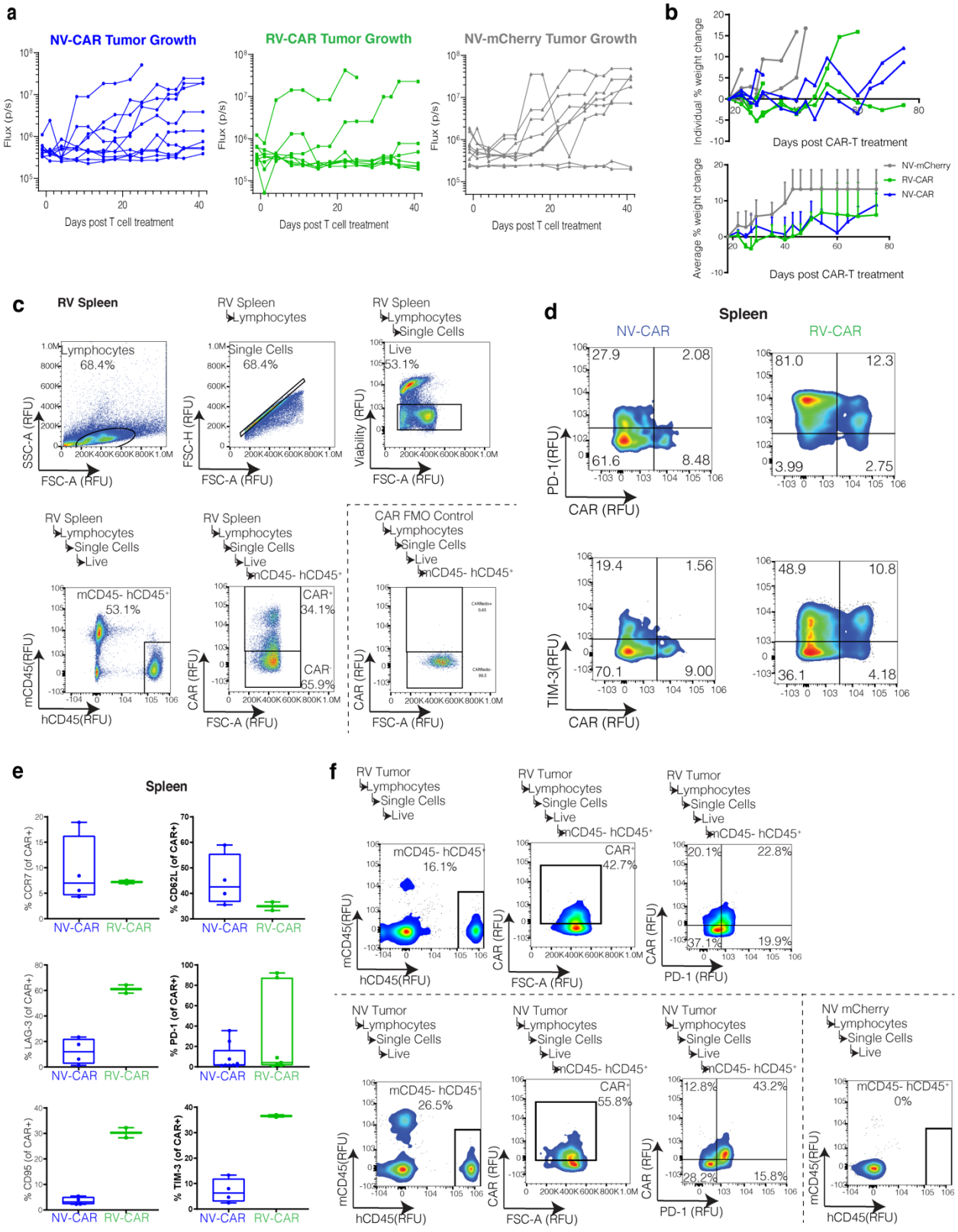
a
NV-CAR Tumor Growth
RV-CAR Tumor Growth
NV-mCherry Tumor Growth
Flux (p/s)
Days post T cell treatment
b
Individual % weight change
Average % weight change
Days post CAR-T treatment
NV-mCherry
RV-CAR
NV-CAR
c
RV Spleen
Lymphocytes
Single Cells
Live
mCD45- hCD45+
CAR FMO Control
SSC-A (RFU)
FSC-A (RFU)
FSC-H (RFU)
Viability (RFU)
mCD45(RFU)
hCD45(RFU)
CAR (RFU)
d
Spleen
NV-CAR
RV-CAR
PD-1(RFU)
TIM-3(RFU)
e
Spleen
% CCR7 (of CAR+)
% CD62L (of CAR+)
% LAG-3 (of CAR+)
% PD-1 (of CAR+)
% CD95 (of CAR+)
% TIM-3 (of CAR+)
f
RV Tumor
NV Tumor
NV mCherry
PD-1 (RFU)

Figure A-6

Bioluminescence, tumor growth, weight gains, and T cell persistence and exhaustion after T cell treatment *in vivo*. a, Flux measurements for individual luciferase-positive tumors for all mouse experiments. NV-CAR, N=10. RV-CAR, N=8. NV-mCh, N=7. **b, Top**, individual mouse percent weight change throughout the experiment. **Bottom**, average percent weight change in mice per treatment condition. **c,** Flow cytometric gating strategy used to assay mouse spleens for human T cells and CAR-positive cells. **d,** Flow cytometric plots for PD-1 or TIM-3 expression on the y-axis and CAR expression on the x-axis for human CD45-positive cells in the spleen. **e,** Boxplots showing the expression levels of subtype and exhaustion markers on human T cells found in mouse spleens. **f,** Flow cytometric plots detailing hCD45-positive cells, followed by PD-1-positive and CAR-positive cells, found in mouse tumors that did not regress.

Table A-1

Modifications of off-target sites of the *TRAC* genome editing strategy detected by CHANGE-seq. Target sequence for all analysis was CAGGGTTCTGGATATCTGTNGG. Only top 50 loci with the highest Nuclease Read Counts are included.

Chrom-osome	Start	End	Genomic Coordinate	Nuclease Read Count	Strand	Control Read Count	Site_Sequence	Site Substitution Number	Site_Sequence Gaps_Allowed	Full_Name	Realigned_Target Sequence
chr14	22547498	22547520	chr14:22547498-22547520	2174	-	0	CAGGGTTCTG GATATCTGTGGG	0		None_None_chr14: 22547498-22547520_2174	none
chr17	40703372	40703394	chr17:40703372-40703394	852	-	0			CAGGGGTTCTG GAT-TCTGTGGG	None_None_chr17: 40703372-40703394_852	CAGGG-TCTGG ATATCTGTNGG
chr11	112561336	112561358	chr11:112561336-112561358	824	+	0	AAGGGCTCTGG ACATCTGTTGG	3		None_None_chr11: 112561336-112561358_824	none
chr20	32791382	32791404	chr20:32791382-32791404	794	+	0	CAAGGTTCTGG ATATCTGTGTG	2		None_None_chr20: 32791382-32791404_794	none
chr5	62938742	62938764	chr5:62938742-62938764	716	-	0	TAGGGTTATGA AAATCTGTGGG	4		None_None_chr5: 62938742-62938764_716	none
chr12	76904355	76904377	chr12:76904355-76904377	700	-	0	ATGGGTTCTAG ACATCTGTGGG	4		None_None_chr12:76904355-76904377_700	none
chr3	39224133	39224154	chr3:39224133-39224154	644	-	0			GAGGGTTCTG GAT-TCTGTGGG	None_None_chr3:39224133-39224154_644	CAGGGTTCTGG ATATCTGTNGG
chr12	122528644	122528666	chr12:122528644-122528666	622	-	0	CTAGGGTTTTG GTATCTGTGGG	6	TAGGGTTTTGG -TATCTGTGGG	None_None_chr12:122528644-122528666_622	CAGGGTTCTGG ATATCTGTNGG
chr8	18531360	18531381	chr8:18531360-18531381	584	+	0			GTGGGTTCTGG ATA-CTGTAGG	None_None_chr8:18531360-18531381_584	CAGGGTTCTGG ATATCTGTNGG
chr1	186351297	186351319	chr1:186351297-186351319	552	-	0	CAGAGTTCTGA ATTTCTGTAGG	3		None_None_chr1:186351297-186351319_552	none
chr8	65468682	65468704	chr8:65468682-65468704	484	-	0	CAAGGATTCTG GTATCTGTTGG	6	AAGGATTCTGG -TATCTGTTGG	None_None_chr8:65468682-65468704_484	CAGGGTTCTGG ATATCTGTNGG
chr18	28607973	28607995	chr18:28607973-28607995	482	-	0	AGGGGTTCTGT ATATCTGTTGG	3	CAGGGGTTCTG TATATCTGTTGG	None_None_chr18:28607973-28607995_482	CAGGG-TCTGG ATATCTGTNGG
chr3	193489265	193489286	chr3:193489265-193489286	482	-	0			CAGGTTTCTAGA TA-CTGTTGG	None_None_chr3:193489265-193489286_482	CAGGGTTCTGG ATATCTGTNGG
chr18	10474286	10474309	chr18:10474286-10474309	458	-	0			CAGGTTTCTGGA TTATCTGTGGG	None_None_chr18:10474286-10474309_458	CAGGGTTCTGGAT-ATCTGTNGG
chr1	161549761	161549783	chr1:161549761-161549783	412	-	0	TAGGGCTCCGG ATATCTTTGGT	5	TAGGGCTCCGGA TATCT-TTGG	None_None_chr1:161549761-161549783_412	CAGGGTTCTGGA TATCTGTNGG
chr2	175733717	175733739	chr2:175733717-175733739	408	-	0	GAGGGATCTGG ATATCTTGGGT	5	GAGGGATCTGGA TATCT-TGGG	None_None_chr2:175733717-175733739_408	CAGGGTTCTGG ATATCTGTNGG
chr1	161631119	161631141	chr1:161631119-161631141	390	-	0	TAGGGCTCCGG ATATCTTTGGT	5	TAGGGCTCCGGA TATCT-TTGG	None_None_chr1:161631119-161631141_390	CAGGGTTCTGG ATATCTGTNGG
chr12	109514437	109514459	chr12:109514437-109514459	360	-	0	CAGGGCTCTG GATTTCTATGGG	3		None_None_chr12:109514437-109514459_360	none
chr1	12357332	12357354	chr1:12357332-12357354	340	+	0	GAGAGTTCTG GATATTGTAGGG	6	GAGAGTTCTGGA TAT-TGTAGG	None_None_chr1:12357332-12357354_340	CAGGGTTCTGG ATATCTGTNGG
chr20	24956213	24956235	chr20:24956213-24956235	310	-	0	CTGGGTCCTG GATGTCTGTGGG	3		None_None_chr20:24956213-24956235_310	none
chr3	15513808	15513830	chr3:15513808-15513830	306	-	0	TCAGGATCTGG ATATCTGTGGG	4	CAGGAT-CTGGA TATCTGTGGG	None_None_chr3:15513808-15513830_306	CAGGGTTCTGG ATATCTGTNGG
chr2	217291117	217291139	chr2:217291117-217291139	284	-	0	ATAGGTTCTGG ATATCTGTGGC	4	TAGG-TTCTGGA TATCTGTGGC	None_None_chr2:217291117-217291139_284	CAGGGTTCTGG ATATCTGTNGG
chr7	126078952	126078974	chr7:126078952-126078974	276	+	0	CAGGAGTCTGA ATATCTGTGGG	3		None_None_chr7:126078952-126078974_276	none
chr2	178315502	178315525	chr2:178315502-178315525	270	-	0			CTGGGTTCTGAA TCATCTGTGGG	None_None_chr2:178315502-178315525_270	CAGGGTTCTGGAT-ATCTGTNGG
chr16	30506705	30506727	chr16:30506705-30506727	260	-	0	CAGGGCTCTGG ATCTGTGGGGG	4		None_None_chr16:30506705-30506727_260	none
chr3	43100427	43100448	chr3:43100427-43100448	232	+	0			TTGGATTCTGG-TATCTGTGGG	None_None_chr3:43100427-43100448_232	CAGGGTTCTGG ATATCTGTNGG
chr1	246685165	246685187	chr1:246685165-246685187	214	-	0	AAGGGTACTAG ATATCTGGGGT	5	AAGGGTACTAG ATATCTG-GGG	None_None_chr1:246685165-246685187_214	CAGGGTTCTGG ATATCTGTNGG
chr8	33915372	33915394	chr8:33915372-33915394	210	-	0	CAGGATTCTAA ATATCTGCAGG	4		None_None_chr8:33915372-33915394_210	none
chr1	23492555	23492577	chr1:23492555-23492577	198	-	0	TGGCCATGTGG ATATCTGTGGG	6		None_None_chr1:23492555-23492577_198	none
chr3	15302244	15302265	chr3:15302244-15302265	198	+	0			CAGGGTGCTGG A-ATCTGTGGG	None_None_chr3:15302244-15302265_198	CAGGGTTCTGG ATATCTGTNGG
chr2	30196507	30196529	chr2:30196507-30196529	194	-	0	CTAGGACATGG ATATCTGTGGG	5		None_None_chr2:30196507-30196529_194	none
chr1	80461528	80461550	chr1:80461528-80461550	172	-	0	TGGGGTTCTAA ATATATGTTGG	5		None_None_chr1:80461528-80461550_172	none
chr4	2702596	2702618	chr4:2702596-2702618	160	-	0	GTGGGGCTGG GATATCTGTGGG	6		None_None_chr4:2702596-2702618_160	none
chr7	129650785	129650807	chr7:129650785-129650807	156	+	0	AGGGGTTCTGG ATATCTTGGTG	5	CAGGGGTTCTGG ATATCTTGGTG	None_None_chr7:129650785-129650807_156	CAGGG-TCTGG ATATCTGTNGG
chr17	45045090	45045112	chr17:45045090-45045112	148	+	0	TAGGTATCTAG ATATCTATAGG	5		None_None_chr17:45045090-45045112_148	none
chr4	12900184	12900206	chr4:12900184-12900206	144	-	0	AAGGGTTAAAG CTATCTGTGGG	5		None_None_chr4:12900184-12900206_144	none
chr4	20834353	20834375	chr4:20834353-20834375	142	+	0	CAGGGTACTGG GTATATGTGGG	3		None_None_chr4:20834353-20834375_142	none
chr4	99579491	99579513	chr4:99579491-99579513	142	-	0	GAGCTACATGG ATATCTGTGGG	6		None_None_chr4:99579491-99579513_142	none
chr11	97219436	97219458	chr11:97219436-97219458	138	+	0	ATGGGGGTTGG ATATCTGCAGG	6		None_None_chr11:97219436-97219458_138	none
chr2	48154595	48154617	chr2:48154595-48154617	138	+	0	ATGGGTCCTTG ATATCTGTTAG	5	CATGGGTCCTT GATATCTGTTAG	None_None_chr2:48154595-48154617_138	CA-GGTTCTGG ATATCTGTNGG
chr11	33910938	33910960	chr11:33910938-33910960	136	-	0	TGGGGGTCTGG ATATCTGTCAG	4		None_None_chr11:33910938-33910960_136	none
chr19	1512262	1512284	chr19:1512262-1512284	128	+	0	TAGGGTCCTGG GTATCTCTAGG	4		None_None_chr19:1512262-1512284_128	none
chr7	63140834	63140856	chr7:63140834-63140856	122	-	0	CAGGGTTCTGG AATTGTGGGTG	5		None_None_chr7:63140834-63140856_122	none
chr11	133323102	133323124	chr11:133323102-133323124	120	+	0	CAGGGATCTGG ATACCTGTGGT	3		None_None_chr11:133323102-133323124_120	none
chr4	156773119	156773141	chr4:156773119-156773141	120	+	0	GAGGGATATGG ATATCTTTTGG	4		None_None_chr4:156773119-156773141_120	none
chr8	60788756	60788778	chr8:60788756-60788778	118	+	0	AAGGGTACTGG ATATCTTGGTG	5	AAGGGTACTGG ATATCT-TGGT	None_None_chr8:60788756-60788778_118	CAGGGTTCTGG ATATCTGTNGG
chr13	34289967	34289989	chr13:34289967-34289989	116	+	0	CAGGGCTCTAA ATATCTGCTAG	5	CAGGGCTCTAA ATATCTGCTAGG	None_None_chr13:34289967-34289989_116	CAGGGTTCTGG ATATCTG-TNGG
chr17	19838074	19838096	chr17:19838074-19838096	114	-	0	GAGCCATGTGG ATATCTGTGGG	5		None_None_chr17:19838074-19838096_114	none
chr1	222622374	222622396	chr1:222622374-222622396	114	+	0	AAGGGTCCTCG ATATCTTTAGG	4		None_None_chr1:222622374-222622396_114	none
chr14	65614837	65614859	chr14:65614837-65614859	112	+	0	TTAGGTTATGG ATATCTTTGGG	5	TAGG-TTATGGA TATCTTTGGG	None_None_chr14:65614837-65614859_112	CAGGGTTCTGG ATATCTGTNGG

Table A-2

Supplementary Table 2. Differentially expressed genes between sample pairs. Comparison for NV-CAR/RV-CAR donor-matched pairs, pre- and post-antigen exposure. Unless otherwise indicated, genes listed had significant differential expression ($p<0.001$) for both donors; values in the table show normalized log fold-change and adjusted P-values for all cells pooled across both donors.

NV vs RV Pre Antigen Exposure						NV vs RV Post Antigen Exposure					
GeneName	**p_val**	**avg_logFC**	**pct.1**	**pct.2**	**p_val_adj**	**GeneName**	**p_val**	**avg_logFC**	**pct.1**	**pct.2**	**p_val_adj**
NRP1	7.38E-108	0.783707232	0.421	0.171	1.17E-103	**CXCL8**	3.38E-70	-1.260447119	0.502	0.36	5.35E-66
CCR10	2.32E-104	0.650313438	0.196	0.121	3.68E-100	**GPR87**	8.41E-66	0.703608119	0.339	0.27	1.33E-61
transgene	1.81E-101	-1.766497665	1	1	2.87E-97	**LHFPL6**	1.63E-65	1.242707167	0.381	0.302	2.59E-61
IQCD	3.79E-97	-1.306498648	0.288	0.103	6.01E-93	**TNFSF4**	1.78E-62	-0.590777895	0.334	0.267	2.82E-58
LINC01980	1.65E-91	-0.993477977	0.285	0.093	2.61E-87	**IL23R**	5.57E-60	1.290808487	0.362	0.279	8.83E-56
IRX3	4.43E-90	-0.642217693	0.358	0.161	7.02E-86	**MYL9**	9.29E-60	-1.582029053	0.348	0.287	1.47E-55
ART3	5.34E-90	-1.391053685	0.234	0.097	8.46E-86	**AC109449.1**	1.21E-59	-0.819358086	0.158	0.12	1.93E-55
PHEX	1.21E-89	-1.329478212	0.3	0.123	1.92E-85	**OBSL1**	1.65E-58	1.079433258	0.28	0.205	2.61E-54
NPPC	8.27E-84	-1.001706299	0.323	0.13	1.31E-79	**DLG3-AS1**	6.58E-56	-0.469639247	0.223	0.144	1.04E-51
COL6A2	7.33E-82	-2.660146384	0.237	0.095	1.16E-77	**UBR5-AS1**	2.64E-55	0.861959408	0.32	0.235	4.19E-51
ENC1	3.75E-79	-1.214223881	0.226	0.119	5.94E-75	**BEX5**	3.11E-55	-1.282228127	0.299	0.251	4.93E-51
RND1	6.39E-79	-0.982496804	0.282	0.106	1.01E-74	**KIRREL2**	3.17E-55	0.323749653	0.18	0.137	5.02E-51
NTRK1	7.63E-79	-0.658394365	0.295	0.102	1.21E-74	**EVA1A**	1.97E-54	0.804044542	0.141	0.128	3.12E-50
NR4A1	1.50E-74	-0.516079979	0.328	0.142	2.38E-70	**AC107959.1**	3.90E-51	-1.569805985	0.262	0.159	6.19E-47
AC234772.3	2.88E-74	-0.688882838	0.31	0.108	4.57E-70	**CD1A**	4.14E-51	-0.687586298	0.193	0.152	6.56E-47
CABLES1	1.37E-71	-0.580453519	0.283	0.138	2.16E-67	**PLEKHH2**	4.83E-51	-0.694073776	0.352	0.277	7.65E-47
COL9A2	3.24E-71	0.955042312	0.301	0.153	5.14E-67	**AC009275.1**	4.93E-50	0.732820006	0.369	0.278	7.81E-46
AC012184.1	4.18E-71	-1.023717176	0.267	0.084	6.63E-67	**HSD11B1**	5.31E-49	-1.482299236	0.203	0.182	8.42E-45
CTHRC1	7.38E-71	-1.63807408	0.392	0.212	1.17E-66	**ADGRE2**	1.49E-48	0.371244262	0.352	0.293	2.36E-44
THBS4	3.48E-70	-1.587664985	0.267	0.1	5.52E-66	**AL445472.1**	4.22E-48	-1.180391598	0.194	0.154	6.69E-44
P2RY14	2.38E-69	-0.905625149	0.341	0.212	3.77E-65	**AC022182.2**	1.86E-47	0.826209565	0.251	0.193	2.94E-43
IL22	1.27E-68	-0.879791558	0.207	0.086	2.01E-64	**AC090627.1**	1.16E-46	-0.8191522	0.189	0.126	1.83E-42
CHRNA6	2.26E-68	-1.056078435	0.198	0.101	3.58E-64	**AC009630.2**	2.02E-46	-0.561222808	0.369	0.279	3.20E-42
AC067930.4	2.41E-68	-0.6959323	0.233	0.077	3.83E-64	**LINC00599**	7.10E-46	0.692738501	0.122	0.136	1.13E-41
MYL9	7.26E-68	-0.413343476	0.261	0.161	1.15E-63	**TNIP3**	2.37E-45	-1.050812781	0.251	0.283	3.75E-41
DZIP1	8.63E-68	-3.058389298	0.188	0.057	1.37E-63	**TM4SF5**	1.09E-43	0.315298732	0.233	0.142	1.73E-39
COL6A1	6.08E-67	-2.021156682	0.183	0.068	9.63E-63	**DNAJC28**	4.75E-43	-0.500924953	0.12	0.12	7.54E-39
ZNF665	9.12E-67	-0.959792182	0.251	0.064	1.45E-62	**FN3K**	5.07E-43	0.51987206	0.206	0.131	8.03E-39
ANK2	2.99E-66	0.685744721	0.24	0.083	4.74E-62	**ALPK1**	7.65E-42	0.551499905	0.174	0.142	1.21E-37
LAIR2	5.16E-65	-1.023024297	0.331	0.143	8.19E-61	**CD8B2**	3.19E-41	-1.322139966	0.231	0.165	5.06E-37
AC005224.4	5.43E-65	-2.189014544	0.319	0.126	8.61E-61	**EFCAB10**	4.30E-41	0.720173464	0.266	0.165	6.82E-37

MILR1	6.40E-65	-0.694549371	0.309	0.116	1.01E-60	**CRMP1**	1.19E-40	1.127870407	0.195	0.13	1.88E-36
SPIB	2.35E-64	-1.540399752	0.193	0.068	3.72E-60	**TSPAN10**	2.14E-40	-1.284818507	0.266	0.161	3.40E-36
ALPK3	1.38E-63	-0.836821864	0.218	0.079	2.19E-59	**MERTK**	4.19E-40	0.403890995	0.204	0.219	6.65E-36
CHGB	1.43E-63	-0.585384793	0.266	0.08	2.26E-59	**PROS1**	7.30E-39	0.382734693	0.429	0.344	1.16E-34
AC100793.2	1.66E-60	0.77195384	0.242	0.103	2.63E-56	**SLFNL1**	4.26E-38	-1.485474637	0.222	0.172	6.75E-34
LINC00184	2.03E-58	-4.167618843	0.154	0.021	3.22E-54	**ANXA3**	7.33E-38	-1.570697401	0.317	0.27	1.16E-33
PKIG	2.35E-57	-1.740920623	0.284	0.136	3.72E-53	**SPIB**	1.69E-37	0.283149411	0.268	0.196	2.67E-33
CBS	7.36E-57	0.369382187	0.185	0.05	1.17E-52	**AC010245.1**	3.70E-37	-0.742388231	0.291	0.213	5.87E-33
NBPF20	2.86E-56	0.405120948	0.278	0.103	4.54E-52	**CYP2W1**	7.18E-37	-1.76183074	0.151	0.125	1.14E-32
SH3D21	4.04E-53	-1.58875588	0.325	0.141	6.40E-49	**TRAV29DV5**	3.47E-36	-0.384869321	0.162	0.148	5.50E-32
NRIP3	5.66E-53	0.36869308	0.243	0.114	8.97E-49	**AREG**	1.64E-35	-1.103428628	0.189	0.21	2.60E-31
TRAV1-2	9.26E-53	-0.466868034	0.242	0.053	1.47E-48	**BASP1**	2.41E-34	1.117175989	0.153	0.172	3.81E-30
TUFT1	9.53E-53	-1.609281774	0.27	0.082	1.51E-48	**NBPF3**	3.22E-34	-1.954366417	0.148	0.174	5.11E-30
JAM2	1.41E-51	0.56684328	0.266	0.083	2.23E-47	**TPTE2**	1.22E-33	-1.378401269	0.179	0.17	1.94E-29
FAM110C	3.28E-51	-0.577221547	0.208	0.062	5.20E-47	**AC008764.3**	9.93E-33	-0.542338703	0.224	0.188	1.57E-28
TMTC2	3.97E-51	-0.902471617	0.262	0.105	6.30E-47	**NT5E**	9.94E-33	-0.496105389	0.325	0.26	1.58E-28
ALOX5AP	5.01E-51	-1.455963793	0.385	0.262	7.94E-47	**G0S2**	1.71E-32	-1.827390062	0.524	0.41	2.71E-28
ZNF772	1.17E-50	-0.696785526	0.222	0.092	1.86E-46	**PAN3-AS1**	3.55E-32	-1.113149864	0.347	0.253	5.63E-28
TSPAN18	1.42E-50	-1.04942631	0.132	0.032	2.26E-46	**PLAC8**	5.17E-32	-1.117547612	0.116	0.138	8.20E-28
ITGB7	2.08E-48	-2.002578912	0.379	0.27	3.29E-44	**transgene**	1.27E-31	-1.291807881	1	1	2.02E-27
AC112220.2	1.30E-47	-1.469099561	0.231	0.073	2.07E-43	**PRAM1**	1.38E-31	-0.461094177	0.122	0.111	2.19E-27
CHIT1	4.64E-47	-0.447549121	0.293	0.097	7.35E-43	**FAM171A1**	1.52E-31	0.558232888	0.155	0.104	2.41E-27
PWAR6	6.55E-47	1.331942127	0.268	0.113	1.04E-42	**EGFL8**	1.51E-30	-0.506192816	0.222	0.203	2.40E-26
NR4A2	9.56E-47	-0.422625244	0.234	0.105	1.52E-42	**MT1G**	1.51E-30	-0.810386177	0.31	0.289	2.40E-26
RAB31	3.61E-46	-0.829533817	0.184	0.067	5.73E-42	**SLC27A1**	4.49E-30	0.584067104	0.264	0.218	7.11E-26
PI16	1.65E-45	-0.679818897	0.246	0.162	2.61E-41	**CCR8**	1.27E-29	0.887884921	0.375	0.316	2.02E-25
AL445248.1	1.70E-45	-1.552736139	0.312	0.123	2.69E-41	**ZSCAN9**	1.90E-29	-0.795260429	0.33	0.271	3.01E-25
ALDH8A1	2.01E-45	-1.271514835	0.214	0.085	3.19E-41	**ADAP2**	1.91E-29	0.370537692	0.21	0.161	3.03E-25
LHX1	5.50E-45	-0.603001746	0.261	0.109	8.73E-41	**DNM1**	2.54E-29	0.887778659	0.155	0.183	4.02E-25
LY6G5B	9.16E-45	-1.048664664	0.282	0.102	1.45E-40	**TMEM200A**	3.55E-29	-1.124217499	0.272	0.219	5.63E-25
AC004832.6	1.37E-43	-0.599557211	0.241	0.062	2.17E-39	**FRMD4A**	1.13E-28	0.480888869	0.205	0.239	1.79E-24
PTGES3L	7.50E-43	-1.396865044	0.176	0.042	1.19E-38	**SULT2B1**	2.02E-28	-1.794178378	0.162	0.109	3.21E-24
SHISA2	1.37E-42	-1.469438424	0.308	0.109	2.17E-38	**C11orf44**	5.17E-28	-1.415690155	0.16	0.123	8.20E-24
AC127024.6	2.48E-42	-2.168541452	0.255	0.072	3.93E-38	**IFNL1**	1.26E-27	-0.519193872	0.225	0.179	1.99E-23
CRTAM	1.53E-41	-0.768653606	0.32	0.235	2.43E-37	**CHMP4C**	4.52E-27	-0.766679329	0.142	0.166	7.17E-23
AL391988.1	1.69E-41	-0.756534585	0.258	0.087	2.68E-37	**EED**	7.09E-27	1.468545904	0.618	0.729	1.12E-22
AC141586.3	2.10E-41	-0.408561452	0.225	0.054	3.33E-37	**ITGA1**	2.29E-26	1.08442271	0.211	0.203	3.64E-22
CTAGE6	3.28E-41	-0.433775685	0.18	0.045	5.20E-37	**BACE2**	4.50E-26	-1.399885626	0.196	0.169	7.14E-22
NPB	3.38E-41	-0.614040063	0.188	0.041	5.36E-37	**KCNE1**	4.89E-26	-0.733714683	0.173	0.103	7.75E-22
ENPP1	1.72E-40	-1.830247274	0.16	0.05	2.72E-36	**REM2**	1.04E-25	-0.58556203	0.17	0.125	1.64E-21

PTGFRN	2.10E-40	1.37647958	0.356	0.222	3.34E-36	**CFAP54**	2.03E-25	-0.772245176	0.13	0.162	3.21E-21
CD44	2.66E-40	-1.24285473	0.393	0.267	4.22E-36	**NIPAL2**	2.41E-25	-0.436772704	0.264	0.241	3.82E-21
AC002480.2	2.94E-40	-2.750455614	0.156	0.074	4.66E-36	**BCL6**	2.44E-25	0.432225634	0.181	0.226	3.87E-21
C4orf50	3.41E-40	-0.629082658	0.187	0.034	5.40E-36	**AC068722.2**	2.64E-25	-0.514963794	0.184	0.148	4.18E-21
AC136944.2	3.46E-39	-0.995634243	0.236	0.062	5.48E-35	**UFSP1**	4.73E-25	0.689979751	0.213	0.224	7.49E-21
AC130324.2	3.99E-39	-0.913273811	0.196	0.031	6.32E-35	**MAPRE3**	5.14E-25	1.105414054	0.241	0.184	8.15E-21
SCG5	1.10E-38	-2.190495234	0.301	0.108	1.74E-34	**AC018521.2**	1.41E-24	0.460450056	0.179	0.119	2.23E-20
MEOX1	1.46E-38	0.318307214	0.174	0.068	2.32E-34	**AC093157.2**	3.66E-24	0.574693898	0.241	0.187	5.81E-20
LINC02068	2.05E-38	0.376880264	0.229	0.082	3.24E-34	**AL390763.1**	3.31E-23	-1.064243072	0.16	0.13	5.25E-19
LAMP3	2.20E-38	-1.090105742	0.209	0.052	3.49E-34	**PIWIL2**	3.49E-23	1.331971114	0.253	0.241	5.53E-19
AL359715.1	8.78E-38	-0.7768936	0.168	0.043	1.39E-33	**TTLL11**	1.12E-22	0.566730962	0.264	0.229	1.78E-18
SPIRE2	9.34E-38	-1.546792201	0.204	0.069	1.48E-33	**RSPH9**	1.13E-22	-0.850024599	0.136	0.074	1.78E-18
HOXB6	1.88E-37	1.203706839	0.29	0.096	2.98E-33	**ATP12A**	1.78E-22	-0.42677884	0.29	0.252	2.83E-18
C20orf194	2.09E-37	-1.383325871	0.286	0.147	3.31E-33	**C1QL1**	2.14E-22	1.303742032	0.202	0.166	3.39E-18
AL158071.5	3.87E-37	-0.872648908	0.189	0.054	6.13E-33	**AC137630.3**	1.34E-21	-0.87836874	0.203	0.185	2.13E-17
LINC01597	1.07E-36	-1.513228856	0.214	0.078	1.69E-32	**HLA-DOA**	3.31E-21	-0.772962348	0.232	0.214	5.24E-17
GAD1	1.63E-36	-1.420426271	0.225	0.185	2.59E-32	**TMEM136**	3.79E-21	0.723434658	0.309	0.291	6.00E-17
ANGPTL2	6.24E-36	-0.936254926	0.141	0.025	9.89E-32	**PKD2L2**	1.82E-20	-0.429235845	0.298	0.23	2.88E-16
NBPF15	8.18E-35	-1.594937895	0.261	0.151	1.30E-30	**RCN3**	3.68E-20	1.108969603	0.279	0.222	5.84E-16
AOC3	1.57E-34	-1.699068844	0.18	0.072	2.50E-30	**AC020656.2**	5.42E-20	-0.304924597	0.145	0.102	8.60E-16
SPRY3	2.58E-34	-1.382051652	0.221	0.069	4.08E-30	**TRBV20-1**	1.15E-19	-0.669733052	0.152	0.109	1.82E-15
PART1	3.72E-34	-0.565571391	0.198	0.048	5.89E-30	**COX6B2**	1.39E-19	-0.516552993	0.255	0.191	2.20E-15
AFF2	5.98E-34	-0.369711051	0.135	0.03	9.47E-30	**LINC00504**	1.77E-19	0.412429748	0.267	0.227	2.80E-15
CDH26	6.24E-34	-0.67875999	0.162	0.053	9.90E-30	**AC060766.4**	3.15E-19	-0.388718383	0.249	0.194	5.00E-15
AF129075.2	1.54E-33	-0.564667442	0.187	0.042	2.44E-29	**SCN2A**	5.01E-19	1.001468919	0.149	0.166	7.94E-15
AC079385.2	2.60E-33	-0.627599931	0.154	0.048	4.11E-29	**ACSF2**	2.66E-18	-0.996720275	0.264	0.263	4.21E-14
MYO1F	2.90E-33	-1.095500945	0.348	0.242	4.59E-29	**CDC20B**	7.13E-18	0.460380081	0.18	0.124	1.13E-13
SIPA1L2	4.05E-33	-1.148340241	0.199	0.059	6.42E-29	**SOCS3**	2.56E-17	1.334913489	0.248	0.227	4.06E-13
GPLD1	5.13E-33	-1.740532507	0.195	0.068	8.13E-29	**AC110615.1**	4.97E-16	0.426505911	0.113	0.193	7.88E-12
AC009950.1	5.53E-33	-0.507853943	0.218	0.05	8.77E-29	**HAAO**	5.18E-16	-0.542979274	0.168	0.197	8.21E-12
AC093525.6	6.73E-33	-0.769051652	0.204	0.061	1.07E-28	**NLRC3**	9.08E-16	-1.664975671	0.292	0.237	1.44E-11
AL078590.3	1.59E-32	-1.105094352	0.312	0.233	2.52E-28	**LINC01934**	1.64E-15	-0.465887782	0.149	0.148	2.61E-11
AC087632.1	8.51E-32	-0.75950128	0.158	0.051	1.35E-27	**SP2-AS1**	1.89E-15	0.785585021	0.201	0.183	3.00E-11
IFI6	1.30E-31	-2.086725809	0.386	0.272	2.06E-27	**STEAP1B**	2.31E-14	-0.305812166	0.126	0.112	3.66E-10
PITPNM2	1.93E-31	-1.149171678	0.218	0.117	3.07E-27	**ARMCX2**	4.90E-09	-0.605865843	0.228	0.295	7.77E-05
AC007216.4	2.23E-31	-1.13114115	0.211	0.062	3.53E-27	**LINC00880**	1.08E-07	-0.775774037	0.184	0.231	0.001720046
SLC35G2	2.58E-31	-1.095534134	0.323	0.143	4.08E-27	**CACNB2**	1.58E-07	0.366252426	0.258	0.209	0.002503545
GBP1	3.85E-31	1.583113038	0.26	0.172	6.10E-27	**AC084809.2**	5.12E-07	0.860562114	0.154	0.18	0.008114647
ARL4C	5.90E-31	-0.921378512	0.364	0.247	9.35E-27	**SPATA45**	5.37E-07	0.389531687	0.201	0.257	0.008513126
SYCE1L	6.72E-31	-1.534067431	0.231	0.083	1.06E-26	**LINC00910**	2.95E-06	-0.794167014	0.188	0.181	0.046789998

ITGAX	1.68E-30	-0.855858756	0.379	0.28	2.67E-26	**LINC02273**	3.01E-06	-1.058937291	0.137	0.128	0.047676908
AP002852.1	2.20E-30	-1.587878097	0.401	0.27	3.49E-26	**TREML2**	4.29E-06	-0.717225741	0.17	0.146	0.068073474
B2M	3.67E-30	-1.284518802	0.303	0.221	5.82E-26	**C11orf95**	1.40E-05	-1.850331065	0.238	0.25	0.222417075
AHNAK	5.88E-30	-1.051811056	0.379	0.272	9.32E-26	**SPATA3-AS1**	0.015854584	0.450646866	0.18	0.16	1
OGDHL	9.38E-30	-0.453309667	0.117	0.054	1.49E-25	**NAPSA**	0.01563233	0.899962061	0.266	0.23	1
S100A11	1.49E-29	0.328207856	0.402	0.273	2.37E-25	**ASMT**	0.00371791	1.12389625	0.213	0.2	1
C11orf44	2.26E-29	-0.734967982	0.123	0.035	3.59E-25	**AC096734.1**	0.037947703	0.371117266	0.095	0.149	1
PLOD2	4.85E-29	-0.821963966	0.257	0.172	7.68E-25	**Z94721.1**	0.905612527	0.797912283	0.209	0.214	1
PRRX2	5.21E-29	-0.574600968	0.212	0.087	8.26E-25	**AC234582.1**	0.282593084	0.587217441	0.231	0.201	1
GTF2H4	6.07E-29	-0.639717674	0.268	0.131	9.62E-25	**AC026333.4**	0.331471366	1.040009309	0.252	0.29	1
SLC39A5	1.34E-28	-0.916144697	0.171	0.06	2.12E-24	**HIST1H2AK**	0.000462075	1.566540883	0.243	0.22	1
TRDV1	5.72E-28	0.629549815	0.247	0.071	9.07E-24	**CEBPD**	0.200755722	0.775576944	0.164	0.187	1
AC022784.3	6.84E-28	-0.528328506	0.125	0.055	1.08E-23	**AC103724.4**	0.013234588	0.391479773	0.169	0.149	1
CD52	7.09E-28	-0.854698736	0.315	0.222	1.12E-23	**NAP1L2**	0.080169596	0.739738407	0.235	0.283	1
AC080112.1	1.05E-27	-2.019452961	0.153	0.031	1.66E-23	**AL591846.2**	0.00047628	1.532772291	0.188	0.164	1
ITGB2	2.10E-27	-1.323975588	0.473	0.343	3.33E-23	**KLK1**	0.302795505	0.395692985	0.203	0.188	1
SAP30L-AS1	5.74E-27	-1.574855643	0.193	0.062	9.10E-23	**C8orf44**	0.228674587	1.031357425	0.23	0.259	1
TRAV5	6.78E-27	-0.977120351	0.172	0.05	1.08E-22	**SCAANT1**	0.002197757	0.429359362	0.155	0.194	1
AL136531.1	2.64E-26	-1.757857629	0.208	0.074	4.18E-22	**TRBV6-2**	0.011292578	0.449502201	0.09	0.15	1
LPAR4	3.11E-26	-0.792568691	0.158	0.054	4.93E-22	**TFEC**	0.014200667	1.62409218	0.19	0.184	1
EED	2.05E-25	-1.948307529	0.56	0.638	3.25E-21	**AL359198.1**	0.161302917	0.791928447	0.223	0.207	1
CHMP4C	2.81E-25	-1.458560595	0.144	0.061	4.46E-21	**LINC02391**	0.008343899	1.270234731	0.141	0.18	1
PPARD	7.76E-25	-1.944636585	0.366	0.258	1.23E-20	**LINC01759**	0.442484529	0.731230623	0.132	0.141	1
AC012645.4	9.20E-25	-0.973891361	0.159	0.052	1.46E-20	**FO704657.1**	0.111711613	0.410956235	0.2	0.233	1
NCR3	1.20E-24	-0.359731978	0.43	0.285	1.91E-20	**PFN2**	0.015529077	0.658177072	0.161	0.184	1
AC240565.1	1.42E-23	-0.671301014	0.119	0.035	2.25E-19	**ADGRA3**	0.519047343	2.367106417	0.303	0.327	1
HLA-C	2.11E-23	-1.208681917	0.323	0.242	3.34E-19	**AP006333.1**	0.239731953	0.828505292	0.14	0.142	1
NECAB1	4.13E-23	-0.87731085	0.134	0.025	6.55E-19	**GP5**	0.002929454	0.501999792	0.107	0.108	1
SLC17A9	6.73E-23	-1.039204591	0.338	0.228	1.07E-18	**AL359715.3**	0.09977773	0.559467628	0.226	0.255	1
ADD3	1.20E-22	-1.307191841	0.266	0.182	1.90E-18	**TNS2**	0.161023262	0.596042188	0.237	0.263	1
SLC9A3R1	2.47E-22	0.827842916	0.341	0.251	3.91E-18	**EPHB6**	0.129276006	0.750184131	0.149	0.173	1
HLA-B	3.08E-22	-0.889346831	0.339	0.249	4.88E-18	**KRT17**	0.337380151	0.771624991	0.135	0.154	1
CLEC2D	7.45E-22	-0.757048062	0.332	0.268	1.18E-17	**AC091180.2**	0.00266657	-0.479388646	0.097	0.119	1
IGHE	1.52E-21	-1.826350835	0.262	0.214	2.41E-17	**AC019186.1**	0.000217146	-0.413967689	0.087	0.137	1
SLC22A1	1.53E-21	-1.30830224	0.176	0.048	2.42E-17	**LINC00884**	0.010467429	-1.945214809	0.258	0.246	1
EMP3	2.54E-21	-2.04131017	0.358	0.268	4.03E-17	**ARHGEF35**	0.029496735	-0.826922973	0.241	0.261	1
TAS2R43	1.46E-20	-1.326502928	0.118	0.041	2.32E-16	**LINC02175**	0.279110157	-0.368771836	0.204	0.201	1
EIF4E3	1.47E-20	-0.571234035	0.291	0.21	2.33E-16	**GALNT12**	0.002166142	-1.357853468	0.115	0.152	1
S100A4	2.79E-20	-0.781057442	0.35	0.256	4.43E-16	**AC074386.1**	0.652976712	-1.210870899	0.21	0.23	1
AL121987.2	3.81E-20	-0.616647767	0.115	0.023	6.04E-16	**LINC00891**	0.329683741	-1.123677142	0.145	0.167	1

IL32	4.43E-20	-0.921836263	0.439	0.325	7.03E-16	**LINC01337**	0.070664644	-0.841284773	0.216	0.233	1
NOXO1	6.78E-20	-0.598043154	0.156	0.041	1.08E-15	**CD79A**	0.558247773	-0.380368291	0.163	0.183	1
RORB	8.76E-20	0.95929312	0.177	0.037	1.39E-15	**AC091153.3**	0.928424072	-0.986526134	0.213	0.207	1
AL358472.3	2.29E-19	-0.693624076	0.197	0.071	3.63E-15	**AC146944.4**	0.395846539	-1.725243739	0.237	0.276	1
ANKRD61	9.79E-19	1.086994898	0.109	0.048	1.55E-14	**S100Z**	0.017875752	-2.33773172	0.125	0.129	1
SLC2A3	1.26E-18	-1.815363987	0.425	0.346	1.99E-14	**AC011893.1**	0.813866803	-0.780178451	0.249	0.232	1
ABCA7	1.72E-18	-2.288058221	0.245	0.126	2.73E-14	**ZNF546**	0.855868301	-2.050217467	0.203	0.209	1
SMPDL3A	2.74E-18	-0.970289759	0.253	0.151	4.34E-14	**AC025171.3**	0.004470864	-0.858314566	0.19	0.189	1
AL158154.2	3.81E-18	0.828871321	0.121	0.039	6.05E-14	**ACSM3**	0.951077759	-0.264816458	0.181	0.196	1
PTGDR	4.60E-18	1.3868687	0.177	0.028	7.29E-14	**ANKRD55**	0.796719027	-0.891999162	0.122	0.144	1
GIMAP1	7.97E-18	-1.038142222	0.263	0.185	1.26E-13	**AL031056.1**	0.244197241	-0.716877644	0.304	0.335	1
MMP25	1.45E-17	-0.748214016	0.468	0.378	2.29E-13	**AC022916.1**	0.757663881	-0.970623535	0.19	0.173	1
GIMAP4	1.83E-17	-0.872056511	0.258	0.18	2.90E-13	**AC006252.1**	0.134880876	-0.750998072	0.216	0.22	1
AKNA	1.33E-15	-0.871941106	0.398	0.322	2.11E-11	**HHLA2**	0.00124646	-1.101712815	0.15	0.146	1
COL27A1	3.13E-15	-0.54283194	0.221	0.15	4.97E-11	**AC005696.1**	0.381957121	-1.079238503	0.204	0.18	1
SH3D19	4.72E-13	-1.121812089	0.21	0.082	7.49E-09	**FCER2**	0.234003391	-1.065522593	0.315	0.271	1
MTRNR2L3	9.30E-13	0.652888798	0.246	0.114	1.47E-08	**C14orf28**	0.667380334	-0.99955218	0.224	0.244	1
AC022098.4	1.41E-12	-0.626726564	0.199	0.089	2.24E-08	**AC243965.1**	0.396227828	-0.751626906	0.252	0.246	1
NPHP1	4.14E-10	1.14618858	0.205	0.091	6.57E-06	**LY9**	0.428191969	-1.375491311	0.19	0.154	1
MUC12	1.18E-09	-0.87178735	0.26	0.149	1.87E-05	**FAM84B**	0.125568075	-0.331665144	0.195	0.221	1
SLC22A31	3.46E-09	-1.095023484	0.185	0.119	5.49E-05	**LRRC3**	0.003548481	-0.695008583	0.212	0.228	1
AC099811.4	5.44E-09	-1.461291966	0.256	0.152	8.62E-05	**CDH23**	0.15895901	-0.833808545	0.175	0.166	1
ZNF286B	9.22E-09	-0.883898135	0.24	0.131	0.00014621	**ABHD17C**	0.258071708	-0.820548439	0.227	0.261	1
AC009318.4	1.16E-08	-0.716672657	0.209	0.146	0.000183968	**AL592494.3**	0.563022252	-1.192476447	0.229	0.226	1
AC026979.2	1.16E-07	-1.362870314	0.21	0.118	0.00183941	**SOWAHD**	0.062728586	-1.278196455	0.142	0.135	1
HSF2BP	1.88E-07	-1.054333997	0.195	0.116	0.002985612	**RFX3-AS1**	0.001273966	-0.527334095	0.195	0.2	1
PELI3	3.00E-07	-1.046554302	0.266	0.176	0.004760207	**SH3RF2**	0.007013572	-1.07876859	0.177	0.157	1
CPEB2	3.31E-07	-0.948730088	0.297	0.228	0.005246448	**LINC01534**	0.330772161	-0.293501493	0.256	0.232	1
ZNF623	5.90E-07	-1.624546298	0.237	0.184	0.00935744	**AC009005.1**	0.007757193	-0.95283623	0.186	0.205	1
JAM3	2.13E-06	-1.994040429	0.238	0.136	0.033699252	**RBM5-AS1**	0.268586173	-1.056788278	0.249	0.245	1
KIAA1024	2.32E-06	-1.246542784	0.164	0.102	0.036740405	**EFHD1**	0.004896724	-1.037320621	0.149	0.161	1
AC011444.1	3.46E-06	-0.48545227	0.165	0.087	0.054875543	**C3orf18**	0.003898577	-0.794573679	0.164	0.169	1
ZC3H12C	9.38E-06	-1.391609346	0.354	0.293	0.148718286	**CHI3L2**	0.393096096	-0.664268579	0.125	0.096	1
TSHZ2	1.24E-05	-0.919177074	0.222	0.28	0.195995082	**AC016745.2**	0.005497702	-0.965062033	0.24	0.287	1
SLC31A2	0.000170295	0.528731853	0.275	0.158	1	**AC103739.1**	0.195910194	-0.37981418	0.154	0.197	1
AC005332.8	0.023236992	1.273472877	0.179	0.072	1	**AC006449.2**	0.222910502	-0.632594584	0.195	0.218	1
TOP1MT	0.306597871	2.10308387	0.204	0.195	1						
C5orf17	0.004438298	0.371074252	0.191	0.121	1						
PRR5L	0.00016739	-0.420303077	0.184	0.109	1						
BOLA2-SMG1P6	0.050349875	-1.515814705	0.249	0.151	1						

RNASEH2B-AS1	0.016306135	-0.763621667	0.182	0.064	1
SPNS2	0.000178999	-0.491516307	0.188	0.086	1
MARVELD2	7.53E-05	-1.470297149	0.164	0.089	1
AC015936.1	0.000944593	-2.175399745	0.158	0.096	1
GATM	7.92E-05	-1.438338693	0.175	0.108	1
FAM222A	0.000601987	-1.354769196	0.172	0.101	1
AC106795.2	7.84E-05	-1.427284739	0.199	0.09	1
AP001160.2	0.627521277	-0.75815111	0.218	0.113	1
AC073896.3	0.000147541	-0.699920485	0.2	0.126	1
PVRIG	0.081527236	-0.928793758	0.188	0.104	1
USP35	6.38E-05	-1.332108756	0.216	0.143	1
AC091153.3	0.895232598	-1.020125981	0.174	0.117	1
MAN1B1-DT	0.000281379	-0.587880991	0.224	0.17	1
AL365203.2	0.010516466	-0.785709839	0.185	0.086	1
EPM2A	0.000709022	-1.420220825	0.258	0.192	1
LIN37	0.000657787	-1.00348456	0.201	0.114	1
RPA4	0.009899623	-0.686244523	0.255	0.159	1
AL022238.2	0.087110526	-1.534352116	0.203	0.106	1
AC055811.3	8.10E-05	-1.220814261	0.228	0.087	1
SLC38A6	0.000870351	-0.945763587	0.276	0.236	1
CD79A	0.103658551	-1.140505369	0.124	0.07	1
AL365181.2	0.006521728	-1.076955749	0.208	0.121	1
TRIM16	0.111945619	-0.593831843	0.239	0.228	1
PPM1L	0.037737681	-1.081584892	0.229	0.143	1
AL109955.1	0.064258137	-2.106016555	0.221	0.12	1
AP003392.5	0.047897515	-1.009505579	0.144	0.081	1
AP003068.2	0.005394333	-1.087512372	0.193	0.114	1
NPR 2.00	0.000266826	-1.453747928	0.241	0.153	1
UBAC2-AS1	0.212537028	-1.416766681	0.242	0.132	1
ASCL2	0.167564199	-0.488387494	0.155	0.076	1
PLCD3	0.016576007	-1.489789304	0.185	0.119	1
FAM124B	0.118421843	-0.708114406	0.12	0.1	1
AC093901.1	0.068275116	-1.882520018	0.222	0.133	1
AL024498.1	0.765574735	-0.864048593	0.192	0.123	1
C19orf57	0.410067785	-1.150374606	0.157	0.096	1
RFX3-AS1	0.12118232	-2.156986073	0.203	0.107	1
AC006333.2	0.115111083	-0.56737573	0.258	0.195	1
ARL4D	0.762589392	-1.188207815	0.212	0.132	1
PHLDA2	0.863277545	-0.551256591	0.274	0.27	1
GFI1	0.323113512	-0.927022167	0.41	0.366	1

AC006213.2	0.04747803	-0.585489915	0.184	0.105	1
LINC02132	0.411465067	-1.295328259	0.184	0.083	1
RWDD3	0.778997702	-1.028433771	0.203	0.102	1
SH3RF2	0.332211794	-1.828421674	0.165	0.078	1
USP40	0.389041918	-0.660298795	0.252	0.207	1
PHOSPHO2	0.201041457	-1.668465003	0.227	0.178	1
PRRG2	0.485771137	-1.053121405	0.212	0.11	1
KISS1R	0.010027409	-0.889171308	0.214	0.152	1
AC005962.1	0.271468481	-1.071223128	0.145	0.083	1

Table A-3

Supplementary Table 3. Gene set enrichment analysis of transgene-positive cells. All Reactome pathways that were significantly enriched are listed for each donor-matched pair of samples along with enrichment scores and p-values as described in Fig. 2.1l and Fig. 2.2e.

Post Antigen Donor1 for RV-CAR vs. NV-CAR								
NAME	SIZE	ES	NES	NOM p-val	FDR q-val	FWER p-val	RANK AT MAX	LEADING EDGE
REACTOME_RNA_POL_I_TRANSCRIPTION	7	0.66567296	1.909227	0.005300353	0.40710104	0.29	791	tags=100%, list=34%, signal=150%
REACTOME_MITOTIC_G2_G2_M_PHASES	6	0.7189067	1.9086578	0.001821494	0.20409074	0.291	350	tags=67%, list=15%, signal=78%
REACTOME_TRANSCRIPTION	9	0.6128833	1.8817406	0.008849558	0.16855654	0.344	791	tags=89%, list=34%, signal=133%
REACTOME_INTERFERON_GAMMA_SIGNALING	8	0.6204505	1.872004	0.013769363	0.13474126	0.355	496	tags=75%, list=21%, signal=95%
REACTOME_INTERFERON_SIGNALING	15	0.4944482	1.8597633	0.011945393	0.11830743	0.38	737	tags=73%, list=31%, signal=106%
REACTOME_MEIOTIC_RECOMBINATION	6	0.6947637	1.8564286	0.003696858	0.10095725	0.386	722	tags=100%, list=31%, signal=144%
REACTOME_RNA_POL_I_PROMOTER_OPENING	6	0.6947637	1.848142	0	0.09186219	0.406	722	tags=100%, list=31%, signal=144%
REACTOME_RNA_POL_I_RNA_POL_III_AND_MITOCHONDRIAL_TRANSCRIPTION	7	0.66567296	1.8455071	0.003533569	0.08254243	0.415	791	tags=100%, list=34%, signal=150%
REACTOME_NEURONAL_SYSTEM	25	0.40076062	1.82583	0.015337423	0.08397113	0.452	955	tags=72%, list=41%, signal=120%
REACTOME_INTERFERON_ALPHA_BETA_SIGNALING	10	0.5570059	1.7743591	0.015490534	0.11295183	0.589	712	tags=80%, list=30%, signal=114%
REACTOME_MEIOSIS	8	0.5773609	1.7322464	0.021015761	0.13813888	0.699	722	tags=88%, list=31%, signal=126%
REACTOME_DIABETES_PATHWAYS	13	0.46174505	1.6913232	0.029508196	0.16964042	0.8	1079	tags=85%, list=46%, signal=155%
REACTOME_GABA_RECEPTOR_ACTIVATION	6	0.60899925	1.6888422	0.028673835	0.15882707	0.802	510	tags=67%, list=22%, signal=85%
REACTOME_RECRUITMENT_OF_MITOTIC_CENTROSOME_PROTEINS_AND_COMPLEXES	5	0.67922235	1.6696675	0.011299435	0.16709358	0.85	350	tags=60%, list=15%, signal=70%
REACTOME_AMYLOIDS	8	0.54036283	1.6382494	0.03583062	0.1888195	0.907	941	tags=88%, list=40%, signal=145%

REACTOME_GABA_B_RECEPTOR_ACTIVATION	6	0.60899925	1.6229666	0.041516244	0.19538221	0.928	510	tags=67%, list=22%, signal=85%
REACTOME_AXON_GUIDANCE	25	0.34822148	1.6013358	0.028616853	0.2099095	0.956	733	tags=56%, list=31%, signal=80%
REACTOME_DEVELOPMENTAL_BIOLOGY	30	0.32995278	1.5937773	0.04347826	0.20817257	0.965	733	tags=53%, list=31%, signal=76%
REACTOME_NOTCH1_INTRACELLULAR_DOMAIN_REGULATES_TRANSCRIPTION	5	0.6363495	1.590577	0.037366547	0.20027916	0.967	251	tags=60%, list=11%, signal=67%
REACTOME_NRAGE_SIGNALS_DEATH_THROUGH_JNK	5	0.62546766	1.5655395	0.044061303	0.22218354	0.985	534	tags=80%, list=23%, signal=103%
REACTOME_CELL_DEATH_SIGNALLING_VIA_NRAGE_NRIF_AND_NADE	5	0.62546766	1.5488949	0.054151624	0.2316424	0.99	534	tags=80%, list=23%, signal=103%
REACTOME_P75_NTR_RECEPTOR_MEDIATED_SIGNALLING	5	0.62546766	1.5466455	0.06315789	0.22390375	0.99	534	tags=80%, list=23%, signal=103%
REACTOME_CELL_CYCLE_MITOTIC	13	0.4208852	1.5010958	0.05794702	0.27462503	0.997	350	tags=38%, list=15%, signal=45%
REACTOME_INTEGRIN_CELL_SURFACE_INTERACTIONS	10	0.46487164	1.498429	0.065972224	0.26717225	0.998	627	tags=60%, list=27%, signal=81%
REACTOME_SIGNALING_BY_NOTCH1	6	0.56350046	1.4915476	0.0704698	0.26545832	0.999	251	tags=50%, list=11%, signal=56%
REACTOME_TRANSLATION	5	0.58114594	1.4607676	0.077634014	0.30015814	0.999	774	tags=80%, list=33%, signal=119%
REACTOME_CYTOKINE_SIGNALING_IN_IMMUNE_SYSTEM	26	0.32088098	1.460241	0.07617504	0.28975564	0.999	745	tags=54%, list=32%, signal=78%
REACTOME_CELL_SURFACE_INTERACTIONS_AT_THE_VASCULAR_WALL	10	0.44500333	1.4600917	0.07678883	0.27963415	0.999	1052	tags=80%, list=45%, signal=144%
REACTOME_NUCLEAR_RECEPTOR_TRANSCRIPTION_PATHWAY	7	0.5113293	1.4587762	0.09252669	0.27160975	0.999	387	tags=43%, list=16%, signal=51%
REACTOME_NEUROTRANSMITTER_RECEPTOR_BINDING_AND_DOWNSTREAM_TRANSMISSION_IN_THE_POSTSYNAPTIC_CELL	11	0.43308488	1.4499038	0.09615385	0.27387807	0.999	510	tags=45%, list=22%, signal=58%
REACTOME_SIGNALING_BY_NOTCH	7	0.50237167	1.4209883	0.09540636	0.30668062	0.999	516	tags=57%, list=22%, signal=73%
REACTOME_TRANSMISSION_ACROSS_CHEMICAL_SYNAPSES	14	0.38720185	1.4192259	0.116883114	0.29924783	0.999	510	tags=43%, list=22%, signal=54%
REACTOME_G_ALPHA1213_SIGNALLING_EVENTS	7	0.49204373	1.4054451	0.09892087	0.30889073	1	733	tags=71%, list=31%, signal=103%
REACTOME_CELL_CYCLE	18	0.3358573	1.365949	0.12714776	0.35604367	1	722	tags=50%, list=31%, signal=72%
REACTOME_UNFOLDED_PROTEIN_RESPONSE	7	0.46888867	1.3476703	0.13176896	0.37309656	1	1079	tags=86%, list=46%, signal=158%
REACTOME_SIGNALING_BY_RHO_GTPASES	11	0.3857876	1.3180732	0.15986395	0.41150334	1	1152	tags=82%, list=49%, signal=159%
REACTOME_POTASSIUM_CHANNELS	12	0.37777343	1.3106712	0.17520662	0.41304806	1	942	tags=75%, list=40%, signal=124%
REACTOME_SIGNALLING_BY_NGF	16	0.32538208	1.2981054	0.16194968	0.42322087	1	617	tags=44%, list=26%, signal=59%

REACTOME_CLASS_I_MHC_MEDIATED_ANTIGEN_PROCESSING_PRESENTATION	12	0.3660379	1.2919267	0.15319866	0.4220789	1	504	tags=42%, list=21%, signal=53%
REACTOME_ANTIGEN_PROCESSING_UBIQUITINATION_PROTEASOME_DEGRADATION	9	0.41441783	1.2832712	0.19757366	0.4250851	1	156	tags=33%, list=7%, signal=36%
REACTOME_GPCR_DOWNSTREAM_SIGNALING	41	0.23879935	1.2657803	0.18225807	0.442648	1	536	tags=37%, list=23%, signal=47%
REACTOME_SIGNALING_BY_GPCR	47	0.22285396	1.2394483	0.2027439	0.4774826	1	536	tags=34%, list=23%, signal=43%
REACTOME_CHROMOSOME_MAINTENANCE	5	0.4999535	1.2369653	0.21428572	0.47069207	1	722	tags=80%, list=31%, signal=115%
REACTOME_MHC_CLASS_II_ANTIGEN_PRESENTATION	9	0.39425576	1.2351407	0.23168655	0.4628178	1	686	tags=56%, list=29%, signal=78%
REACTOME_MEIOTIC_SYNAPSIS	5	0.4999535	1.2298942	0.20751342	0.4611308	1	722	tags=80%, list=31%, signal=115%
REACTOME_HEPARAN_SULFATE_HEPARIN_HS_GAG_METABOLISM	6	0.4623244	1.2233093	0.24299066	0.46238053	1	1268	tags=100%, list=54%, signal=216%
REACTOME_METABOLISM_OF_NUCLEOTIDES	6	0.44582304	1.1846067	0.2585895	0.51979077	1	656	tags=50%, list=28%, signal=69%
REACTOME_SEMAPHORIN_INTERACTIONS	10	0.35886952	1.1837653	0.24020442	0.5108136	1	733	tags=60%, list=31%, signal=87%
REACTOME_ADAPTIVE_IMMUNE_SYSTEM	36	0.22757053	1.1709337	0.26771653	0.5230764	1	710	tags=39%, list=30%, signal=55%
REACTOME_L1CAM_INTERACTIONS	11	0.3368412	1.1640729	0.2862069	0.5245092	1	370	tags=36%, list=16%, signal=43%
REACTOME_PEPTIDE_LIGAND_BINDING_RECEPTORS	14	0.31261593	1.1549506	0.271012	0.53010356	1	460	tags=36%, list=20%, signal=44%
REACTOME_PPARA_ACTIVATES_GENE_EXPRESSION	6	0.418567	1.1384487	0.29879102	0.5482117	1	249	tags=50%, list=11%, signal=56%
REACTOME_CELL_JUNCTION_ORGANIZATION	7	0.39726007	1.1262847	0.33728814	0.55949205	1	349	tags=43%, list=15%, signal=50%
REACTOME_GENERIC_TRANSCRIPTION_PATHWAY	46	0.19020161	1.0630155	0.3610675	0.6645261	1	410	tags=26%, list=17%, signal=31%
REACTOME_HEMOSTASIS	42	0.19483314	1.0572143	0.37384614	0.663631	1	1079	tags=60%, list=46%, signal=108%
REACTOME_VOLTAGE_GATED_POTASSIUM_CHANNELS	8	0.34685507	1.0308024	0.4232143	0.70253974	1	942	tags=75%, list=40%, signal=125%
REACTOME_DOWNSTREAM_SIGNAL_TRANSDUCTION	7	0.362049	1.0251833	0.43979058	0.7011635	1	496	tags=43%, list=21%, signal=54%
REACTOME_LIPID_DIGESTION_MOBILIZATION_AND_TRANSPORT	5	0.40765947	1.0127202	0.45660377	0.71248776	1	1396	tags=100%, list=59%, signal=245%
REACTOME_SIGNALING_BY_PDGF	8	0.33966976	0.9979863	0.46113074	0.72777003	1	682	tags=50%, list=29%, signal=70%
REACTOME_IMMUNE_SYSTEM	70	0.16155054	0.9949712	0.4778761	0.7211614	1	757	tags=37%, list=32%, signal=53%
REACTOME_INTEGRATION_OF_ENERGY_METABOLISM	7	0.34416643	0.9846438	0.475	0.7279876	1	624	tags=43%, list=26%, signal=58%

REACTOME_GASTRIN_CREB_SIGNALLING_PATHWAY_VIA_PKC_AND_MAPK	10	0.30057406	0.9788985	0.46793762	0.72692794	1	536	tags=40%, list=23%, signal=52%
REACTOME_G_ALPHA_Q_SIGNALLING_EVENTS	10	0.30057406	0.9781972	0.5	0.71639055	1	536	tags=40%, list=23%, signal=52%
REACTOME_FATTY_ACID_TRIACYLGLYCEROL_AND_KETONE_BODY_METABOLISM	8	0.3267967	0.9668072	0.4742268	0.72537637	1	249	tags=38%, list=11%, signal=42%
REACTOME_CHEMOKINE_RECEPTORS_BIND_CHEMOKINES	10	0.29249635	0.9616009	0.49816176	0.7230016	1	674	tags=40%, list=29%, signal=56%
REACTOME_CELL_CELL_COMMUNICATION	10	0.29698053	0.9553435	0.50886524	0.7229652	1	349	tags=30%, list=15%, signal=35%
REACTOME_MEMBRANE_TRAFFICKING	5	0.38066864	0.9515187	0.5092251	0.7184322	1	617	tags=60%, list=26%, signal=81%
REACTOME_GLYCOSAMINOGLYCAN_METABOLISM	12	0.26851055	0.9462467	0.52667814	0.717667	1	1314	tags=83%, list=56%, signal=188%
REACTOME_OPIOID_SIGNALLING	8	0.31345356	0.9196548	0.54270464	0.7529936	1	510	tags=38%, list=22%, signal=48%
REACTOME_AMINO_ACID_TRANSPORT_ACROSS_THE_PLASMA_MEMBRANE	6	0.34239438	0.9150839	0.56989247	0.750675	1	1019	tags=83%, list=43%, signal=147%
REACTOME_AMINO_ACID_AND_OLIGOPEPTIDE_SLC_TRANSPORTERS	6	0.34239438	0.9070712	0.5714286	0.7535017	1	1019	tags=83%, list=43%, signal=147%
REACTOME_FACTORS_INVOLVED_IN_MEGAKARYOCYTE_DEVELOPMENT_AND_PLATELET_PRODUCTION	10	0.26867563	0.8950034	0.568662	0.76316804	1	601	tags=40%, list=26%, signal=53%
REACTOME_G_ALPHA_I_SIGNALLING_EVENTS	16	0.2269667	0.8906187	0.57591623	0.7603843	1	510	tags=31%, list=22%, signal=40%
REACTOME_TRANSPORT_OF_INORGANIC_CATIONS_ANIONS_AND_AMINO_ACIDS_OLIGOPEPTIDES	10	0.268958	0.8764547	0.60383946	0.7735881	1	1019	tags=70%, list=43%, signal=123%
REACTOME_REGULATION_OF_INSULIN_SECRETION	5	0.33976516	0.858126	0.62566847	0.7938913	1	955	tags=60%, list=41%, signal=101%
REACTOME_METABOLISM_OF_PROTEINS	21	0.19813971	0.8509197	0.6450512	0.79599303	1	1065	tags=57%, list=45%, signal=103%
REACTOME_SIGNALING_BY_TGF_BETA_RECEPTOR_COMPLEX	9	0.27209157	0.8443655	0.6637478	0.79655296	1	383	tags=33%, list=16%, signal=40%
REACTOME_CLASS_A1_RHODOPSIN_LIKE_RECEPTORS	26	0.1749399	0.8076507	0.72195125	0.8434448	1	460	tags=27%, list=20%, signal=33%
REACTOME_METABOLISM_OF_CARBOHYDRATES	20	0.18536137	0.7756558	0.7495908	0.8817743	1	1314	tags=75%, list=56%, signal=168%
REACTOME_GPCR_LIGAND_BINDING	31	0.15891807	0.768	0.77287066	0.88260126	1	460	tags=26%, list=20%, signal=32%
REACTOME_SIGNALING_BY_ILS	12	0.21762937	0.7440001	0.7785714	0.9058615	1	496	tags=33%, list=21%, signal=42%
REACTOME_IL_3_5_AND_GM_CSF_SIGNALING	5	0.29787236	0.7382436	0.7713249	0.90297604	1	1654	tags=100%, list=70%, signal=335%
REACTOME_TRANSMEMBRANE_TRANSPORT_OF_SMALL_MOLECULES	36	0.14467984	0.7351271	0.7983871	0.8966347	1	249	tags=17%, list=11%, signal=18%
REACTOME_IL_2_SIGNALING	5	0.29787236	0.7345607	0.77459747	0.88670874	1	1654	tags=100%, list=70%, signal=335%

REACTOME_PLC_BETA_MEDIATED_EVENTS	6	0.26065275	0.6982811	0.83304346	0.92415684	1	510	tags=33%, list=22%, signal=42%
REACTOME_PLATELET_ACTIVATION_SIGNALING_AND_AGGREGATION	16	0.17859662	0.6969101	0.845787	0.91489947	1	1079	tags=56%, list=46%, signal=103%
REACTOME_SEMA4D_INDUCED_CELL_MIGRATION_AND_GROWTH_CONE_COLLAPSE	6	0.25422856	0.6776457	0.8426573	0.92763525	1	351	tags=33%, list=15%, signal=39%
REACTOME_SEMA4D_IN_SEMAPHORIN_SIGNALING	6	0.25422856	0.6748462	0.86236936	0.9203374	1	351	tags=33%, list=15%, signal=39%
REACTOME_SLC_MEDIATED_TRANSMEMBRANE_TRANSPORT	20	0.14681189	0.6225439	0.9234528	0.963917	1	21	tags=10%, list=1%, signal=10%
REACTOME_METABOLISM_OF_RNA	5	0.20996603	0.5238749	0.9699248	1	1	739	tags=40%, list=31%, signal=58%
REACTOME_METABOLISM_OF_MRNA	5	0.20996603	0.518976	0.9722222	1	1	739	tags=40%, list=31%, signal=58%
REACTOME_CHONDROITIN_SULFATE_DERMATAN_SULFATE_METABOLISM	6	0.1924223	0.5173729	0.9826087	0.9983821	1	1902	tags=100%, list=81%, signal=519%
REACTOME_NGF_SIGNALLING_VIA_TRKA_FROM_THE_PLASMA_MEMBRANE	11	0.14307624	0.4800433	0.98641765	0.9993122	1	617	tags=27%, list=26%, signal=37%
REACTOME_SIGNALING_BY_FGFR_IN_DISEASE	13	0.12381878	0.4427686	0.99668324	0.9952564	1	496	tags=23%, list=21%, signal=29%

Post Antigen Donor2 for RV-CAR vs. NV-CAR

NAME	SIZE	ES	NES	NOM p-val	FDR q-val	FWER p-val	RANK AT MAX	LEADING EDGE
REACTOME_L1CAM_INTERACTIONS	6	0.63164544	1.8344226	0.013477089	0.4408137	0.295	196	tags=67%, list=15%, signal=79%
REACTOME_SIGNALING_BY_PDGF	8	0.46369296	1.5928159	0.054755043	0.7396736	0.695	53	tags=38%, list=4%, signal=39%
REACTOME_TRANSMEMBRANE_TRANSPORT_OF_SMALL_MOLECULES	14	0.34130725	1.482007	0.086666666	0.8061991	0.862	719	tags=93%, list=57%, signal=213%
REACTOME_SIGNALING_BY_FGFR_IN_DISEASE	7	0.4491256	1.4533609	0.08947369	0.6902546	0.899	699	tags=100%, list=55%, signal=222%
REACTOME_SLC_MEDIATED_TRANSMEMBRANE_TRANSPORT	5	0.5133742	1.3889118	0.11139241	0.7246478	0.949	345	tags=80%, list=27%, signal=110%
REACTOME_DOWNSTREAM_SIGNAL_TRANSDUCTION	6	0.46927312	1.3603069	0.13725491	0.6739168	0.961	312	tags=67%, list=25%, signal=88%
REACTOME_NEUROTRANSMITTER_RECEPTOR_BINDING_AND_DOWNSTREAM_TRANSMISSION_IN_THE_POSTSYNAPTIC_CELL	6	0.44400313	1.335778	0.13941018	0.64305973	0.974	705	tags=100%, list=56%, signal=225%
REACTOME_SIGNALING_BY_FGFR	6	0.44876885	1.3190712	0.14634146	0.5982923	0.98	699	tags=100%, list=55%, signal=222%
REACTOME_SIGNALING_BY_ERBB2	6	0.44876885	1.3165251	0.16321243	0.53679234	0.982	699	tags=100%, list=55%, signal=222%
REACTOME_DEVELOPMENTAL_BIOLOGY	22	0.24323013	1.3133796	0.14285715	0.49026912	0.984	232	tags=36%, list=18%, signal=44%
REACTOME_GENERIC_TRANSCRIPTION_PATHWAY	21	0.24684457	1.2998204	0.16091955	0.46894422	0.985	59	tags=24%, list=5%, signal=25%

REACTOME_DIABETES_PATHWAYS	5	0.46746033	1.2943889	0.16172507	0.43864867	0.986	675	tags=100%, list=53%, signal=214%
REACTOME_INTEGRATION_OF_ENERGY_METABOLISM	6	0.44400313	1.2876834	0.17134832	0.4165384	0.989	705	tags=100%, list=56%, signal=225%
REACTOME_OPIOID_SIGNALLING	5	0.4436508	1.210758	0.23498695	0.51332724	0.998	705	tags=100%, list=56%, signal=225%
REACTOME_SIGNALING_BY_EGFR_IN_CANCER	5	0.44841272	1.2081909	0.22192514	0.48277983	0.999	699	tags=100%, list=55%, signal=223%
REACTOME_DOWNSTREAM_SIGNALING_OF_ACTIVATED_FGFR	5	0.44841275	1.205165	0.22693267	0.45688054	0.999	699	tags=100%, list=55%, signal=223%
REACTOME_PLATELET_HOMEOSTASIS	5	0.44365084	1.193214	0.22222222	0.45071205	0.999	705	tags=100%, list=56%, signal=225%
REACTOME_AXON_GUIDANCE	18	0.2081359	1.0664716	0.3465704	0.65054786	1	232	tags=33%, list=18%, signal=40%
REACTOME_MUSCLE_CONTRACTION	6	0.3521246	1.0372945	0.4139785	0.67627555	1	108	tags=50%, list=9%, signal=54%
REACTOME_G_ALPHA_S_SIGNALLING_EVENTS	10	0.2514102	0.9381086	0.51197606	0.85530984	1	729	tags=90%, list=58%, signal=211%
REACTOME_SEMAPHORIN_INTERACTIONS	7	0.28923425	0.9301629	0.5392954	0.8313566	1	80	tags=29%, list=6%, signal=30%
REACTOME_COSTIMULATION_BY_THE_CD28_FAMILY	5	0.32021993	0.8603327	0.63171357	0.9454426	1	5	tags=20%, list=0%, signal=20%
REACTOME_MHC_CLASS_II_ANTIGEN_PRESENTATION	6	0.2898616	0.8515078	0.6824147	0.9238174	1	342	tags=67%, list=27%, signal=91%
REACTOME_SIGNALING_BY_SCF_KIT	5	0.2879522	0.7639495	0.74805194	1	1	5	tags=20%, list=0%, signal=20%
REACTOME_CELL_CELL_COMMUNICATION	7	0.24405965	0.7542844	0.76519334	1	1	5	tags=14%, list=0%, signal=14%
REACTOME_MEMBRANE_TRAFFICKING	8	0.21780267	0.7349671	0.83125	1	1	228	tags=38%, list=18%, signal=45%
REACTOME_NGF_SIGNALLING_VIA_TRKA_FROM_THE_PLASMA_MEMBRANE	8	0.21842133	0.7305633	0.80792683	0.9939202	1	312	tags=50%, list=25%, signal=66%
REACTOME_G_ALPHA_Q_SIGNALLING_EVENTS	9	0.20132157	0.7141272	0.80712163	0.9829128	1	218	tags=33%, list=17%, signal=40%
REACTOME_METABOLISM_OF_PROTEINS	8	0.20684169	0.7063068	0.8166189	0.9607318	1	1004	tags=100%, list=79%, signal=482%
REACTOME_CELL_CYCLE_MITOTIC	7	0.22019073	0.6749028	0.8584337	0.9704625	1	987	tags=100%, list=78%, signal=453%
REACTOME_PPARA_ACTIVATES_GENE_EXPRESSION	7	0.20560159	0.6600149	0.8684211	0.95570934	1	343	tags=57%, list=27%, signal=78%
REACTOME_POST_TRANSLATIONAL_PROTEIN_MODIFICATION	7	0.20667721	0.6589155	0.89807165	0.9271483	1	1004	tags=100%, list=79%, signal=482%
REACTOME_CELL_CYCLE	18	0.134446	0.6459374	0.9215017	0.91122127	1	987	tags=94%, list=78%, signal=424%
Pre Antigen Donor2 for RV-CAR vs. NV-CAR								

NAME	SIZE	ES	NES	NOM p-val	FDR q-val	FWER p-val	RANK AT MAX	LEADING EDGE
REACTOME_PEPTIDE_LIGAND_BINDING_RECEPTORS	6	0.5089784	1.4009402	0.09785203	1	0.9	180	tags=67%, list=23%, signal=86%
REACTOME_GLYCOSAMINOGLYCAN_METABOLISM	5	0.5079999	1.3058167	0.1659292	1	0.967	139	tags=60%, list=18%, signal=73%
REACTOME_IMMUNOREGULATORY_INTERACTIONS_BETWEEN_A_LYMPHOID_AND_A_NON_LYMPHOID_CELL	11	0.2866578	1.0281936	0.39635536	1	1	550	tags=100%, list=72%, signal=347%
REACTOME_CLASS_A1_RHODOPSIN_LIKE_RECEPTORS	11	0.2844075	1.008872	0.4541387	1	1	180	tags=45%, list=23%, signal=59%
REACTOME_NUCLEAR_RECEPTOR_TRANSCRIPTION_PATHWAY	6	0.34251973	0.9669619	0.4695652	1	1	506	tags=100%, list=66%, signal=291%
REACTOME_PLATELET_ACTIVATION_SIGNALING_AND_AGGREGATION	6	0.35301843	0.9627048	0.5043668	1	1	498	tags=100%, list=65%, signal=282%
REACTOME_GPCR_LIGAND_BINDING	13	0.228183	0.8830072	0.5791962	1	1	180	tags=38%, list=23%, signal=49%
REACTOME_INTERFERON_GAMMA_SIGNALING	7	0.2851512	0.8432655	0.63461536	1	1	550	tags=100%, list=72%, signal=349%
REACTOME_METABOLISM_OF_CARBOHYDRATES	9	0.2472992	0.8232918	0.6643678	0.97162515	1	38	tags=22%, list=5%, signal=23%
REACTOME_APOPTOSIS	5	0.31330436	0.7919723	0.70509976	0.9359235	1	15	tags=20%, list=2%, signal=20%
REACTOME_G_ALPHA_I_SIGNALLING_EVENTS	7	0.26271755	0.7896227	0.71218485	0.8550848	1	180	tags=43%, list=23%, signal=55%
REACTOME_INNATE_IMMUNE_SYSTEM	6	0.19028872	0.5291453	0.9746544	1	1	622	tags=100%, list=81%, signal=522%
REACTOME_INTEGRIN_CELL_SURFACE_INTERACTIONS	9	0.15060528	0.4935626	0.98364484	0.98853964	1	518	tags=89%, list=67%, signal=270%

Table A-4

Estimates for the cost of goods for manufacturing one batch of CAR T cells for a single patient. *The costs of nonviral CAR T cell manufacturing are lower than using AAV vectors to deliver the HDR donor template.* Estimates for AAV production taken from *Cameau et al. 2019*[221].

Cost of Gene Editor for 1 Batch of Patient Apheresis Product			
Line Item	**Quantity**	**Item Cost**	**Estimated Total Cost**
Number of T Cells Collected	2x109 (Allen et al Transfusion 2017)		
DNA Template per 1x106 cells	4 µg	-	-
DNA Template per 2x109 cells	8 mg	-	-
Concentration of Purified HDR Template	2 mg/mL	-	-
Volume of Purified HDR Template	4 mL	-	-
Volume of PCR Product	80 mL (32 x 50 µL concentrated 20X to 80 µL)	-	-
Volume of Q5 Hotstart Enzyme	40 mL	$724/25 mL	$1,200
Volume of Ampure Beads	40 mL	$1488/60 mL	$2,000
Cas9 per 1x106 cells	0.8 µg		
Cas9 per 2x109 cells	16 mg	$9000/5 mg	$28,800
gRNA+crRNA per 1x106 cells	50 pmol		
gRNA+crRNA per 2x109 cells	100 nmol	$1450/100 nmol	$1450
Total cost of goods			$33,450
Cost of AAV HDR Template for 1 patient			
MOI for HDR Template	5x105 (Eyquem et al 2017)		
Total number of vector genomes (vg)	10x1014	$10000/1x1014 vg	$100,000
Total cost of goods	-	-	$100,000
Cost of Lentiviral Vector for 1 patient	-	-	$10,000

Table A-5

Antibodies used in all flow cytometry panel.

Antigen	Clone	Fluorophore	Manufacturer	Catalog #
CAR	anti-id 1A7	APC	NCI, Novus Biologics	NCI, 705-0010
CCR7	G043H7	Brilliant Violet 711	Biolegend	353228
CCR7	G043H7	Brilliant Violet 650	Biolegend	353234
CD19	HIB19	APC-Fire 750	Biolegend	302258
CD3	OKT3	AlexaFluor 488	Biolegend	304017
CD3	OKT3	Brilliant Violet 785	Biolegend	300472
CD3	OKT3	PE-Dazzle594	Biolegend	317346
CD3	OKT3	AlexaFluor 488	Biolegend	317310
CD4	OKT4	Brilliant Violet 711	Biolegend	317440
CD4	OKT4	PE-Cyanine5	Biolegend	317412
CD45RA	HI100	PE-Cyanine7	Biolegend	304125
CD62L	DREG56	Brilliant Violet 605	Biolegend	304834
CD62L	DREG56	PE	Biolegend	304840
CD69	FN50	PE-Dazzle594	Biolegend	310941
CD8	SK1	PerCP-eFluor710	ThermoFisher	46-0087-42
CD95	DX2	AlexaFluor 700	Biolegend	305648
GD2	14G2a	APC	Biolegend	357305
Human CD45	HI30	Pacific Blue	Biolegend	304022
IgG2a	RMG2a-62	APC	Biolegend	407109
LAG3	3DS223H	PE	ThermoFisher	17-2239-42
Mouse CD45.1	A20	PE-Cyanine7	Biolegend	110730
PD1	EH12.2H7	AlexaFluor 488	Biolegend	329936
TCR α/β	IP26	BV421	Biolegend	306721
TCR α/β	IP26	AlexaFluor 488	Biolegend	306712
TIM3	F38-2E2	Brilliant Violet 510	Biolegend	345030
GhostRed™780	Viability	-	Tonbo Biosciences	13-0865-T100

Table A-6

Guide RNA and primer sequences.

Oligo	**Sequence (5’ to 3’)**
TRAC crRNA	CAGGGTTCTGGATATCTGT
TRAC Donor FWD primer	CCTTTTTCCCATGCCTGCCTTT
TRAC Donor REV primer	TAAGGCCGAGACCACCAATCAG
TRAC sequencing FWD primer	ACACTCTTTCCCTACACGACGCTCTTCCGATCT
TRAC sequencing REV primer	GTGACTGGAGTTCAGACGTGTGCTCTTCCGATCT
TRAC genomic integration FWD primer	ATCTTGTGCGCATGTGAGGGGC
TRAC genomic integration REV primer	GCAAGCCAGGACTCCACCAACC

Appendix B: Supplemental Tables and Figures for Chapter 3

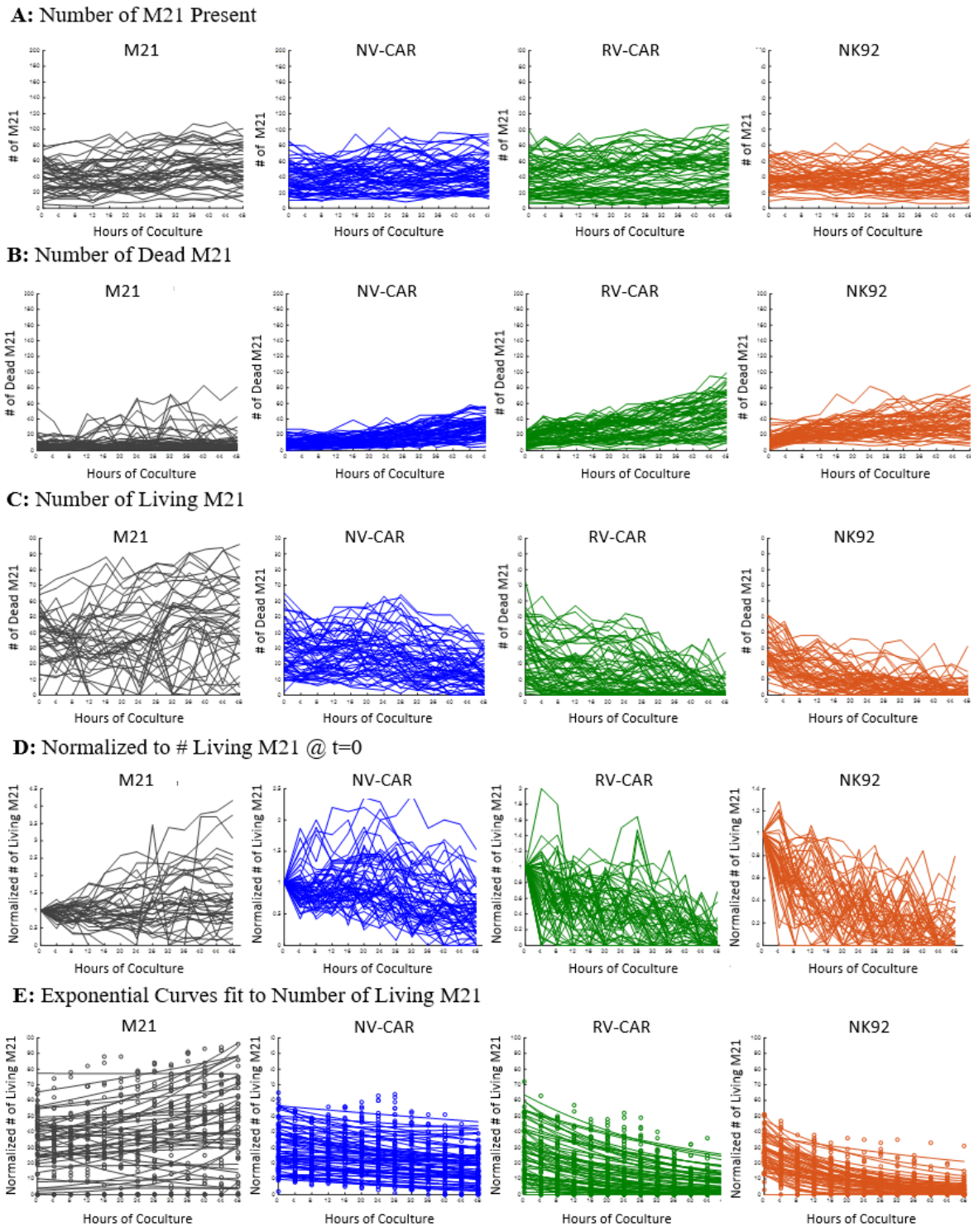
A: Number of M21 Present
M21
NV-CAR
RV-CAR
NK92
# of M21
Hours of Coculture
B: Number of Dead M21
# of Dead M21
C: Number of Living M21
D: Normalized to # Living M21 @ t=0
Normalized # of Living M21
E: Exponential Curves fit to Number of Living M21

Figure B-1

Step by step processing of Raw Microwell data to calculate β. A, Each line represents one microwell measured over time. The y-axis is the number of M21 detected in each well. Black is M21 alone, blue is M21 and NV-CAR cocultures, green is M21 and RV-CAR cocultures, orange is M21 and NK92 cocultures. **B,** The number of dead M21 detected in each microwell. **C,** The number of living M21 in each microwell, calculated by subtracting the number of dead M21 from the total number of M21. **D,** The number of living M21 in each microwell, normalized to the number of living M21 at t=0. **E,** The lines are the exponential curves that were fit to the data (dots) for the number of living M21 at each timepoint. Microwells with M21 alone are black, NV-CAR coculture with M21 are blue, RV-CAR coculture with M21 are green, and NK92 coculture with M21 are orange. n=65 microwells per condition.

A: Number of Living M21

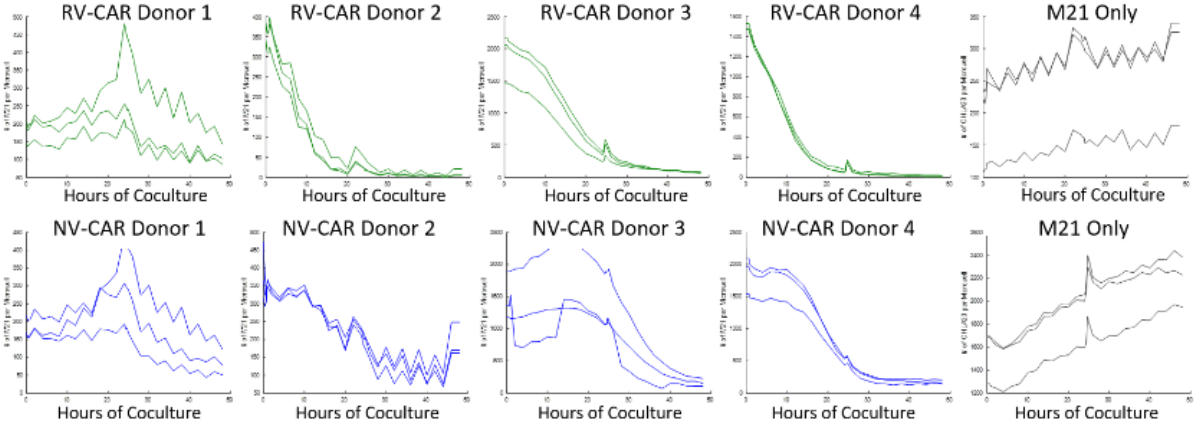

B: Normalized to # Living M21 @ t=0

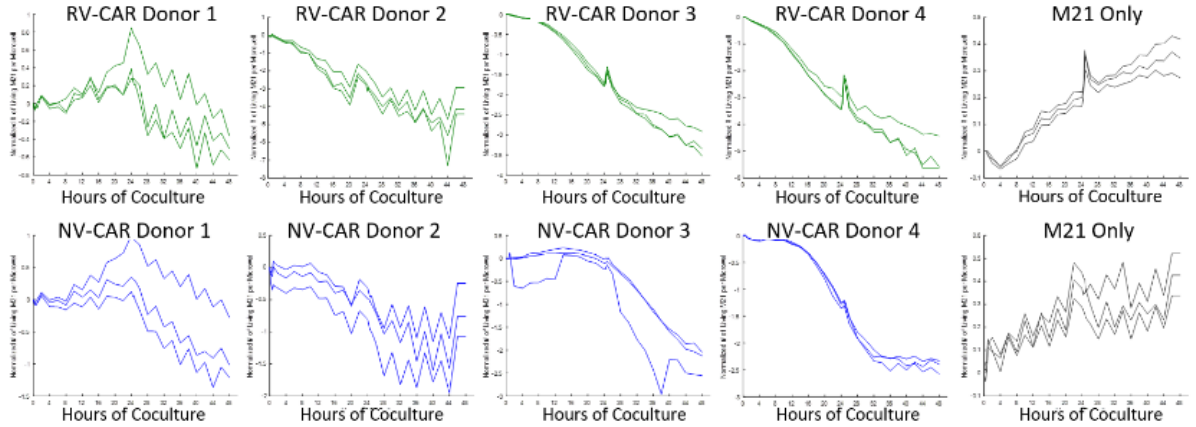

C: Exponential Curves fit to Number of Living M21

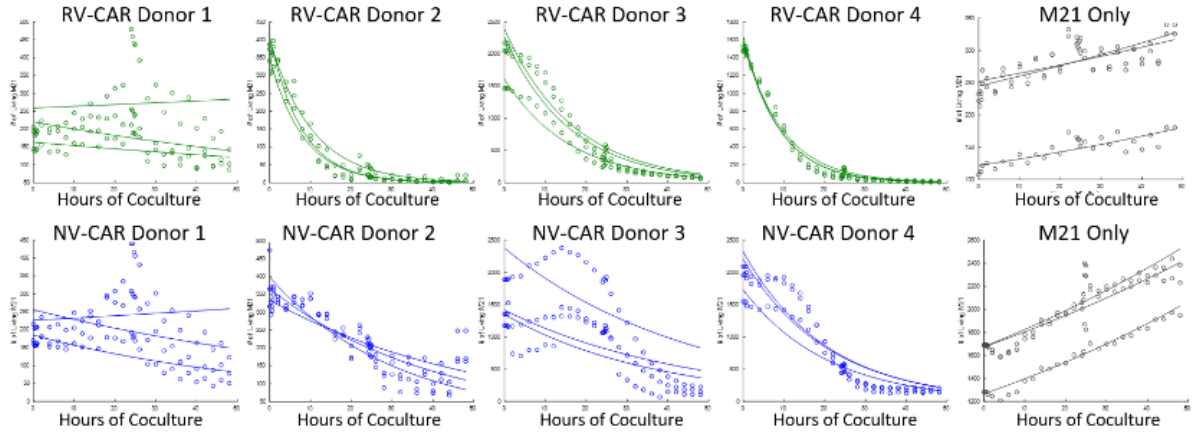

Figure B-2

Processing of Raw IncuCyte data to calculate β, for all 4 donors. A, Each line represents one well of a 96-well plate measured over time. The y-axis is the number of CHLA20 detected in each well. **B,** The number of CHLA20 in each microwell, normalized to the number of living CHLA20 at t=0. **C,** The lines are the exponential curves that were fit to the data (dots) for the number of living CHLA20 at each timepoint. Microwells with CHLA20 alone are black, NV-CAR coculture with CHLA20 are blue, and RV-CAR coculture with CHLA20 are green. n=3 wells per condition.

Code B-1

Example of Macro code used in FIJI to convert the .nd2 file into .tif files for processing in CellProfiler:

```
run("Bio-Formats Importer", "open=Z:/Nicole/Imaging_Data/2019.12.12/2019.12.12.nd2 autoscale
color_mode=Default rois_import=[ROI manager] specify_range split_timepoints split_channels
view=Hyperstack stack_order=XYCZT series_list=1-30 c_begin_1=1 c_end_1=5 c_step_1=2
t_begin_1=1 t_end_1=13 t_step_1=1 c_begin_2=1 c_end_2=5 c_step_2=2 t_begin_2=1 t_end_2=13
t_step_2=1 c_begin_3=1 c_end_3=5 c_step_3=2 t_begin_3=1 t_end_3=13 t_step_3=1 c_begin_4=1
c_end_4=5 c_step_4=2 t_begin_4=1 t_end_4=13 t_step_4=1 c_begin_5=1 c_end_5=5 c_step_5=2
t_begin_5=1 t_end_5=13 t_step_5=1 c_begin_6=1 c_end_6=5 c_step_6=2 t_begin_6=1 t_end_6=13
t_step_6=1 c_begin_7=1 c_end_7=5 c_step_7=2 t_begin_7=1 t_end_7=13 t_step_7=1 c_begin_8=1
c_end_8=5 c_step_8=2 t_begin_8=1 t_end_8=13 t_step_8=1 c_begin_9=1 c_end_9=5 c_step_9=2
t_begin_9=1 t_end_9=13 t_step_9=1 c_begin_10=1 c_end_10=5 c_step_10=2 t_begin_10=1
t_end_10=13 t_step_10=1 c_begin_11=1 c_end_11=5 c_step_11=2 t_begin_11=1 t_end_11=13
t_step_11=1 c_begin_12=1 c_end_12=5 c_step_12=2 t_begin_12=1 t_end_12=13 t_step_12=1
c_begin_13=1 c_end_13=5 c_step_13=2 t_begin_13=1 t_end_13=13 t_step_13=1 c_begin_14=1
c_end_14=5 c_step_14=2 t_begin_14=1 t_end_14=13 t_step_14=1 c_begin_15=1 c_end_15=5
c_step_15=2 t_begin_15=1 t_end_15=13 t_step_15=1 c_begin_16=1 c_end_16=5 c_step_16=2
t_begin_16=1 t_end_16=13 t_step_16=1 c_begin_17=1 c_end_17=5 c_step_17=2 t_begin_17=1
t_end_17=13 t_step_17=1 c_begin_18=1 c_end_18=5 c_step_18=2 t_begin_18=1 t_end_18=13
t_step_18=1 c_begin_19=1 c_end_19=5 c_step_19=2 t_begin_19=1 t_end_19=13 t_step_19=1
c_begin_20=1 c_end_20=5 c_step_20=2 t_begin_20=1 t_end_20=13 t_step_20=1 c_begin_21=1
c_end_21=5 c_step_21=2 t_begin_21=1 t_end_21=13 t_step_21=1 c_begin_22=1 c_end_22=5
c_step_22=2 t_begin_22=1 t_end_22=13 t_step_22=1 c_begin_23=1 c_end_23=5 c_step_23=2
t_begin_23=1 t_end_23=13 t_step_23=1 c_begin_24=1 c_end_24=5 c_step_24=2 t_begin_24=1
t_end_24=13 t_step_24=1 c_begin_25=1 c_end_25=5 c_step_25=2 t_begin_25=1 t_end_25=13
t_step_25=1 c_begin_26=1 c_end_26=5 c_step_26=2 t_begin_26=1 t_end_26=13 t_step_26=1
c_begin_27=1 c_end_27=5 c_step_27=2 t_begin_27=1 t_end_27=13 t_step_27=1 c_begin_28=1
c_end_28=5 c_step_28=2 t_begin_28=1 t_end_28=13 t_step_28=1 c_begin_29=1 c_end_29=5
c_step_29=2 t_begin_29=1 t_end_29=13 t_step_29=1 c_begin_30=1 c_end_30=5 c_step_30=2
t_begin_30=1 t_end_30=13 t_step_30=1"); //c_begin_31=1 c_end_31=5 c_step_31=2 t_begin_31=1
t_end_31=13 t_step_31=1 c_begin_32=1 c_end_32=5 c_step_32=2 t_begin_32=1 t_end_32=13
t_step_32=1 c_begin_33=1 c_end_33=5 c_step_33=2 t_begin_33=1 t_end_33=13 t_step_33=1
c_begin_34=1 c_end_34=5 c_step_34=2 t_begin_34=1 t_end_34=13 t_step_34=1 c_begin_35=1
c_end_35=5 c_step_35=2 t_begin_35=1 t_end_35=13 t_step_35=1 c_begin_36=1 c_end_36=5
c_step_36=2 t_begin_36=1 t_end_36=13 t_step_36=1 c_begin_37=1 c_end_37=5 c_step_37=2
t_begin_37=1 t_end_37=13 t_step_37=1 c_begin_38=1 c_end_38=5 c_step_38=2 t_begin_38=1
t_end_38=13 t_step_38=1 c_begin_39=1 c_end_39=5 c_step_39=2 t_begin_39=1 t_end_39=13
t_step_39=1 c_begin_40=1 c_end_40=5 c_step_40=2 t_begin_40=1 t_end_40=13 t_step_40=1
c_begin_41=1 c_end_41=5 c_step_41=2 t_begin_41=1 t_end_41=13 t_step_41=1 c_begin_42=1
c_end_42=5 c_step_42=2 t_begin_42=1 t_end_42=13 t_step_42=1 c_begin_43=1 c_end_43=5
c_step_43=2 t_begin_43=1 t_end_43=13 t_step_43=1 c_begin_44=1 c_end_44=5 c_step_44=2
t_begin_44=1 t_end_44=13 t_step_44=1 c_begin_45=1 c_end_45=5 c_step_45=2 t_begin_45=1
t_end_45=13 t_step_45=1 c_begin_46=1 c_end_46=5 c_step_46=2 t_begin_46=1 t_end_46=13
t_step_46=1 c_begin_47=1 c_end_47=5 c_step_47=2 t_begin_47=1 t_end_47=13 t_step_47=1
c_begin_48=1 c_end_48=5 c_step_48=2 t_begin_48=1 t_end_48=13 t_step_48=1 c_begin_49=1
c_end_49=5 c_step_49=2 t_begin_49=1 t_end_49=13 t_step_49=1 c_begin_50=1 c_end_50=5
c_step_50=2 t_begin_50=1 t_end_50=13 t_step_50=1 c_begin_51=1 c_end_51=5 c_step_51=2
```

```
t_begin_51=1 t_end_51=13 t_step_51=1 c_begin_52=1 c_end_52=5 c_step_52=2 t_begin_52=1
t_end_52=13 t_step_52=1 c_begin_53=1 c_end_53=5 c_step_53=2 t_begin_53=1 t_end_53=13
t_step_53=1 c_begin_54=1 c_end_54=5 c_step_54=2 t_begin_54=1 t_end_54=13 t_step_54=1
c_begin_55=1 c_end_55=5 c_step_55=2 t_begin_55=1 t_end_55=13 t_step_55=1 c_begin_56=1
c_end_56=5 c_step_56=2 t_begin_56=1 t_end_56=13 t_step_56=1 c_begin_57=1 c_end_57=5
c_step_57=2 t_begin_57=1 t_end_57=13 t_step_57=1 c_begin_58=1 c_end_58=5 c_step_58=2
t_begin_58=1 t_end_58=13 t_step_58=1 c_begin_59=1 c_end_59=5 c_step_59=2 t_begin_59=1
t_end_59=13 t_step_59=1 c_begin_60=1 c_end_60=5 c_step_60=2 t_begin_60=1 t_end_60=13
t_step_60=1 c_begin_61=1 c_end_61=5 c_step_61=2 t_begin_61=1 t_end_61=13 t_step_61=1
c_begin_62=1 c_end_62=5 c_step_62=2 t_begin_62=1 t_end_62=13 t_step_62=1 c_begin_63=1
c_end_63=5 c_step_63=2 t_begin_63=1 t_end_63=13 t_step_63=1 c_begin_64=1 c_end_64=5
c_step_64=2 t_begin_64=1 t_end_64=13 t_step_64=1 c_begin_65=1 c_end_65=5 c_step_65=2
t_begin_65=1 t_end_65=13 t_step_65=1");
for(variable=0; variable<=12; variable++){
run("Images to Stack", "name=NK92_T"+variable+"_mCherry title=[T="+variable+" C=0] use");
saveAs("Tiff",
"Z:/Nicole/Imaging_Data/2019.12.12/Concatenated/NK92/TxRed/NK92_T"+variable+"_mCherry.tif");
run("Images to Stack", "name=NK92_T"+variable+"_CellEvent title=[T="+variable+" C=1] use");
saveAs("Tiff",
"Z:/Nicole/Imaging_Data/2019.12.12/Concatenated/NK92/GFP/NK92_T"+variable+"_CellEvent.tif");
run("Images to Stack", "name=NK92_T"+variable+"_Hoechst title=[T="+variable+" C=2] use");
saveAs("Tiff",
"Z:/Nicole/Imaging_Data/2019.12.12/Concatenated/NK92/DAPI/NK92_T"+variable+"_Hoechst.tif"); }
run("Close All");
run("Bio-Formats Importer", "open=Z:/Nicole/Imaging_Data/2019.12.12/2019.12.12.nd2 autoscale
color_mode=Default rois_import=[ROI manager] specify_range split_timepoints split_channels
view=Hyperstack stack_order=XYCZT series_list=31-65 c_begin_31=1 c_end_31=5 c_step_31=2
t_begin_31=1 t_end_31=13 t_step_31=1 c_begin_32=1 c_end_32=5 c_step_32=2 t_begin_32=1
t_end_32=13 t_step_32=1 c_begin_33=1 c_end_33=5 c_step_33=2 t_begin_33=1 t_end_33=13
t_step_33=1 c_begin_34=1 c_end_34=5 c_step_34=2 t_begin_34=1 t_end_34=13 t_step_34=1
c_begin_35=1 c_end_35=5 c_step_35=2 t_begin_35=1 t_end_35=13 t_step_35=1 c_begin_36=1
c_end_36=5 c_step_36=2 t_begin_36=1 t_end_36=13 t_step_36=1 c_begin_37=1 c_end_37=5
c_step_37=2 t_begin_37=1 t_end_37=13 t_step_37=1 c_begin_38=1 c_end_38=5 c_step_38=2
t_begin_38=1 t_end_38=13 t_step_38=1 c_begin_39=1 c_end_39=5 c_step_39=2 t_begin_39=1
t_end_39=13 t_step_39=1 c_begin_40=1 c_end_40=5 c_step_40=2 t_begin_40=1 t_end_40=13
t_step_40=1 c_begin_41=1 c_end_41=5 c_step_41=2 t_begin_41=1 t_end_41=13 t_step_41=1
c_begin_42=1 c_end_42=5 c_step_42=2 t_begin_42=1 t_end_42=13 t_step_42=1 c_begin_43=1
c_end_43=5 c_step_43=2 t_begin_43=1 t_end_43=13 t_step_43=1 c_begin_44=1 c_end_44=5
c_step_44=2 t_begin_44=1 t_end_44=13 t_step_44=1 c_begin_45=1 c_end_45=5 c_step_45=2
t_begin_45=1 t_end_45=13 t_step_45=1 c_begin_46=1 c_end_46=5 c_step_46=2 t_begin_46=1
t_end_46=13 t_step_46=1 c_begin_47=1 c_end_47=5 c_step_47=2 t_begin_47=1 t_end_47=13
t_step_47=1 c_begin_48=1 c_end_48=5 c_step_48=2 t_begin_48=1 t_end_48=13 t_step_48=1
c_begin_49=1 c_end_49=5 c_step_49=2 t_begin_49=1 t_end_49=13 t_step_49=1 c_begin_50=1
c_end_50=5 c_step_50=2 t_begin_50=1 t_end_50=13 t_step_50=1 c_begin_51=1 c_end_51=5
c_step_51=2 t_begin_51=1 t_end_51=13 t_step_51=1 c_begin_52=1 c_end_52=5 c_step_52=2
t_begin_52=1 t_end_52=13 t_step_52=1 c_begin_53=1 c_end_53=5 c_step_53=2 t_begin_53=1
t_end_53=13 t_step_53=1 c_begin_54=1 c_end_54=5 c_step_54=2 t_begin_54=1 t_end_54=13
t_step_54=1 c_begin_55=1 c_end_55=5 c_step_55=2 t_begin_55=1 t_end_55=13 t_step_55=1
c_begin_56=1 c_end_56=5 c_step_56=2 t_begin_56=1 t_end_56=13 t_step_56=1 c_begin_57=1
c_end_57=5 c_step_57=2 t_begin_57=1 t_end_57=13 t_step_57=1 c_begin_58=1 c_end_58=5
c_step_58=2 t_begin_58=1 t_end_58=13 t_step_58=1 c_begin_59=1 c_end_59=5 c_step_59=2
```

```
t_begin_59=1 t_end_59=13 t_step_59=1 c_begin_60=1 c_end_60=5 c_step_60=2 t_begin_60=1
t_end_60=13 t_step_60=1 c_begin_61=1 c_end_61=5 c_step_61=2 t_begin_61=1 t_end_61=13
t_step_61=1 c_begin_62=1 c_end_62=5 c_step_62=2 t_begin_62=1 t_end_62=13 t_step_62=1
c_begin_63=1 c_end_63=5 c_step_63=2 t_begin_63=1 t_end_63=13 t_step_63=1 c_begin_64=1
c_end_64=5 c_step_64=2 t_begin_64=1 t_end_64=13 t_step_64=1 c_begin_65=1 c_end_65=5
c_step_65=2 t_begin_65=1 t_end_65=13 t_step_65=1");
for(variable=0; variable<=12; variable++){
run("Images to Stack", "name=2_NK92_T"+variable+"_mCherry title=[T="+variable+" C=0] use");
saveAs("Tiff",
"Z:/Nicole/Imaging_Data/2019.12.12/Concatenated/NK92/TxRed/2_NK92_T"+variable+"_mCherry.tif")
run("Images to Stack", "name=2_NK92_T"+variable+"_CellEvent title=[T="+variable+" C=1] use");
saveAs("Tiff",
"Z:/Nicole/Imaging_Data/2019.12.12/Concatenated/NK92/GFP/2_NK92_T"+variable+"_CellEvent.tif");
run("Images to Stack", "name=2_NK92_T"+variable+"_Hoechst title=[T="+variable+" C=2] use");
saveAs("Tiff",
"Z:/Nicole/Imaging_Data/2019.12.12/Concatenated/NK92/DAPI/2_NK92_T"+variable+"_Hoechst.tif");}
run("Close All");
```

Code B-2

Example of Macro code used in FIJI to increase the contrast of the .tif files before processing in CellProfiler:

```
// Define function
function incrContrast(input, output, filename) {
        open(input+filename);
run("Enhance Contrast...", "saturated=0.1 normalize process_all");
saveAs("Tiff", output+filename);
        run("Close"); }
//run function on folders
//NK92
input="Z:/Nicole/Imaging_Data/2019.12.12/Concatenated/NK92/TxRed/"
output="Z:/Nicole/Imaging_Data/2019.12.12/IncreasedContrast/NK92/TxRed/"
setBatchMode(true);
list=getFileList(input);
for (i=0; i<list.length; i++)
        incrContrast(input, output, list[i]);
setBatchMode(false);
input="Z:/Nicole/Imaging_Data/2019.12.12/Concatenated/NK92/GFP/"
output="Z:/Nicole/Imaging_Data/2019.12.12/IncreasedContrast/NK92/GFP/"
setBatchMode(true);
list=getFileList(input);
for (i=0; i<list.length; i++)
        incrContrast(input, output, list[i]);
setBatchMode(false);
input="Z:/Nicole/Imaging_Data/2019.12.12/Concatenated/NK92/DAPI/"
```

```
output="Z:/Nicole/Imaging_Data/2019.12.12/IncreasedContrast/NK92/DAPI/"
setBatchMode(true);
list=getFileList(input);
for (i=0; i<list.length; i++)
        incrContrast(input, output, list[i]);
setBatchMode(false);
```

Code B-3

Example of MatLab code used to calculate the β values for the microwells:

```
% how many M21 are present in each microwell
M21_NVCAR_1=readtable('MATLAB_microwell_M21.xlsx','Sheet','NVCAR1');
% how many Dead M21 are present in each microwell
dead_NVCAR_1=readtable('MATLAB_microwell_Dead.xlsx','Sheet','NVCAR1');
%% Make new ones with only data through different hours
%change timepoints to see how far to let the analysis run
timepoints=13;
% 13 is 48 hours, 10 is 36, 7 is 24, 4 is 12
endtime=4*timepoints;
x=1:4:endtime;
x=x-1;
finalspot=endtime-4;
%NVCAR
i=1;
while i<=timepoints
    M21_NVCAR_1_sub(:,i)=M21_NVCAR_1(:,i);
    i=i+1;
end
% NVCAR
i=1;
while i<=timepoints
    dead_NVCAR_1_sub(:,i)=dead_NVCAR_1(:,i);
    i=i+1;
end
% Matrices for math
M21_NVCAR_1_sub=table2array(M21_NVCAR_1_sub);
dead_NVCAR_1_sub=table2array(dead_NVCAR_1_sub);
%% fill in missing values due to outlier analysis in Prism
fixedM21_NVCAR_1_sub=fillmissing(M21_NVCAR_1_sub,'linear',2,'EndValues','near
est');
%% array back to table
fixedM21_NVCAR_1_sub_table=array2table(fixedM21_NVCAR_1_sub);
%% Line Plot # of M21 per microwell, Plot # of M21
figure;
hold on
y=fixedM21_NVCAR_1_sub_table{1,:}; % y is in raw #s
i=1;
while i<=height(fixedM21_NVCAR_1_sub_table)
    idx = ~any(isnan(y),1);
    y=fixedM21_NVCAR_1_sub_table{i,:};
    plot(x(idx),y(idx),'color',[0 0 1])
    i=i+1;
end
```

```
% Format plot
title('# M21, NVCAR1')
xlabel('Hours of CoCulture')
xlim([0 finalspot])
xticks([0 4 8 12 16 20 24 28 32 36 40 44 48])
ylim([0 200])
ylabel('# of M21 per Microwell')
hold off
%% Line Plot # of Dead M21 per microwell, calculate Average vectors
dead_NVCAR_1_sub_table=array2table(dead_NVCAR_1_sub);
% Plot # of M21
figure;
hold on
y=dead_NVCAR_1_sub_table{1,:}; % y is in raw #s
i=1;
while i<=height(dead_NVCAR_1_sub_table)
    idx = ~any(isnan(y),1);
    y=dead_NVCAR_1_sub_table{i,:};
    plot(x(idx),y(idx),'color',[0 0 1])
    i=i+1;
end
% Format plot
title('# Dead M21, NVCAR1')
xlabel('Hours of CoCulture')
xlim([0 finalspot])
xticks([0 4 8 12 16 20 24 28 32 36 40 44 48])
ylim([0 40])
ylabel('# of Dead M21 per Microwell')
hold off
%% Calculate Alive Only M21 from All M21 minus Dead M21
% Also removed all below 0 values and turned into 0
% NV-CAR
numAlive_NVCAR_1=fixedM21_NVCAR_1_sub-dead_NVCAR_1_sub;
% turn all below 0 to 0
numAlive_NVCAR_1(numAlive_NVCAR_1<0) = 0;
%plot # alive
figure;
hold on
plot(x,numAlive_NVCAR_1,'color',[0 0 1])
%plot(x,log(numAlivem_NVCAR),'color',[0 0 1])
% Format plot
title('NV-CAR 1')
xlabel('Hours of CoCulture')
xlim([0 finalspot])
xticks([0 4 8 12 16 20 24 28 32 36 40 44 48])
%ylim([0 100])
ylabel('# of Living M21 per Microwell')
hold off
%Normalize # living by dividing # living at each t by # living at t=0
% NV-CAR
normNumAlive_NVCAR_1=numAlive_NVCAR_1./numAlive_NVCAR_1(:,1);
%plot # alive
figure;
hold on
plot(x,log(normNumAlive_NVCAR_1),'color',[0 0 1])
title('Normalized, NV-CAR 1')
xlabel('Hours of CoCulture')
```

```
xticks([0 4 8 12 16 20 24 28 32 36 40 44 48])
ylabel('Normalized # of Living M21 per Microwell')
hold off
%% fit data to calc values
x=transpose(x);
% NVCAR
[la,deeda]=size(numAlive_NVCAR_1);
counter=1;
while counter <= la
    y=transpose(numAlive_NVCAR_1(counter,:));
    [eqtn,gof]=fit(x,y,'exp1');
    avecNVCAR_1(counter)=eqtn.a;
    bvecNVCAR_1(counter)=eqtn.b;
    rsqrdtNVCAR_1(counter)=gof.rsquare;
    counter=counter+1;
end
%% plot curves as lines on plot with data points

% x=transpose(x);
timepoints=13;
% 13 is 48 hours, 10 is 36, 7 is 24, 4 is 12
endtime=4*timepoints; x=1:4:endtime; x=x-1;
finalspot=endtime-4;
x=transpose(x);
% create arrays for curves
curveNVCAR_1=avecNVCAR_1.*exp(bvecNVCAR_1.*x);
curveNVCAR_1=transpose(curveNVCAR_1);
% plot
x=1:4:endtime; % x is in hours
x=x-1;
figure;
hold on
plot(x,numAlive_NVCAR_1,'o','color',[0 0 1])
plot(x,curveNVCAR_1,'color',[0 0 1])
xlim([0 finalspot])
xticks([0 4 8 12 16 20 24 28 32 36 40 44 48])
ylim([0 200])
title('Exponential Curves to fit # of Living M21, NVCAR 1')
xlabel('Hours of CoCulture')
ylabel('# of Living M21')
hold off
%% plot x axis is # NK cells at t=0, y axis is Beta*NK, killing rate for NK
cells, slope will be killing rate, Beta
%need to get # T cells at t=0
numImmune_1=readtable('DAPI_Immune_Cells.xlsx','Sheet','1');
numImmune_NVCAR_1=table2array(numImmune_1(:,2));
%get rid of empty cells in the vectors
numImmune_NVCAR_1(any(isnan(numImmune_NVCAR_1), 2), :) = [];
% colors
c2=[0 0 1];
%% multiply by % CAR+ per sample
numImmune_NVCAR_1=round(numImmune_NVCAR_1*0.1356);
%% scatter plot based on # immune cells
figure%(2)
hold on
scatter(numImmune_NVCAR_1,bvecNVCAR_1,[],c2)
title('Beta vs Immune Cells')
```

```
xlabel('# Immune Cells at t=0')
%ylim([-0.3 0.1])
ylim([-0.25 0.05])
ylabel('b')
legend('M21','NVCAR','RVCAR','location','Northeast')
hold off
% Do this for M21 and each test condition
allImmune_NVCAR_1=[numImmune_M21_1' numImmune_NVCAR_1'];
allb_NVCAR_1=[-bvecM21_1 -bvecNVCAR_1];
scatter(allImmune_NVCAR_1,allb_NVCAR_1)
cftool
```